

**DERIVING MORPHOLOGICAL CHANGES IN THE EASTERN FLANK OF
THE BRAZOS RIVER DELTA USING TERRESTRIAL LASER SCANNING
AND GPS**

A Thesis Presented to
the Faculty of the Department of Earth and Atmospheric Sciences
University of Houston

In Partial Fulfillment
of the Requirements for the Degree
Master of Science

By
Veronica Guzman

May 2017

**DERIVING MORPHOLOGICAL CHANGES IN THE EASTERN FLANK OF
THE BRAZOS RIVER DELTA USING TERRESTRIAL LASER SCANNING
AND GPS**

Veronica Guzman

APPROVED:

Dr. Guoquan Wang, Chairman

Dr. Craig Glennie

Dr. Jonny Wu

**Dean, College of Natural Sciences
and Mathematics**

Acknowledgements

Firstly, I would like to thank God. He has provided me with this opportunity and has granted me the strength and knowledge to achieve this degree.

Second, my sincere gratitude to my advisor, Dr. Guoquan Wang, for his patience, dedication, and continuous support towards his student's research. Your motivation and perseverance are greatly admirable. Also, thank you to my research committee members, Dr. Jonny Wu and Dr. Craig Glennie, for your patience and insight into my project which has guided me to improve the quality of my research work and expand my knowledge.

Thank you to Dr. Wang's research team, Xinxiang, Lin, Hanlin, Jak, Linqiang, Sarah, Kavindu, and Visilios. Without you, this project would have not been possible, and trips to Colorado and Freeport would not have been the same. I shared great memories with you.

Finally, I would like to thank my mom for her love, patience, and invaluable support. "If it is about titles, we graduated the same day, right?"

To all of my family, Daniel, and Paola.

**DERIVING MORPHOLOGICAL CHANGES IN THE EASTERN FLANK OF
THE BRAZOS RIVER DELTA USING TERRESTRIAL LASER SCANNING
AND GPS**

An Abstract of a Thesis

Presented to

the Faculty of the Department of Earth and Atmospheric Sciences

University of Houston

In Partial Fulfillment

of the Requirements for the Degree

Master of Science

By

Veronica Guzman

May 2017

Abstract

Terrestrial laser scanning (TLS) techniques have proven to be efficient to collect three-dimensional high-density and high-accuracy point clouds for coastal research and resource management. LiDAR-based bare-earth digital elevation models (DEMs) are widely used for quantification analysis of beach and dune morphological changes in time and space. This study aims to quantify the morphological changes in the vicinity of the Brazos River delta in Freeport, Texas during the period from summer of 2015 to winter of 2016 using the TLS and GPS integrated techniques.

TLS collects a massive amount of surveying points. The processing and presentation of the large volumes of datasets is always a challenge for research when targeting large areas. This study developed a practical workflow for TLS data acquisition and massive data processing, and for the analysis of digital elevation models (DEMs) aimed to derive coastal morphological changes. Four repeated TLS datasets were collected in May and December of 2015, and May and December of 2016. Four high-resolution DEMs were generated following the workflow introduced in this study. The changes of shoreline, vegetation line, dune ridge, volume, and beach profiles were investigated by utilizing the high-

resolution and highly accurate DEMs. The final analysis and visualization of results were completed using ArcGIS.

Results from this study indicate that significant beach erosion happened since the summer of 2015 to the winter of 2016. The short-term rate-of-change and net movement are higher than those calculated in previous long-term studies in the Freeport beach region. On average, the shoreline retreated 15.6 m since May 2015 to December of 2016. The change of the dune ridge is minor. However, the changes of vegetation line and dune volume are significant. The short-term rapid topographic change in the Freeport beach and dune was caused mainly by several storm flood events that affected the Texas coast in May of 2015 and April of 2016. It is expected that this study will promote the applications of the GPS and TLS techniques in coastal erosion and other natural hazards studies in Texas and other natural hazard-prone areas.

Table of Content

Chapter 1 Introduction.....	1
1.1 Introduction	1
1.2 Study Area.....	3
1.3 Motivation and Scope	6
Chapter 2 Geologic Setting	8
2.1 Coastal Geological Setting	8
2.2 Previous Studies	15
2.3 Factors Affecting Coastal Morphology	17
2.3.1 Relative Sea Level and Subsidence	17
2.3.2 Storms and Flooding	19
2.3.3 Human Causes	23
2.4 Coastal Seasonal Changes and Beach Profiles	26
Chapter 3 Introduction to LiDAR and GPS	31
3.1 LiDAR Introduction.....	31
3.1.1 Laser Ranging and Scanning.....	32
3.1.3 Terrestrial Laser Scanner	35
3.1.4 LiDAR Application on Coastal Topographic Studies	36
3.2 GPS Introduction.....	38
3.2.1 GPS and TLS Integrated Techniques	39
Chapter 4 Data Acquisition and Processing	43
4.1 LiDAR Instrumentation.....	43
4.2 GPS Instrumentation.....	46
4.3 Methods	48
4.3.1 GPS Data Acquisition and Processing.....	48
4.3.2 LiDAR Data Acquisition.....	54

4.3.3 TLS Data Processing.....	59
4.3.4 Point Cloud and DEM Accuracy Assessment	74
Chapter 5 Morphological Changes Derived from DEMs.....	82
5.1 Shoreline Analysis.....	83
5.2 Vegetation Line Analysis	99
5.3 Dune Ridge Analysis	107
5.4 Volumetric Change	111
5.4 Beach Profile Analysis	116
Chapter 6 Discussion and Conclusions	124
References.....	127

Table of Figures

Fig. 1.1: Study Area. The map shows the study area in Bryan Beach State Park in the Brazoria County, Freeport, Texas. The black line represents the beach strip where multiple scans were performed and used to derive coastal change.....	4
Fig. 1.2: Aerial photograph of the study area. Aerial picture of the study area looking at the mouth of the Brazos River and the coastal lagoon.	5
Fig. 1.3: Study area near the Brazos River delta. A picture of the study area near the Brazos River delta during the collection period of May 2015. The picture was taken following the Memorial Day Weekend flood that occurred in the Greater Houston area on May 24 and 25, 2015.	6
Fig. 2.1: Brazos River Basin in Texas. The map shows the Brazos River basin in Texas in the highlighted area. Data source: Texas Water Development Board.....	8
Fig. 2.2: New Brazos River delta, and Old Brazos delta. Scaled aerial imagery from February 2015 depicting the positioning of the New Brazos River delta versus the Old Brazos River delta. The red circle is the spot at which Fig. 2.3 was obtained.	10
Fig. 2.3: Location of the Brazos River diversion. The picture was taken at the location where the Brazos River was diverted in 1929. The right side of the picture corresponds to the new Brazos channel, and the left side corresponds to the old channel.....	10
Fig. 2.4: Environments of deposition of the Brazos River delta and its adjacent coastal area (modified from Rodriguez et al., 2000).	13
Fig. 2.5: Brazos River delta’s adjacent coastal features. Scaled aerial imagery from February 2015 that shows the features that are associated with the progradation of the headland, and other coastal features. After each flooding episode, the mouth bar is transported and preserved onshore as the new shoreline. The pre-flood shoreline is preserved as a beach ridge.	15
Fig. 2.6: Gauge stations. The flood stages of the Richmond and the Rosharon stations at the Brazos River were used in this study to determine the periods in which flood stages were surpassed as the result of severe flooding.....	21
Fig. 2.7: Gage height at the Brazos River at Richmond, Texas. Gage height at the USGS gage station in the Brazos River at Richmond, Texas. Data shows water level at the station, and the flood stage positioned at the 48 ft. mark. Data ranges from	

March 01, 2015 to January 01, 2017. (Data source: USGS National Water Information System).	22
Fig. 2.8: Gage Height at Brazos River at Rosharon, Texas. The graph shows the water level at the station, and the flood stage positioned at the 43 ft. mark. Data ranges from March 01, 2015 to January 01, 2017. (Data source: USGS National Water Information System).	23
Fig. 2.9: Closest man-made structure to the study area. Scaled aerial imagery of the nearest jetties to the Brazos River delta and Bryan Beach located at the mouth of the Freeport Harbor Channel.....	25
Fig. 2.10: Nourishment programs near the study area. The figure shows two of the three most recent nourishment programs north of the study area, near the Freeport Harbor Channel (modified from the Conrad Blucher Institute for Surveying and Science, 2017).	26
Fig. 2.11: Seasonal beach changes. The diagram shows the changes experienced by beaches from one season to another. The winter beach has a narrower beach and a steeper dune-beach profile, while the summer beach exhibits a recovered beach berm with a wider beach and a gentler beach profile.	27
Fig. 2.12: Coastal seasonal changes exhibited in our study area. The figure above shows the difference between "summer" and "winter" beaches. While the "summer" 2016 beach has a wider beach berm, the "winter" 2016 beach is narrower with a steeper profile.	28
Fig. 3.1: Diagram of LiDAR principles. The diagram shows the principle of the operation conducted by scanners that measure range through the time-of-flight method.....	33
Fig. 4.1: TLS instrument. The figure depicts the terrestrial laser scanner used in this study. A VZ-2000 by Riegl company is used with a digital camera and a GPS R10 unit mounted on top.	44
Fig. 4.2: Scanner's coordinate system diagram. The figure shows the Scanner's Own Coordinate System (SOCS), and its key components (modified from Riegl, 2014)	46
Fig. 4.3: R10 GPS unit. The GPS units used in this study are manufactured by Trimble, and its advantages include its low weight and the easiness to establish a connection with a remote controlling device.	47

Fig. 4.4: Trimble Net R9 receiver and Zephyr Geodetic II antenna. The pair was used for the kinematic GPS survey performed for accuracy assessment purposes.	48
Fig. 4.5: The reflector or reference point with a GPS unit. One of the R10 GPS units was mounted on top of a reflector which was used for registration purposes of the TLS datasets.	50
Fig. 4.6: GPS survey on the dune area. The reflector points were positioned alternately on the beach area and the dunes.	51
Fig. 4.7: GPS survey near the dune area. The R10 GPS unit was used to perform a GPS survey near and through the dunes of the study area.	52
Fig. 4.8: Kinematic GPS Survey. The figure shows the car used for the kinematic GPS survey, and the instrument mounted on top. The Zephyr Geodetic II antenna was mounted using a custom-made adapter, while the receiver was kept inside the car.	53
Fig. 4.9: Antenna used for the kinematic GPS survey. The picture shows the Zephyr Geodetic II antenna, and the adapter used to mount the antenna on top of the car.	54
Fig. 4.10: TLS data acquisition. The figure above depicts the team collecting TLS data next to the Brazos River delta. The VZ-2000 was mounted on top of a tripod, while the R10 GPS unit was mounted on top of the scanner and the camera.	56
Fig. 4.11: TLS survey in the coastal area. The figure depicts the VZ-2000 instrument being mounted on the tripod at a high ground position on the dunes.	57
Fig. 4.12: Scan positions in the coastal area. The map shows the scan positions in the beach strip from Summer 2015 to the Winter 2016 collection cycle.	58
Fig. 4.13: Point cloud from the Winter 2015 collection cycle. The point cloud was retrieved after data collection on December 09, 2015, and it shows reflectance intensity values in dB.	59
Fig. 4.14: Example of an “unregistered” point cloud. The figure shows an “unregistered” point cloud from two separate scans. The square object in the figure is a single portable restroom seen twice in the point cloud before the registration pre-processing step.	61
Fig. 4.15: Hill-shaded image of the study area. After a coordinate transformation, the study area possesses a new origin near the mouth of the delta and extends to 3000 m in the X direction, and 400 m in the Y direction.	66

Fig. 4.16: Coordinate rotation. The diagram shows the rotation of the coordinate system from ENZ to XYZ.....	67
Fig. 4.17: Methodology to derive DEMs from TLS and GPS datasets. Each step of the methodology, from data collection and DEM generation, is included in the methodology.....	71
Fig. 4.18: DEM derived from 2015 Summer TLS Survey. The figure shows the Summer 2015 digital elevation model generated after performing the processing steps established in this study.....	72
Fig. 4.19: DEM derived from 2015 Winter TLS Survey. The figure shows the Winter 2015 digital elevation model generated after performing the processing steps established in this study.....	72
Fig. 4.20: DEM derived from 2016 Summer TLS Survey. The figure shows the Summer 2016 digital elevation model generated after performing the processing steps established in this study.....	73
Fig. 4.21: DEM derived from 2016 Winter TLS Survey. The figure shows the Winter 2016 digital elevation model	73
Fig. 4.22: GPS survey points. Scaled image of the GPS points labeled A through B collected in the study area on December 5 th , and the selected GPS points for the December 6 th survey. These surveys were used to perform the point cloud and DEM accuracy assessment of the study.....	76
Fig. 4.23: DEM accuracy assessment results for the cross-dune area. The plots show the elevation value comparisons of the four profiles extracted from the RTK survey and the Winter 2016 DEM.	78
Fig. 4.24: Point cloud accuracy assessment results for the cross-dune area. Profiles A through D depict the accuracy assessment of the raw data points.....	79
Fig. 4.25: Point cloud and DEM accuracy assessment results for the flat-beach area. The plots show the comparison of elevation values between the GPS survey and both the raw LiDAR datasets and the final DEM from December of 2016....	80
Fig. 5.1: Coastal features extracted from the study area. A diagram that shows a cross-beach profile example of the features extracted in this study including the shoreline, vegetation line, and dune ridge.....	82
Fig. 5.2: Extracted shorelines of the study area. After extracting the contours for each dataset, the shorelines were approximated and extracted.....	86

Fig. 5.3: Shorelines, baseline, transects, and intersects. The figure shows the extracted shorelines, the constructed baseline, the transects built perpendicular to the baseline, and the intersects of the transects with the shorelines. 86

Fig. 5.4: Shoreline, transects, and intersects. The zoomed-in figure shows the approximated shorelines for all the four collection cycles, the transects, and the intersect points. 87

Fig. 5.5: Shoreline change envelope. The diagram shows the distance measured from the closest to the farthest shoreline to the baseline representing the shoreline change envelope (modified from Himmelstoss, 2009). 88

Fig. 5.6: Net shoreline movement. The net shoreline movement represents a distance between the oldest and the youngest shorelines (modified from Himmelstoss, 2009). 89

Fig. 5.7: Shoreline’s end point rate. The end point rate represents the net shoreline movement (distance between the youngest and oldest shoreline) divided by the time elapsed between those two shorelines (modified from Himmelstoss, 2009). 89

Fig. 5.8: Shoreline change envelope. Change envelope representing the distance between the closest and the farthest shorelines to the baseline. 91

Fig. 5.9: Net shoreline movement. The figure shows the net shoreline movement, or the distance from the oldest to the youngest shoreline in the study area. 92

Fig. 5.10: Shoreline end point rate. The figure shows the yearly rate of shoreline change at each transect in the study area. 93

Fig. 5.11: Net shoreline movement from summer 2015 to summer 2016. The figure shows the net movement between the summer 2015 shoreline and the summer 2016 shoreline. 95

Fig. 5.12: Net shoreline movement from winter 2015 to winter 2016. The figure shows the net shoreline movement between the winter 2015 and the winter 2016 shorelines. 96

Fig. 5.13: Net shoreline movement from summer 2015 to winter 2015. The figure shows the distance between the summer 2015 and the winter 2015 shorelines. .. 97

Fig. 5.14: Net shoreline movement from the summer of 2016 to the winter of 2016. The figure shows the distance between the summer of 2016 and the winter of 2016 shorelines. 98

Fig. 5.15: Approximated vegetation lines of all collection cycles. The figure shows the vegetation lines from Summer 2015, and 2016, and Winter 2015 and 2016 of the study area. 102

Fig. 5.16: Vegetation line, baseline, transects, and intercepts. The figure shows the approximated vegetation lines, the baseline constructed in ArcGIS, and the transects, and intersects derived from DSAS. 102

Fig. 5.17: Approximated vegetation lines, transects, and intersects. The zoomed-in figure shows the approximated vegetation lines for all the four collection cycles, the transects, and the intersect points between the transects and the vegetation lines. The approximated vegetation lines were split into four plots of approximately 600 m long. 103

Fig. 5.18: Approximated vegetation line change envelope. The distance at each transect between the closest and the farthest vegetation line to the baseline is depicted in the figure. 105

Fig. 5.19: Net vegetation line movement. The figure shows the distance between the youngest and the oldest vegetation lines at each transect in the study area. 106

Fig. 5.20: Approximated vegetation line's end point rate. The figure shows the yearly rate of vegetation line movement at each transect in the study area. 107

Fig. 5.21: Dune ridges, shorelines, and vegetation lines. The figure shows the dune ridges and their position relative to the shorelines and vegetation lines for (a) Summer 2015, (b) Winter 2015, (c) Summer 2016, and (d) Winter 2016. 110

Fig. 5.22: Summer 2015 to Winter 2015 volumetric change. The figure shows the volumetric change after the *Cut Fill* tool was applied in ArcGIS. 114

Fig. 5.23 Winter 2015 to Summer 2016 volumetric change. The figure shows the volumetric change after the *Cut Fill* tool was applied in ArcGIS. The..... 114

Fig. 5.24: Summer 2016 to Winter 2016 volumetric change. The figure shows the volumetric change after the *Cut Fill* tool was applied in ArcGIS. 115

Fig. 5.25: Summer 2015 to Winter 2016 volumetric change. The figure shows the volumetric change after the *Cut Fill* tool was applied in ArcGIS. 115

Fig. 5.26: Beach profile for Summer 2015 at X = 2000 m. The beach profile extracted at the X = 2000 m mark from the 150 m to 200 m cross-dune positions. 117

Fig. 5.27: Beach profile for Summer 2015 at X = 2600 m. The beach profile extracted at the X = 2600 m mark from the 150 m to 200 m cross-dune positions. 118

Fig. 5.28: Beach profile for Summer 2016 at X = 2000 m. The beach profile extracted at X = 2000 m mark from the 150 m to 200 m cross-dune positions. 119

Fig. 5.29: Beach profile for Summer 2016 at X = 2600 m. The beach profile extracted at the X = 2000 m mark from the 150 m to 200 m cross-dune positions. 120

Fig. 5.30: Beach profiles for all datasets. The figure shows the beach profiles at the X = 2000 m and X = 2600 m coordinate marks. 123

List of Tables

Table 1. Maximum range measurements in meters for the Riegl VZ-2000 scanner instrument. These are values for average conditions, flat targets, and perpendicular angle of incidence.....	34
Table 2: VZ – 2000 by Riegl Specifications.....	43
Table 3: TLS surveys’ information.....	55
Table 4. Accuracy assessment statistical results for the cross-dune GPS survey. The table shows the standard deviation and the mean of the elevation differences of the point cloud versus the DEM.....	77
Table 5. Accuracy assessment statistical results for the flat-beach GPS survey. The table shows the standard deviation and the mean of the elevation differences of the point cloud versus the DEM.....	81
Table 6. Summary of the net shoreline movement results. The table shows the net shoreline movement values for each time period analyzed. Negative values correspond to shoreline retreat.....	99

Chapter 1 Introduction

1.1 Introduction

As one of the fastest-growing and most dynamic coastal areas in the United States, the accurate monitoring and analysis of the Texas coast is important for the quantification and identification of areas of erosion or accretion, the assessment of net sediment transport, and the zoning of hazard areas. The understanding of morphological processes in coastal areas is influenced by our comprehension of components affecting trends in coastal change. Factors such as sea level conditions, storm frequency and intensity, subsidence, sediment influx, and human activities are parameters that affect coastal morphology. The increased impact of climate change and the strengthening of geohazards as consequence of rising sea level and warming global temperatures have made coastal research a relevant subject in geomorphic studies.

The quantification of morphological changes in coastal areas is aided by the analysis of periodic changes of beach features such as shoreline, vegetation line, and the dune ridge. Historically, coastal rates-of-change and net beach movement have been established by the interpretation of aerial photography, topographic maps, and beach profiles (Paine et al., 2014). However, with the advancement of

laser light technology, most recent coastal studies include the application of LiDAR surveying method.

LiDAR, or Light Detection and Ranging, is a remote sensing technique that uses laser pulses to measure distances to the target surface. Range measurements lead to the generation of point clouds, or a set of points with defined coordinates that support the creation of digital elevation models used for further analysis. LiDAR data can be collected from terrestrial or aerial platforms, the latter being the most common practice. However, the necessity for more affordable surveys and accurate datasets have made terrestrial LiDAR a more appealing technique to be used in geological studies.

Terrestrial laser scanning (TLS) is a growing method in coastal morphological studies. Multiple studies have been published using the scanning technique (e.g., Buckley et al., 2008; Santos et al., 2014). However, the main challenge in this field remains the lack of standardized techniques to process massive and dense TLS datasets for the purpose of producing digital elevation models of the study areas, and to analyze and extract rates-of-change and net coastline movement (Buckley et al., 2008). This study intends to derive a methodology to collect and process dense TLS datasets and to generate DEMs. The DEMs were used to determine coastal morphological changes in Bryan Beach, Freeport, Texas. This beach was

selected for this study due to the dynamic environment it represents. Multiple studies have concluded this beach strip as one of the most active coastal areas in Texas (Gibeaut et al., 2000; Morton and Pieper, 1975). The diverted mouth of the Brazos River is directly adjacent to the beach area, and the Freeport Harbor Channel entrance is located northeast of the area.

1.2 Study Area

The area surveyed and analyzed is Bryan Beach in Brazoria County, which corresponds to the northeastern flank of the Brazos River delta (Figs. 1.1 through 1.3). The beach is located to the south of Houston, and southwest of the Freeport Harbor Channel and the previous location of the Brazos River delta. It is located in Freeport, Texas which possesses a population of 12,049 residents. The area encompasses a total of 2000 meters of beach shore from the east mouth of the delta to the updrift direction.

In the 2000s, the coast of Texas experienced a total of 10 hurricanes and tropical storms, while the average annual rainfall ranges from 103.7 cm to 124.87 cm (Rodriguez et al., 2000). The littoral drift is southwest with a gross transport rate by waves of 249,000 m³/year (Gibeaut et al., 2000).

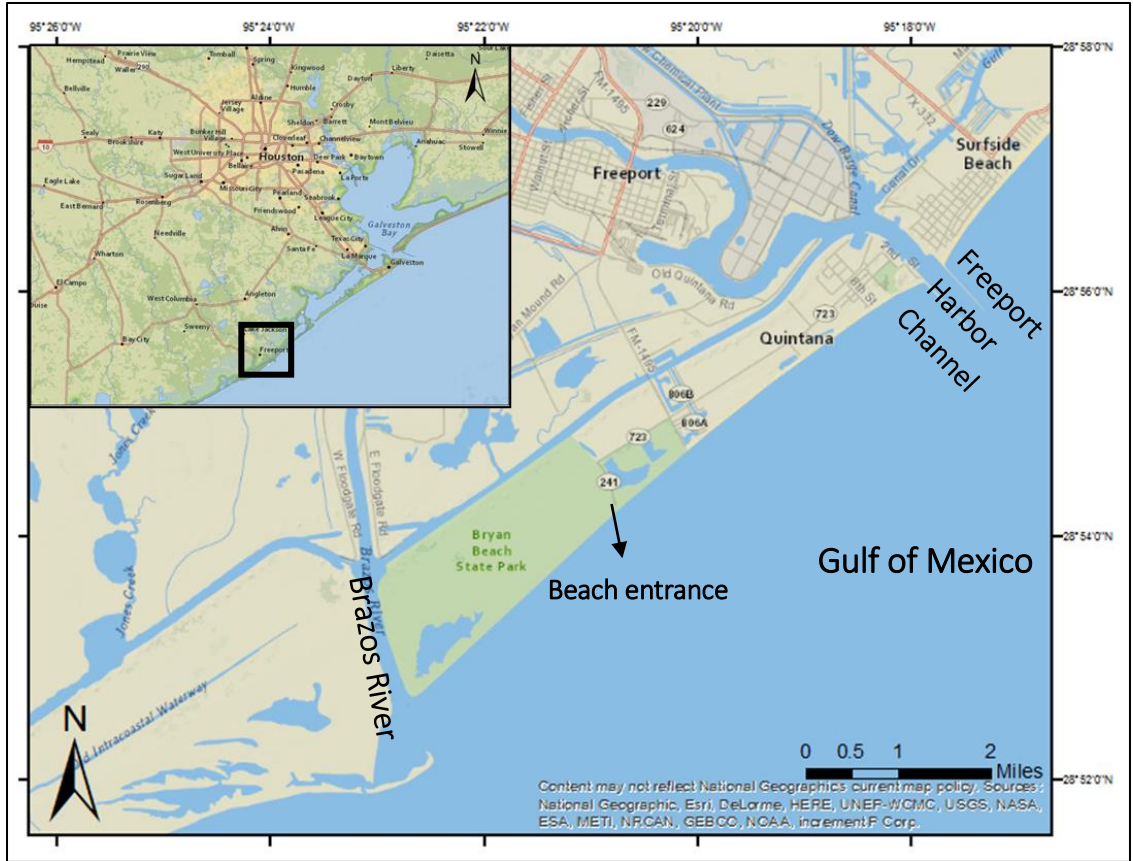


Fig. 1.1: Study Area. The map shows the study area in Bryan Beach State Park in the Brazoria County, Freeport, Texas. The black line represents the beach strip where multiple scans were performed and used to derive coastal change.



Fig. 1.2: Aerial photograph of the study area. Aerial picture of the study area looking at the mouth of the Brazos River and the coastal lagoon.



Fig. 1.3: Study area near the Brazos River delta. A picture of the study area near the Brazos River delta during the collection period of May 2015. The picture was taken following the Memorial Day Weekend flood that occurred in the Greater Houston area on May 24 and 25, 2015.

1.3 Motivation and Scope

Several studies have reported the broad morphological history of the Texas coast based on airborne LiDAR and aerial photography; however, there is no specific study aimed towards our study area, and there is not a defined methodology for the collection, processing, and analysis of TLS datasets aimed to coastal studies. The objectives of this study are to derive a methodology to collect and process substantial TLS datasets, and to derive morphological changes based

on digital elevation models of the beach area adjacent to the Brazos River delta, specifically, the northeast flank of the delta located at Bryan Beach. To achieve these goals, terrestrial LiDAR and GPS datasets were acquired in May of 2015 and 2016, and December of 2015 and 2016. DEMs of the corresponding periods of data were generated to extract coastal features that were analyzed to calculate net movement and morphological changes in the coastal area. Coastal features extracted and analyzed in this study include the shoreline, the vegetation line, and the dune ridge. Furthermore, it was in the interest of this study to analyze and derive seasonal morphological changes. The volumetric changes and beach profiles of the area were analyzed and considered to be proxies for changes relative to seasonal patterns.

Terrestrial laser scanning (TLS) data acquired for over two days in each collection cycle was processed using several software tools that include RiSCAN Pro (V2.2.1), Generic Mapping Tools (GMT), and shell scripts. Moreover, several analyst tools in ArcGIS were applied to extract the coastal features that were used to derive morphological and volumetric changes in the area.

Chapter 2 Geologic Setting

2.1 Coastal Geological Setting

The Brazos River delta, located southeast of Freeport, Texas, corresponds to the depositional landform of one of the longest rivers in Texas. The Brazos River (Fig. 2.1) originates at Llano Estacado, or Staked Plains, located northwest of Texas and east of central New Mexico, and it runs the length of 840 miles through Texas.

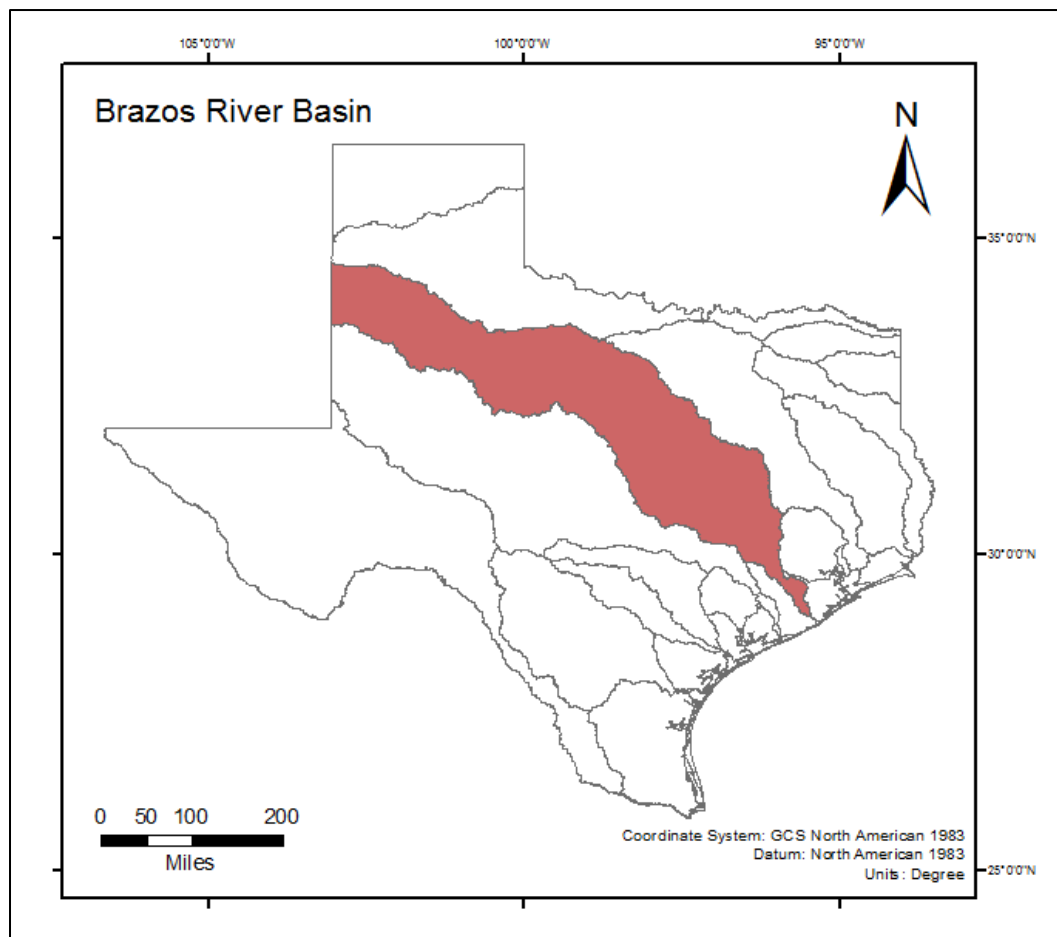


Fig. 2.1: Brazos River Basin in Texas. The map shows the Brazos River basin in Texas in the highlighted area. Data source: Texas Water Development Board.

The Brazos River basin encompasses an area of approximately 116,000 km², and it is the second largest basin in Texas. It also possesses the highest suspended-sediment yield in the state with 39 metric tons/km² (Curtis et al., 1973). However, the river's sediment supply capacity has been reduced due to the construction of dams and reservoirs; there are 19 major reservoirs throughout the Brazos River. Sediment supply consists mostly of clay and sand particles derived from Triassic red beds from Northern Texas and Eastern New Mexico (Sidwell, 1940).

The Brazos River delta was diverted to its present location in 1929 by the U.S. Corps of Engineers due to flooding concerns (Figs. 2.2 and 2.3). The proposed new delta was planned to diminish the high maintenance costs affecting the Freeport Harbor due to floods (Morton and Pieper, 1975). The diversion caused most of the headland sands of the old delta to be transported to the east land adjacent to the new delta. Sediment deprivation in the old delta caused erosion from the west jetty to up to 3 miles west, while the new delta experienced rates of accretion of up to 256.6 ft/year in the years following diversion (Morton and Pieper, 1975).

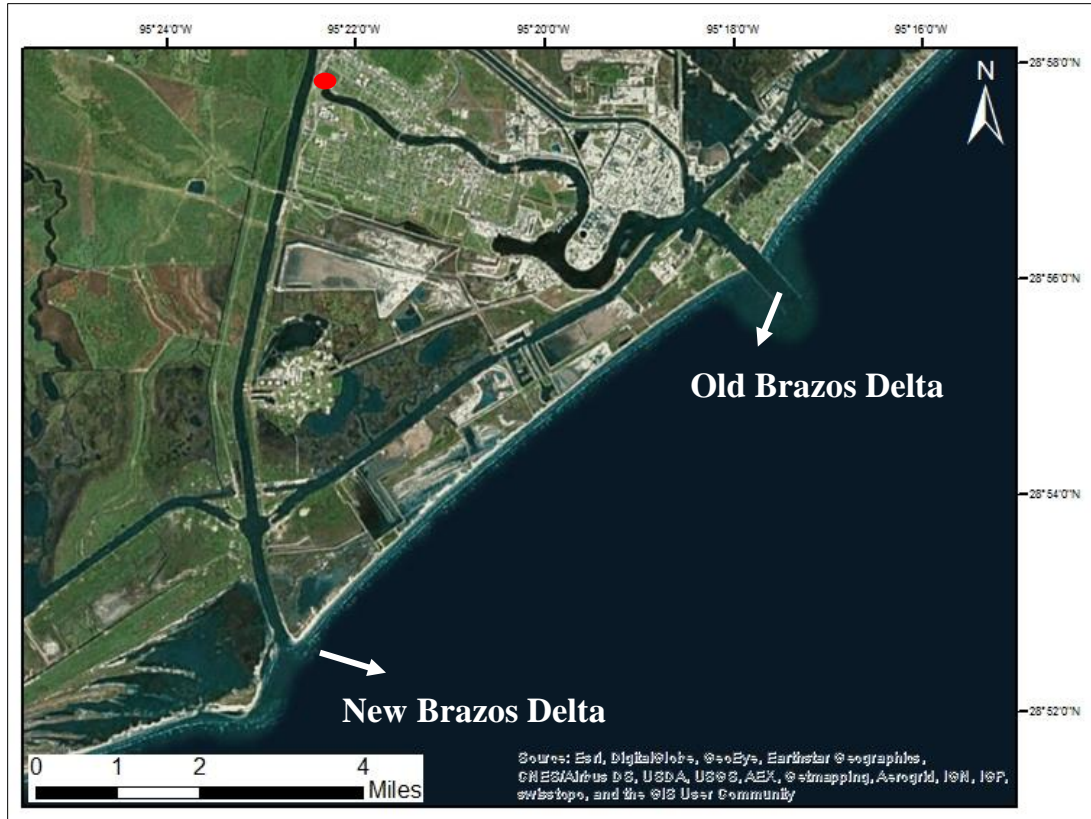


Fig. 2.2: New Brazos River delta, and Old Brazos delta. Scaled aerial imagery from February 2015 depicting the positioning of the New Brazos River delta versus the Old Brazos River delta. The red circle is the spot at which Fig. 2.3 was obtained.



Fig. 2.3: Location of the Brazos River diversion. The picture was taken at the location where the Brazos River was diverted in 1929. The right side of the picture corresponds to the new Brazos channel, and the left side corresponds to the old channel.

Based on Galloway (1975) classification, the delta is wave-dominated, and the resulting energy of waves define its shape and the reworking of the sediments. The delta is considered to be lobate in shape, and accretion is descriptive of the west flank where the headland is located.

Furthermore, as it is characteristic of wave-dominated deltas, the Brazos River delta exhibits short-parallel amalgamated and non-amalgamated beach ridges on the downdrift side of the delta. The east bank is composed of beach ridges, and a lagoon directly adjacent to the new delta (Fig. 2.5). Wave refraction is the main agent responsible for the orientation of beach ridges along the area (Rodriguez et al., 2000).

The fluvial sediment supply plays an important role in the morphological changes experienced by the adjacent beach area. Sediment supply by fluvial sources accounts for 95% of oceans' sediment influx (Syvitski, 2003). River discharge at the Richmond streamflow-gaging station was 7,600 ft³/s during the 1941-1995 period (Dunn and Raines, 2001), while the annual sediment yield of the Brazos River is 39 metric tons/km². In 2015, the average discharge was 12,560 ft³/s, while in 2016 it was 25,200 ft³/s at the same station. Sediment is reworked by east-to-west longshore drift which implies sediment deposition and accretion on the west flank and headland of the delta. For example, after the diversion of the delta,

currents reworked sediments from the old delta towards the east flank and the headland of the new delta which accreted at a high rate. Since then, a slower rate of accretion became the characteristic trend of the headland, while overall erosion is the representative pattern of the Texas coast.

The environments of deposition of the delta and its surrounding coastal areas were divided into three categories by Rodriguez et al., 2000: (1) the onshore environment, (2) the delta front, and (3) the offshore environment (Fig. 2.4). The onshore environment encompasses the active and mineralogically mature beach ridges separated by tidally-influenced interridge troughs made of thin-bedded sands, and the highly diverse mainland beach with poorly sorted and mean grain-sized sands. The delta front, which is the area directly adjacent and seaward to the river mouth, includes the channel mouth bars with the coarsest sands of the coastal area, and the back-bar lagoon which is also tidally-influenced with fine-grained muddy sediments. Lastly, the offshore environment includes the shoreface, the distal delta front, and the prodelta. The shoreface sands are mature and well-sorted, and they extend to both sides of the delta. The distal delta front is made of clay and some coarse sands, while organic material is also present in its sediments. The prodelta represents the environment which demonstrates the type of episodic

sedimentation exhibited by the delta. With fluvial discharge, reddish-brown clay sediments are deposited, followed by the deposition of offshore marine sediments.

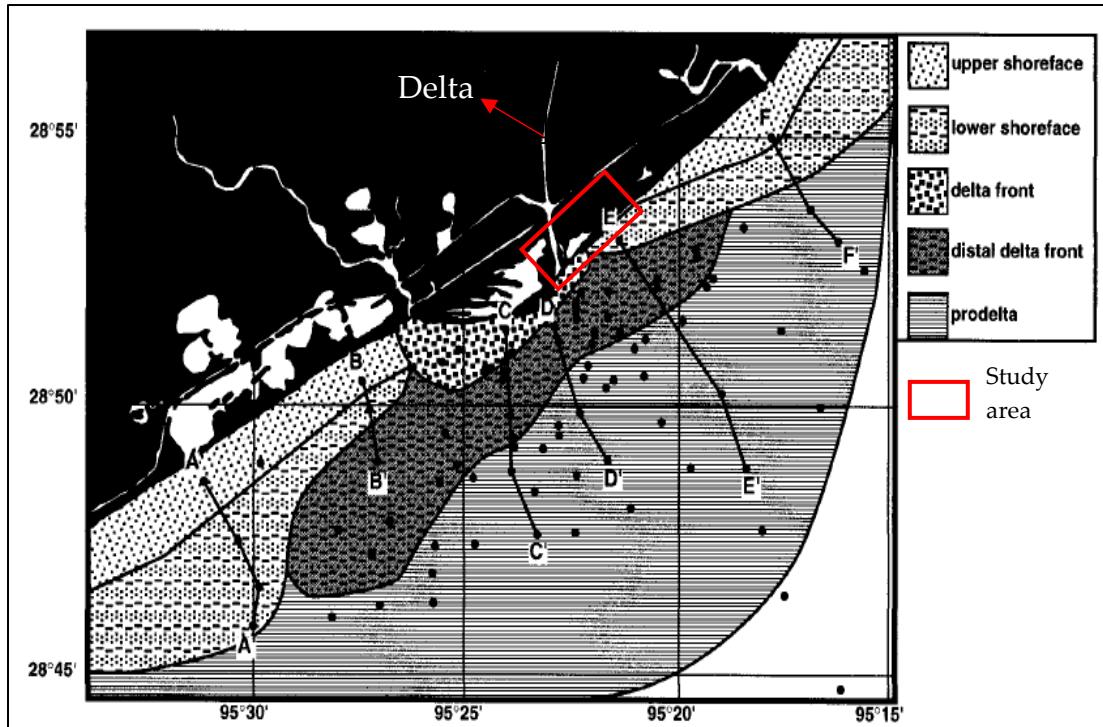


Fig. 2.4: Environments of deposition of the Brazos River delta and its adjacent coastal area (modified from Rodriguez et al., 2000).

Flooding is historically related to the expansion and migration of the delta's mouth bar. Major floods resulting in the overflow of the delta that occurred in 1941, 1957, 1965, and 1992 caused the migration of the bar, and this can be appreciated in the numerous beach ridges that formed from previous shorelines (Fig. 2.5). Rodriguez et al., 2000, studied in depth the impact of flooding episodes on the delta's morphology. Accretion of the headland is associated with major floods. Following each flooding episode, wave energy and direction control the

reworking of the sediments in a landward and westward direction. After flooding, the channel mouth bar is reworked and welded to the old shoreline, becoming the new shoreline. The old shoreline becomes a beach ridge, and the back-bar lagoon becomes the trough. Historical images show pre-flood shorelines preserved in the area as beach ridges while the offshore bar becomes the new shoreline after flooding episodes (Fig. 2.5). In between floods, the shoreline and ridge amalgamation, or the reworking of sand due to wave energy, is characteristic on both sides of the delta.

Although the onshore environment is highly affected by floods, major storms affect mostly the delta front (Rodriguez et al., 2000). While flooding creates a new mouth bar in the delta front that can ultimately become the new shoreline, major storms can sweep them away even before the shoreline is completely formed. Nevertheless, coastal areas can experience significant sand loss and beach-profile changes due to major storms.

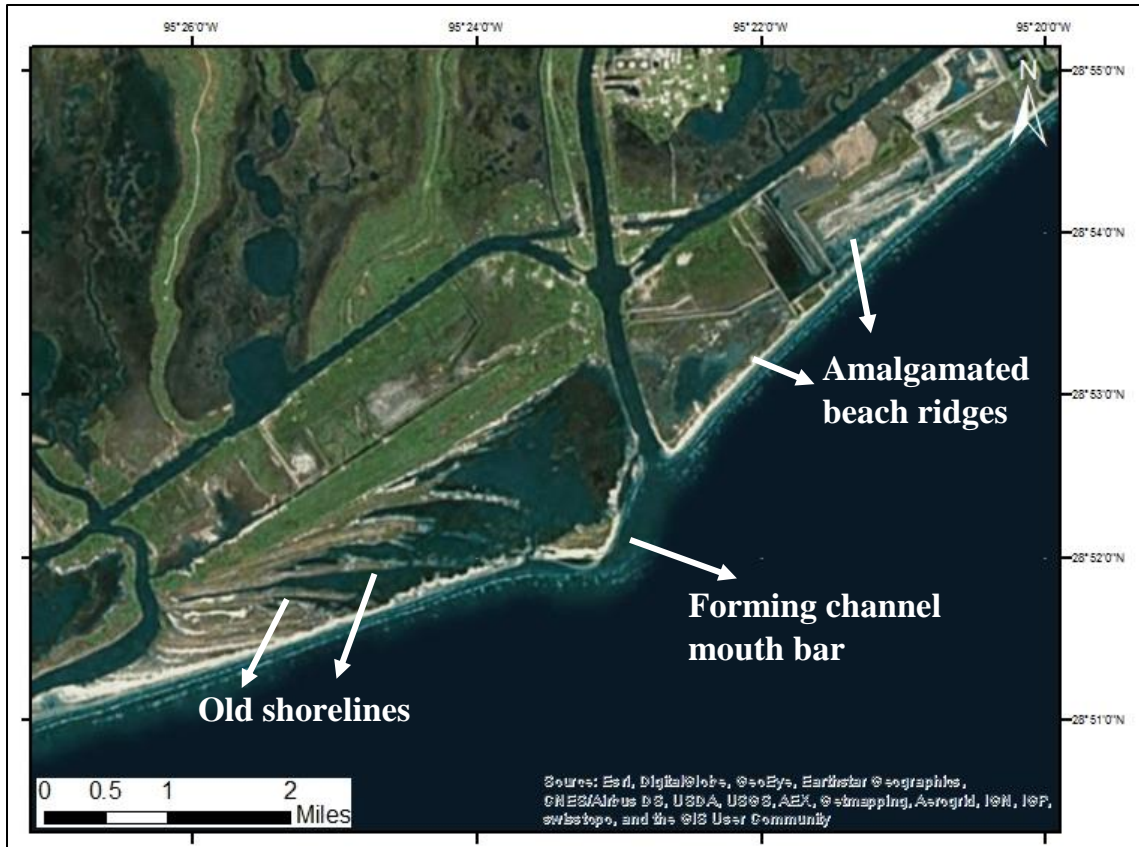


Fig. 2.5: Brazos River delta's adjacent coastal features. Scaled aerial imagery from February 2015 that shows the features that are associated with the progradation of the headland, and other coastal features. After each flooding episode, the mouth bar is transported and preserved onshore as the new shoreline. The pre-flood shoreline is preserved as a beach ridge.

2.2 Previous Studies

The Bureau of Economic Geology (BEG) has provided multiple publications revealing long-term rates-of-change of the Texas coastline. The investigations were largely drawn by studying aerial photography (collected from the 1930s), and topographic charts (collected from the 1850s). A study published in 1975 by Robert A. Morton and Mary J. Pieper offered a deep insight into Texas coastal

changes. The study analyzed historical data from 1852 to 1856 and from 1930 to 1974 of the Texas coast from the San Luis Pass near Galveston to Brown Cedar Cut near Matagorda. In general, the study concluded an overall erosional trend; however, the area adjacent to the new Brazos River delta was the exception during the study's period. Net accretion was characteristic of the area near the new Brazos delta, with short-term periods of erosion. Near the old Brazos River delta, net accretion was recorded until 1929 where diversion of the delta caused erosion on the west flank.

From the 2000s, studies about coastline changes in Texas have been conducted using integrated airborne LiDAR and GPS technologies. The BEG's most recent study was published in 2014, and it encompassed data from the 1930s to 2012. In our study area located at Bryan Beach (between the Brazos River delta and Surfside Beach), the long-term rate-of-change was calculated to be approximately up to 4.5 m of shoreline retreat per year (Paine et al., 2014). Overall, evidence indicates that there is an erosional trend along the coast of Texas. However, the Texas coast accreted from 2010 to 2011 as a response period from Hurricane Ike. Since then, coastal morphological behavior has returned to long-term erosional trend. Nonetheless, short-term rates of erosion and net coastal movement in the study area are expected to be higher than the calculated long-term rate-of-change

due to the recent climatic events that affected southeast Texas. During May of 2015 and April of 2016 multiple historical storms and floods affected Texas. A more rapid pattern of erosion is expected following major storms because they can cause disequilibrium in the sediment budget of coastal areas, which can lead to abnormal coastal changes. Furthermore, the flood episodes during the spring and summer months are expected to produce alterations of the projected coastal seasonal changes in the beach profiles since storms are usually expected to be more frequent during the winter months rather than the summer months.

2.3 Factors Affecting Coastal Morphology

2.3.1 Relative Sea Level and Subsidence

Sea level is defined as the average height of the ocean. Globally, eustatic sea-level changes are due to size alterations of ice caps and snow caps, and the expansion or contraction of sea water as the temperature changes, while local isostatic changes are due to changes in the land height. Relative sea-level rise affects coastal morphology because of the risk of water inundation of low coastal areas and landward displacement of shorelines and the vegetation lines. At the same time, sea-level rise can accelerate other coastal processes such as erosion, and it can be, in turn, affected by subsidence.

According to the National Oceanic and Atmospheric Administration (NOAA), global sea level has been observed to be rising at an average rate of 3.2 mm/year. However, since sea level can be augmented by subsidence, relative sea-level rise along the Gulf Coast have been measured to be larger in specific gauge stations. At the Freeport tide gauge station, the rate calculated by NOAA since 1954 is 4.35 mm/year. Furthermore, the geology of the coastal zones also has a direct influence on how the sea level affects coastal morphology. In our study area, the shoreline is considered to have a low sediment supply, therefore, the sea-level rise will continue to occur, and the long-term rate-of-change of the Texas coast will continue to be of erosional nature (Gibeaut et al., 2000).

The relative sea-level rise is tightly related to subsidence, as it can be amplified by the land sinking and sediment consolidation. This relationship is especially important in our study area since a study by Swanson and Thurlow (1973) concluded that the sea-level rise in Freeport, Texas is caused mainly by subsidence. This is very important when taking into consideration that subsidence in the Houston greater area is of main concern, and is largely caused by groundwater withdrawal. Although there is no public documentation on subsidence of our study area, as Brazoria County becomes more populated and developed, there is an expected increase in groundwater pumping, and therefore subsidence.

2.3.2 Storms and Flooding

Tropical storms and hurricanes, which may lead to abnormal surge height, have a substantial effect on the reworking of sediments in coastal areas (Paine et al., 2013). Storms are responsible for most of the short-term changes in coastal areas (Morton, 1977). Major storms can disrupt normal coastal processes, and substantial sediment rework and erosion can occur. Beach erosion is common after storms due to the effect of the surge height.

From the 1850s to the 2000s, the coast of Texas has been affected by 120 hurricanes and tropical storms (Roth, 2010). In 2008, Hurricane Ike had a large effect on the Texas coast. It made landfall near Galveston Island where the largest storm surge was recorded. The coast area around the Island lost about 100 ft. of shoreline. During our study period, only two tropical storms and hurricanes have directly or indirectly affected Texas coast. In June 2015, Tropical Storm Bill made landfall on Matagorda Island, and the highest storm surge was recorded in Port Lavaca, south of Freeport, where it was measured to be 3.5-ft high. In Galveston Bay and Freeport, the storm surge was recorded at 3.42 ft. and 3.04 ft., respectively. Moreover, the remnants of Hurricane Patricia also affected the Texas coast in October 2015, in which the rain was the main factor affecting southern Texas; nine inches of rain were recorded in the Houston area.

Besides major hurricanes and tropical storms, several historical rain and flooding episodes related to storms have affected the Houston and Freeport area. Most recently, the Memorial Day Weekend flood and the Tax Day flood affected the southern Texas region. On April 18, 2016, the Tax Day flood affected the Houston greater area, as well as Freeport, Texas. According to the USGS Water Resources, the Brazos River gauge station at Richmond (USGS 08114000), Texas, which has been historically referenced to in studies of the Texas coast, surpassed the National Weather Service's (NSW) flood gauge of 48 ft. (Figs. 2.6 and 2.7). The Memorial Day Weekend rain on May 25 and 26 of 2015 also caused major flooding in the Houston Metropolitan area which received as much as 11 inches of rain throughout the weekend.

At the Richmond gauge station, the flood stage was surpassed a total of nine days during 2015 (May to June), and 16 days during 2016 (April to June) (Fig. 2.7). Historical crest was reached on June 02, 2016 where it reached 54.74 ft., surpassing major flood stage. These flooding episodes were expected to have large effects in the results of this study as more sediments were brought by the river channel, while storm waves reworked the coastal sediments.



Fig. 2.6: Gauge stations. The flood stages of the Richmond and the Rosharon stations at the Brazos River were used in this study to determine the periods in which flood stages were surpassed as the result of severe flooding.

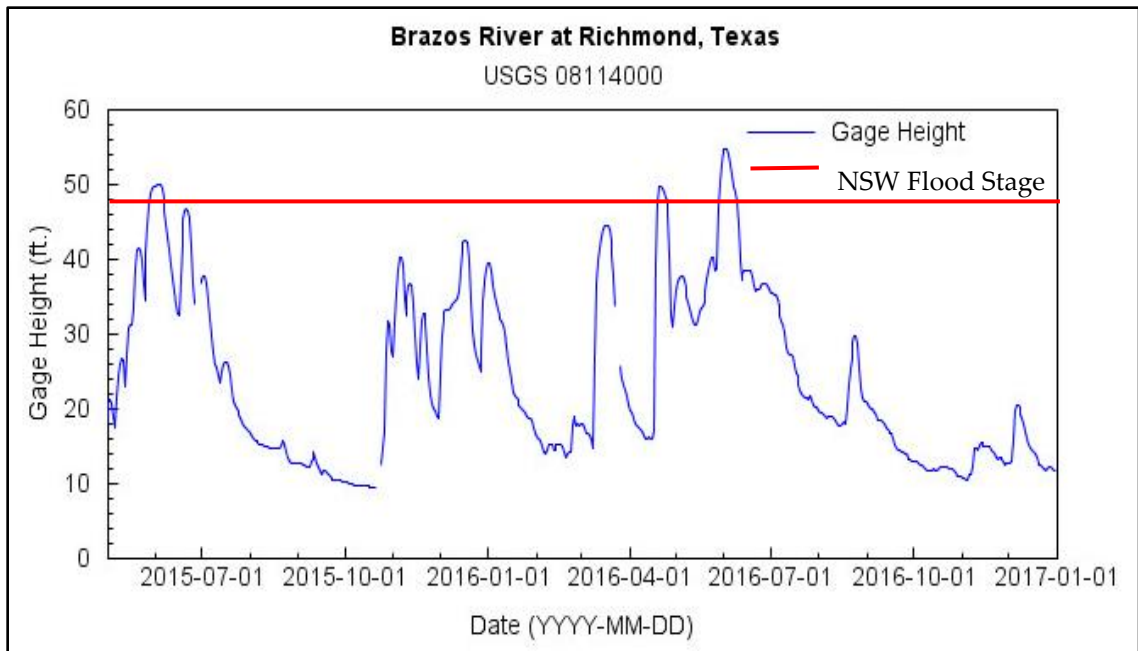


Fig. 2.7: Gage height at the Brazos River at Richmond, Texas. Gage height at the USGS gage station in the Brazos River at Richmond, Texas. Data shows water level at the station, and the flood stage positioned at the 48 ft. mark. Data ranges from March 01, 2015 to January 01, 2017. (Data source: USGS National Water Information System).

Closer to the mouth of the Brazos River delta is the USGS gauge station at the Brazos River near Rosharon, Texas (USGS 08116650) with a flood stage of 43 ft. (Figs. 2.6 and 2.8). The station reached a historical height on June 6, 2016, where it went to 52.56 ft. Other more recent crests were reached on April 24, 2016 (51.04 ft.), March 18, 2016 (47.47 ft.), and May 23 and 05, 2015 (48.47 ft., and 51.46 ft., respectively).

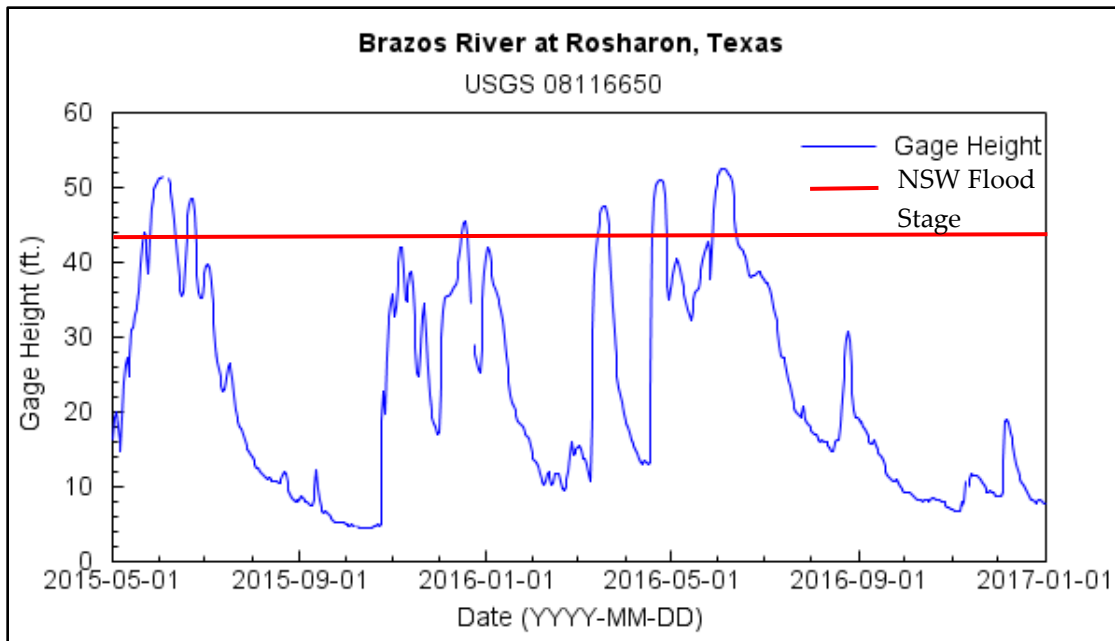


Fig. 2.8: Gage Height at Brazos River at Rosharon, Texas. The graph shows the water level at the station, and the flood stage positioned at the 43 ft. mark. Data ranges from March 01, 2015 to January 01, 2017. (Data source: USGS National Water Information System).

2.3.3 Human Causes

Human activities can also have a direct or an indirect effect on coastal morphological changes. Intervention might affect the sediment influx and transport processes in the coastlines. Changes in coastal areas brought by humans can be of two types; interference by coastal structures, and interference by other activities that can, in turn, affect local geologic and climate settings (e.g., groundwater depletion, oil extraction, and activities changing global climate, and sea level).

Human-made coastal structures are one of the most common causes of morphological changes in beach areas. These structures include seawalls, jetties, ports, or groins, and they are made to protect from beach loss. However, counter effects can be seen in areas surrounding these structures. Although the beach grows on the updrift side of groins and jetties, there can be significant sand loss on the downdrift side since sediment transport along coasts is driven by the prevailing current direction. Moreover, sea walls can cause an increase in erosion near the beach areas that are not protected by it, and they can also displace the beach which it protects and halt its natural migration. The nearest human-made structures to our study area are the Galveston sea wall and the jetties constructed at the entrance of the Freeport Harbor Channel north of the Brazos River delta (at the location of the old Brazos River delta) (Fig. 2.9). The east part of the jetties experienced accretion since their construction in the 1880s, and the west side experienced erosion.

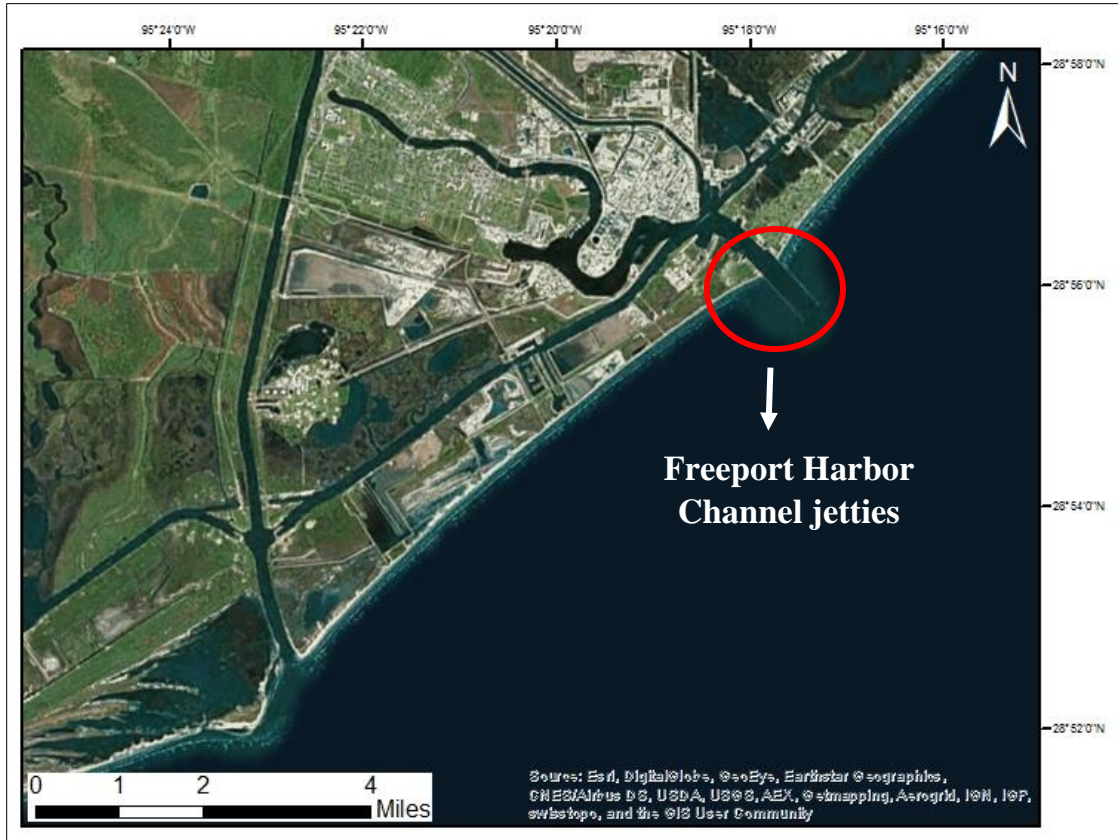


Fig. 2.9: Closest man-made structure to the study area. Scaled aerial imagery of the nearest jetties to the Brazos River delta and Bryan Beach located at the mouth of the Freeport Harbor Channel.

Nourishment of beaches is a way to replenish the beach with sand and to contour the effects of sediment loss. Nevertheless, this is not a permanent solution to sediment starvation. At Bryan Beach, there have been three nourishment programs since 2003 emplaced by the CEPRAs (Coastal Erosion Planning and Response Act) Beach Monitoring Program and Coastal Habitat Restoration GIS (CHRGIS) (Fig. 2.10). The most recent nourishment was done in February of 2016 to aid beach replenishment after Hurricanes Ike and Rita. However, no official

documentation quantifying the effects of the nourishment programs has been published.



Fig. 2.10: Nourishment programs near the study area. The figure shows two of the three most recent nourishment programs north of the study area, near the Freeport Harbor Channel (modified from the Conrad Blucher Institute for Surveying and Science, 2017).

2.4 Coastal Seasonal Changes and Beach Profiles

Besides morphological changes due to climate and human factors, beaches also undergo seasonal changes between the summer and the winter. These seasonal morphological variations are usually due to the change in storm frequency and waves' height and energy from one season to another.

As the wave energy increases during the fall and the winter, they produce an increase in sediment loss. In response, the beach berm and the dunes are prone to erosion, and sand can be transported offshore. This can also lead to the formation of an offshore sand bar. During the winter months, the beach profile looks steeper with a narrow berm (Fig. 2.11). On the other hand, during the summer months, waves tend to be gentler and calmer, allowing for a recovery period where the sand returns to the beach after the winter erosion-prone period. During this time, the beach profile looks gradual and gentler in contrast with the “winter” beach (Fig. 2.11). Also, accretion usually occurs, and beaches grow as sand accumulated offshore returns to the coastal area.

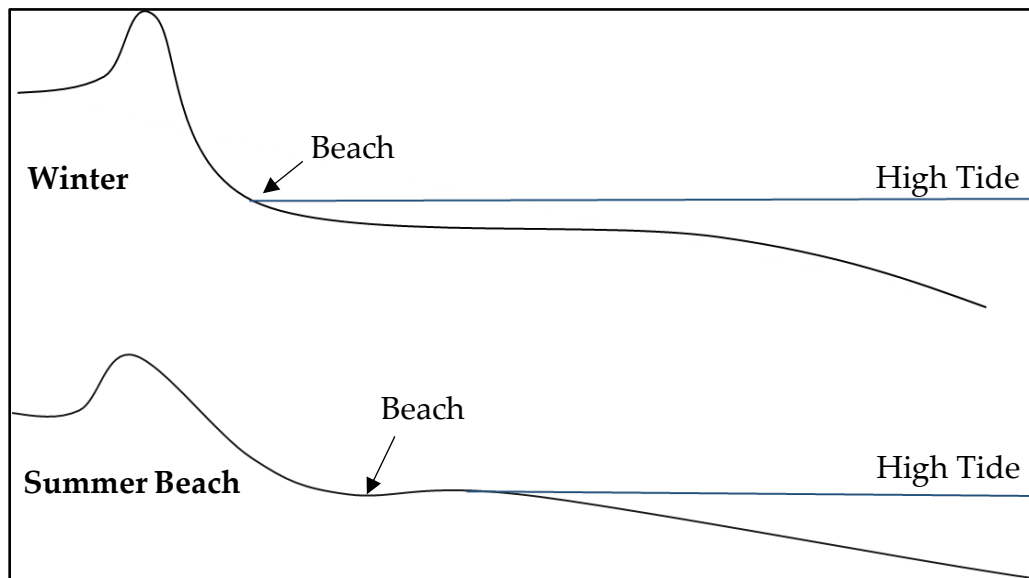


Fig. 2.11: Seasonal beach changes. The diagram shows the changes experienced by beaches from one season to another. The winter beach has a narrower beach and a steeper dune-beach profile, while the summer beach exhibits a recovered beach berm with a wider beach and a gentler beach profile.

Although our study area was highly affected by storms and floods during the summer months of our study period, some seasonal changes could be observed from the Summer 2016 beach to the Winter 2016 beach (Fig. 2.12)



Fig. 2.12: Coastal seasonal changes exhibited in our study area. The figure above shows the difference between "summer" and "winter" beaches. While the "summer" 2016 beach has a wider beach berm, the "winter" 2016 beach is narrower with a steeper profile.

Although these changes tend to be seasonal, events such as hurricanes or floods can disrupt the pattern. In the case when the retreated sand during the winter months exceeds the beach recovery in the summer months, overall erosion is characteristic in the beach. The opposite also holds, and if the overall recovery period is greater than the winter erosion, the overall beach accretion is characteristic. In some cases, the vegetation line can sometimes be buried, and a longer period of recovery is needed for it to grow back through the sand.

Moreover, the location of sand deposition after erosion also affects whether the beach will achieve equilibrium in the following summer months. The winter erosion can transport the eroded sand to a temporary offshore bar, to a different coastal location due to longshore drift, or across the barrier island (Morton and Pieper, 1975). The main case when removed sand is able to return to the beach during the regular seasonal pattern is when the sediments are deposited in an offshore temporary bar.

The coastal seasonal changes can be easily observed by looking at beach profiles (Fig 2.11). These profiles are prone to the highest short-term changes during and after storms when the storm surge and duration have the greatest effect on the topographic features of the area (Morton and Pieper, 1975). For a beach to recover after winter storms and erosion, enough sediments should be

available. Nonetheless, the vegetation line adjustment to pre-storm conditions can take longer (up to several months) than the shoreline adjustment. According to Morton and Pieper (1975), the beach and vegetation line recovery period follows the timeline: (1) beach accretes as sand returns, (2) sand mounds form in the beach berm, (3) sand mounds merge with the foredune, and (4) the vegetation line migrates to its pre-storm location. If there is not enough sand then neither the shoreline nor the vegetation line would recover to their pre-storm positions.

Chapter 3 Introduction to LiDAR and GPS

3.1 LiDAR Introduction

Light detection and ranging, also referred to as LiDAR, is an active remote sensing technique in which laser pulses are used to measure the distance to surface targets. Range measurements allow for the generation of point clouds with three-dimensional information about the terrain surface. Its first application dates back to the 1960s when laser ranging technology was used to measure distances to clouds (Killinger, 2014). In the 1970s, LiDAR was first used in space as laser altimeters, and in the 1990s the first commercial LiDAR systems were developed. Nowadays, LiDAR data can be collected from planes or from stationary platforms, and the technology has applications in a wide range of fields such as geology, archaeology, military, forestry, geomorphology monitoring, and surveying, among others (Asner et al., 2012; Jaboyedoff et al., 2012; Telling et al., 2017; Johnson and Ouimet, 2014).

LiDAR is able to compute the distance to the surface targets, and therefore to produce their 3D coordinate representations. Most instruments calculate ranges from the two-way travel time of the laser, the angle at which the light pulse was transmitted, and the sensor location (NOAA, 2008). The sampling rates vary per

instrument, and they can range from 30,000 to 400,000 pulses per second. The vertical and horizontal accuracy also depends on the instrument and the type of platform from which the dataset is collected.

3.1.1 Laser Ranging and Scanning

The LiDAR technique incorporates a transmitter which generates and sends out laser pulses. When the laser pulses hit and reflect back from the surface to the instrument, the receiver collects the reflected laser light. The incorporation of a rotating mirror allows for a simple terrain profiling instrument to become a scanner device that can measure topographic features rather than just 2D-vertical profiles of the surface (Shan and Toth, 2009). Therefore, with the rotating mirror's azimuth motion the collection of multiple vertical profiles of the range to the target surface is possible. There are two methods to calculate the range to targets, by measuring the phase difference of a continuous laser beam sent and received by the instrument, and by calculating the time-of-flight of the laser pulses. The most basic method for measuring range is the latter, and it involves accurately measuring the time interval from the moment the pulse is emitted to its return to the instrument (Fig 3.1). It follows that:

$$R = \frac{vt}{2}$$

where R is the range, v is the known speed of electromagnetic radiation, and t is the measured time for the pulse to be transmitted and reflected back to the scanner.

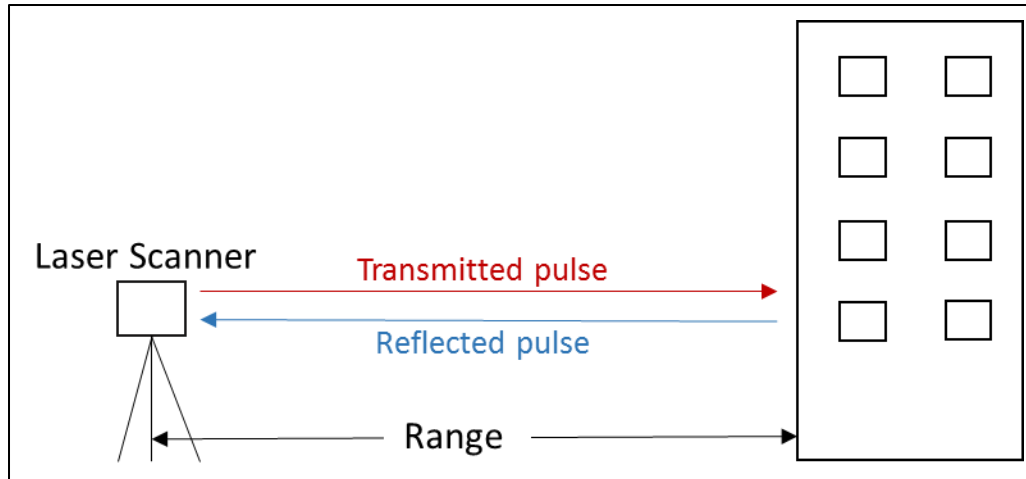


Fig. 3.1: Diagram of LiDAR principles. The diagram shows the principle of the operation conducted by scanners that measure range through the time-of-flight method.

LiDAR laser pulses are generally ultraviolet, visible, or near-infrared light. There are two factors to consider when addressing the ranging performance of the scanner and that also affect the important task of site selection and coverage at the time of survey planning, divergence and reflectivity (Shan and Toth, 2009). After the light is emitted from the instrument, it spreads out in a circular or elliptical way. As the laser moves farther away from the instrument, the diameter of the circular area becomes larger, and it covers a larger surface area. The quality of the signal reflected back to the scanner is characteristic of all of the materials that fall within the circular area the beam illuminates. Manufacturing companies generally

provide beam divergence information for their scanners. For example, the laser beam divergence of the scanner used in this study is 0.3 mrad which corresponds to a beam diameter increase of 30 mm per 100 m (Rieggl, 2016a).

Another aspect to consider regarding ranging performance is the reflectivity of the objects and earth surface materials. The strength of the returned signal depends on the backscattering or reflectance properties of the reflecting material. Moreover, the reflectance properties also affect the maximum range of the scanner. Manufacturer companies even provide the maximum measurement range depending on the minimum reflectivity of natural targets. For example, Rieggl, the manufacturing company of the instrument used in this study quotes maximum measurement ranges seen in Table 1. Ideally, the reflecting surfaces are considered to be hard surfaces with the maximum reflection being perpendicular to the target plane.

Table 4. Maximum range measurements in meters for the Rieggl VZ-2000 scanner instrument. These are values for average conditions, flat targets, and perpendicular angle of incidence.

<i>Natural Targets</i>	<i>Maximum range (m)</i>				
$\rho \geq 90\%$	2050 m	1800 m	1000 m	750 m	580 m
$\rho \geq 20\%$	1050 m	930 m	500 m	370 m	280 m

Moreover, the reflectivity of specific targets depends on the laser pulse wavelength emitted by the instruments, and they can change when considering a varying remote sensing source such as the sun versus an instrument that is capable of sending pulses with specific wavelengths (Shan and Toth, 2009). The Riegl company has also published the reflectivity of some materials. For example, the reflectivity of beach sand for a wavelength of 0.9 micrometers is around 50% (Riegl, 2016a)

3.1.3 Terrestrial Laser Scanner

The evolution of terrestrial laser scanning (TLS) technologies has lagged behind airborne laser scanner (Buckley et al., 2008; Shan and Toth, 2009). However, the technique has progressed greatly and leveled out with airborne data collection with the TLS advancements in accuracy, precision, functionality, and measurement rates (Telling et al., 2017). Nowadays, the technique is widely accepted by the scientific community, and multiple ground-based LiDAR studies have been carried out in a wide variety of applications such as outcrop modeling, landslide monitoring, terrain change studies, and flood modeling. While being more accurate than airborne LiDAR due to the shorter distance measurements, terrestrial laser scanning also has the ability to produce robust and massive 3D representation of the earth surface (Telling et al., 2017).

There are two types of TLS systems, static scanners, and dynamic scanners. The instrument used in this study is a long-range static terrestrial laser scanner which is attached to a fixed position on the surface. Moreover, TLS instruments can be further classified depending on their scanning mechanisms and their coverage. They are classified as (1) panorama scanner, (2) hybrid scanner, and (3) camera scanner (Shan and Toth, 2009). While the hybrid and the camera scanners have limited angular range, the panorama scanner, which is used in this study, has a 360° coverage in the horizontal plane. As mentioned before, the instrument requires a rotating mirror to collect multiple and simultaneous range measurements in the vertical direction. The angular intervals in which the mirror rotates to take angular measurements can be set up by the user, while the angular and horizontal range angles, as well as the measurement rates, depend on the instrument used.

3.1.4 LiDAR Application on Coastal Topographic Studies

As mentioned before, the TLS technology is becoming robust and practical enough to be applied in a wide range of fields. Airborne laser scanning (ALS) has been widely used in coastal monitoring studies in order to generate 3D-representations of the Earth such as digital elevation models, and to aid the evaluation of morphological changes in beach areas. However, for small areas and

short-term studies, TLS proves to be an affordable, precise, practical and accurate technique (Santos et al., 2014; Buckley et al., 2008; Kandrot, 2013; Fairley et al., 2016; Lee et al., 2011). The detailed and massive information obtained along with the practicality in the TLS survey performance facilitates monitoring studies, and have made terrestrial laser scanning a routine technique in geologic studies involving highly dynamic environments (Fairley et al., 2016). Although TLS methodological practices are still in its early stages of developed when compared to ALS, there has been significant advances in the area. As mentioned in Telling et al., 2017, multiple publications offer guidelines and methodologies which are mostly meant to meet the requirements for each study's purpose, and the applications has widen to multiple fields such as geomorphology, spectral geology, volcanic, tsunami and earthquake hazard studies, and landslide applications, among others. The study also presented several TLS applications in coastal geomorphology which include the analysis of marsh morphology, beach volume, sea cliff erosion, swash zones dynamics, and even wave morphology.

Since TLS surveys yield massive and dense 3D-point clouds with XYZ coordinates which have very high-temporal resolution, they aid coastal monitoring studies where vast details are necessary (Fairley et al., 2016). From point clouds, digital elevation models can be generated to evaluate 3D-coastal

features, and ultimately offer conclusions regarding morphological changes and morphological patterns. Although authors differ in methodologies to obtain DEMs, the ultimate goal is the extraction of coastal features throughout time series from the 3D representations. Once the DEMs are generated, analysis of the dataset is done through the defined topographic features that help to quantify coastal morphological change. Historically, the quantification of coastal change depends on the extraction of features such as shoreline, vegetation line, and dune ridges. This study used these features' definitions in order to extract them from the DEMs and analyze them. Moreover, other information such as volume change and profiles were extracted as well to investigate seasonal coastal changes.

3.2 GPS Introduction

Global Positioning System (GPS) is a US-owned global navigation satellite system that provides positioning and navigation to users. The system was created by the United States in the 1960s originally for military applications after the Soviet Union launched Sputnik, the first man-made satellite. The system is based on the known position of satellites, and the signals with time and location information that they sent to the Earth. After receiving time and location information from the satellites, the receiver is capable of calculating the distance to the satellites and its location.

The system consists of three segments: the space segment, the control segment, and the user segment. The space segment consists of the satellites that transmit signals to the Earth. In order to provide accurate positioning to the user, at least four satellites must be in range of view to the receiver. The space segment is designed to have six orbital planes with four satellites each, which ensures the visibility of at least four satellites from any point on the Earth. The control segment is in charge of tracking the satellites and monitoring their signal transmissions. The segment includes a master control station, an alternate master control station, four ground antennas, and six monitoring stations. Finally, the user segment includes the civil, military, commercial, and scientific users of the device.

3.2.1 GPS and TLS Integrated Techniques

Since the underlying goal in morphological change studies is the multi-temporal comparison of datasets, there is also the fundamental requirement of registering each scan to determine their correct position relative to other scans, and in some cases relative to a global coordinate system. For this purpose, control points can be used in multiple scans for registration. Registration allows data to be combined in a single coordinate system. In most TLS studies, registration corresponds to the first step in data processing, and it involves the use of GPS data acquired in the field survey. One of the most common registration methods and

the one used in this study involves using a reference point matched to more than one scan throughout the study area. This approach uses a common control or reference point in multiple scans to correct them and adjust them to a common coordinate system. This technique will be further explained in section 4.3.3.

GPS is also used in TLS studies to determine the accuracy of the survey. The kinematic or real-time kinematic (RTK) GPS techniques can be used to assess the precision of the TLS survey and to correct for errors (Mitasova et al., 2009; Muhadi et al., 2016). The errors related to common GPS practice are related to errors in the satellite clock, the satellite orbital, ionospheric and tropospheric delay, and these are sought to be canceled out using GPS methods. RTK GPS is a differential global positioning technique which improves precision and accuracy by removing positioning errors. RTK provides corrections in real time based on a single reference station. Regular GPS units use code-based positioning, in which the range from the receiver to at least four satellites, along with the satellites' location allow the receiver to establish its position. RTK, on the other hand, uses carrier-based ranging, in which the carrier wave's phase is used to determine precise positioning.

This enhancing system uses two or more GPS units, where one of the units remains stationary (base station) in a known reference point and the other unit(s),

referred to as rover, is moved from one place to another. Rather than using the information that the satellite sends in its signals, the technique uses measurements of the phase of the signal's carrier wave (such as phase measurements or the number of carrier cycles from the satellite). This method assumes that the Global Navigation Satellite System (GNSS) signal processing errors are constant. While the base station located in the reference point calculates the errors between its own position relative to its actual location, it sends out the error corrections to the rover(s). This technique is widely used in TLS surveys, where the highly accurate RTK GPS survey points are used to assess the accuracy of the laser scanner points. A similar type of GPS survey, called kinematic GPS, can also be performed for the same purpose. This technique allows the user to collect GPS data continuously from a moving platform.

Although accuracy in TLS surveys is initially specified by the manufacturer of the instrument, the actual accuracy can be affected by factors such as environmental conditions (wind, rain, and temperature), objects' reflectivity, range, and laser's angle of incidence, among others. Consequently, each TLS survey yields accurately different results. In order to assess accuracy, some TLS surveyors carry out kinematic GPS surveys in order to compare elevation values between the two datasets. Cloud points or DEM elevation values and GPS datasets

that share the same coordinates or that are close to each other are selected for comparison, and the RMSE values are obtained in order to determine the accuracy of the TLS dataset. This process is further explained in section 4.3.4.

Chapter 4 Data Acquisition and Processing

4.1 LiDAR Instrumentation

The TLS instrument used in this study is a Riegl VZ-2000 (Fig 4.1), which uses the near-infrared laser to illuminate targets and create 3D representations of the visible surface. The specifications of the scanner are seen in Table 2.

Table 5: VZ – 2000 by Riegl Specifications.

Class 1 Laser	Near-infrared
Beam Divergence	0.3 mrad
Pulse rate	$\leq 400,000$ meas./sec
Field of view	$100^\circ \times 360^\circ$
Accuracy *	8 mm
Precision	5 mm
Range measurement	Time-of-flight

** 150 m range*



Fig. 4.1: TLS instrument. The figure depicts the terrestrial laser scanner used in this study. A VZ-2000 by Riegl company is used with a digital camera and a GPS R10 unit mounted on top.

The VZ-2000 includes a high precision mount for a digital camera, an electronic compass, and inclination sensors. An integrated L1 GPS can be replaced by an external dual-frequency GPS unit mounted on top of the instrument.

The instrument is comprised of a fast rotating polygon mirror which deflects the light into the Earth's surface. Consecutive measurements from the rotating mirror are called a scan line. The slower rotating optical head, which is the top part of the scanner, rotates slower than the mirror to measure in a scan movement called a frame scan which can cover 360°. The users can configure both the angular ranges of the scan line as well as the frame scan.

Point clouds are originally stored in the Scanner's Own Coordinate System (SOCS), in which the laser source is set as the origin of the Cartesian coordinate system (0, 0, 0). This way, the optical head rotates in the XY plane, and the rotating mirror deflects the laser pulse in the plane perpendicular to the XY plane (Fig. 4.2). In order to define the directions of the X, Y, and Z axes, the scanner is equipped with inclination sensors which measure the tilt angle between the horizontal plane and the SOCS. In turn, the SOCS can be transformed to a geographically and leveled coordinate system by using the roll, pitch and yaw angles between the scanner planes and the horizontal and vertical planes. In our study, the external GPS unit was used to transform SOCS to a Global Coordinate System (GLCS) in order to be able to register the datasets that vary in a temporal and spatial manner.

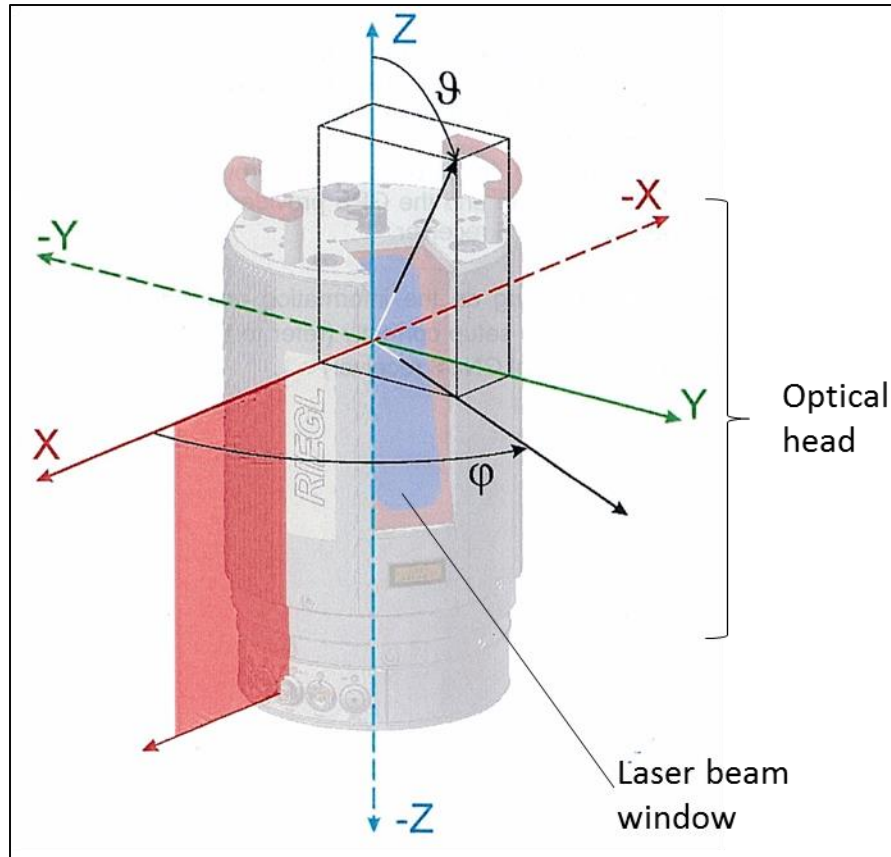


Fig. 4.2: Scanner's coordinate system diagram. The figure shows the Scanner's Own Coordinate System (SOCS), and its key components (modified from Riegl, 2014)

4.2 GPS Instrumentation

Two Trimble R10 GNSS units were used in the TLS survey (Fig 4.3). One was mounted on top of the LiDAR instrument, and the other one was mounted on top of the reflector used for registration purposes. The same instrument was used separately to perform one portion of the point cloud and DEM accuracy assessment. Advantages of this instrument include its low size and weight which

lessens field time. The instrument is able to measure continuous RTK data and to establish wireless connections with a remote controller.



Fig. 4.3: R10 GPS unit. The GPS units used in this study are manufactured by Trimble, and its advantages include its low weight and the easiness to establish a connection with a remote controlling device.

Furthermore, a Trimble Net R9 receiver and Zephyr Geodetic II antenna pair were used to perform the second part of the accuracy assessment (Fig. 4.4). The receiver allows for a web interface configuration of the survey, and connections can be established through Bluetooth, USB wire, or Ethernet port. The usage of this instrument is later explained in section 4.3.4



Fig. 4.4: Trimble Net R9 receiver and Zephyr Geodetic II antenna. The pair was used for the kinematic GPS survey performed for accuracy assessment purposes.

4.3 Methods

The tasks in this project include: (1) perform a TLS survey where terrestrial LiDAR data is acquired over the defined study area in a biannual manner, (2) generate digital elevation models of the study area from the TLS datasets, (3) extract coastal features and beach profiles in order to derive morphological changes, (4) and generate a methodology to collect and process TLS datasets for coastal morphological studies.

4.3.1 GPS Data Acquisition and Processing

GPS data was acquired simultaneously with LiDAR data for the purpose of TLS data registration and georeferencing, and the assessment of the survey's accuracy.

For the TLS survey, one R10 GPS unit was mounted on top of the TLS instrument, and the other one was mounted on top of the reflecting reference point (Figs. 4.5 and 4.6). GPS data for the scan positions was acquired continuously for over 20 minutes at each location, while the GPS data for the reflecting position was collected for over two hours at each location. The reflecting reference point with the mounted GPS was located less than 1000 m away from the scan position, and the same reference point location was used for at least two scans.

Raw R10 GPS data was processed using the Online Positioning User Service (OPUS) by the National Geodetic Survey (NGS). OPUS allows the end user to upload GPS data in RINEX format (Receiver Independent Exchange) and provides coordinate results for the NGS' Continuously Operating Reference Station (CORS). Besides uploading the RINEX files, information about the antenna type and height should be set by the user for more accurate results. In this case, the reflector antenna height was set to be 0.25 m which corresponds to the height from the bottom of the R10 to the center of the reflector, and 0.307 m for the TLS instrument which corresponds to the height from the R10 bottom to the center of the scanner. UTM coordinates results for the reference points and scan positions were used to register all scans, and to relate the project coordinate system to a global coordinate system. The usage of the GPS datasets is explained in depth in

the Point Cloud and DEM Data Accuracy Assessment and Registration sections of this thesis.



Fig. 4.5: The reflector or reference point with a GPS unit. One of the R10 GPS units was mounted on top of a reflector which was used for registration purposes of the TLS datasets.



Fig. 4.6: GPS survey on the dune area. The reflector points were positioned alternately on the beach area and the dunes.

For the kinematic GPS survey, both the R10 and the R9 GPS units were used. The R10 unit was used to perform an RTK GPS survey across the dunes in the region (Fig. 4.7), while the R9 was used to perform a kinematic survey across the flat-beach area (Figs. 4.8 and 4.9). While the R10 was mounted atop a pole, the Zephyr Geodetic II antenna was mounted atop a moving vehicle by using a custom-made connecting structure.

The kinematic GPS dataset was processed using the Automatic Precise Positioning Service of the Global Differential GPS (GDGPS) System from NASA's

Jet Propulsion Laboratory. The system allows the user to upload static or kinematic datasets, and uses Gipsy Oasis software to process the data. APPS' expected positioning accuracy of a kinematic survey is less than 5 cm.



Fig. 4.7: GPS survey near the dune area. The R10 GPS unit was used to perform a GPS survey near and through the dunes of the study area.



Fig. 4.8: Kinematic GPS Survey. The figure shows the car used for the kinematic GPS survey, and the instrument mounted on top. The Zephyr Geodetic II antenna was mounted using a custom-made adapter, while the receiver was kept inside the car.



Fig. 4.9: Antenna used for the kinematic GPS survey. The picture shows the Zephyr Geodetic II antenna, and the adapter used to mount the antenna on top of the car.

4.3.2 LiDAR Data Acquisition

TLS data was acquired in the study area in four biannual consecutive collection cycles: summer of 2015 and 2016, and winter of 2015 and 2016. Multiple scans were performed in the beach strip of the study area. Table 3 shows the number of scans per collection cycle, the number of days the surveys were carried on for, and the number of scans that were considered admissible for the study. Some scans were

not taken into account for this study on the basis of the scanners' location with respect to the reference points or OPUS' reference stations.

Table 6: TLS surveys' information.

	<i>Survey dates</i>	<i>Total Scans</i>	<i>Admissible scans</i>
Summer 2015	May 19 – May 26	51	39
Winter 2015	Dec. 9 and Dec. 16	12	11
Summer 2016	May 19 – 21, 23 – 24	45	39
Winter 2016	Dec. 06 – Dec. 07	14	14
<i>Total</i>	<i>17 days</i>	<i>122</i>	<i>103</i>

To perform the scans, the instrument was mounted on a 4 m elevation tripod (Figs. 4.10 and 4.11). A total of 103 scans were admissible for the TLS survey, however, the study area was limited to over a 2 kilometers strip of beach along the Texas coast, and less than 70 scans were specifically used in this study. Fig. 4.12 shows all of the TLS scan positions throughout the period of data collection.

The scans were done in alternating locations; one scan was done in front of the dunes, and the next one was performed in the back of the dunes and so on for better coverage purposes. In some occasions, the scanner was positioned on the dunes. The reference points were always positioned so that they were within the range of the scanner; however, it is worth noting that during the summer collection

cycles, the high influx of beach-goers and vehicles represented a limitation for the survey and the accurate positioning of the reference points. The reflecting car windows and other objects were in many times drawbacks for the correct scanning and proper identification of the reference points.



Fig. 4.10: TLS data acquisition. The figure above depicts the team collecting TLS data next to the Brazos River delta. The VZ-2000 was mounted on top of a tripod, while the R10 GPS unit was mounted on top of the scanner and the camera.



Fig. 4.11: TLS survey in the coastal area. The figure depicts the VZ-2000 instrument being mounted on the tripod at a high ground position on the dunes.

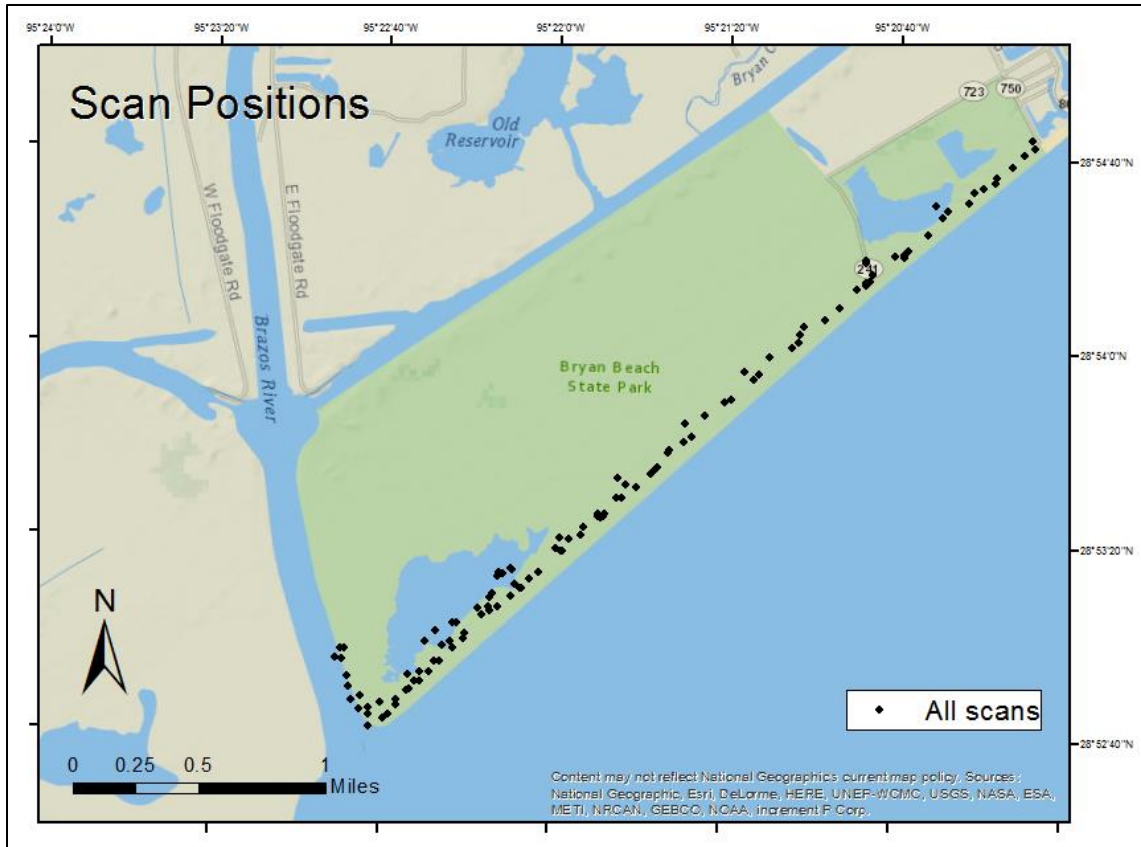


Fig. 4.12: Scan positions in the coastal area. The map shows the scan positions in the beach strip from Summer 2015 to the Winter 2016 collection cycle.

The software that accompanies the instrument, RiSCAN Pro (V2.2.1), was used to perform the survey and set up its parameters. The software was used during data acquisition, data storage, for data organization purposes, and for the first processing part of this study. The parameters needed to be set for this study were the resolution in degrees, set at 0.04° , and the measurement program which was generally set at 1800 m or 100 kHz. Other parameters that can be set are the picture acquisition mode, and the start and stop angles of the scan. The point clouds could be immediately accessed after data collection using the RiSCAN Pro software to

examine the coverage and success of the scan (Fig. 4.13). In our study area, black areas with no data points can mean water areas as well as no-coverage zones in areas such as the backdune or the rough terrains (Fig. 4.13).

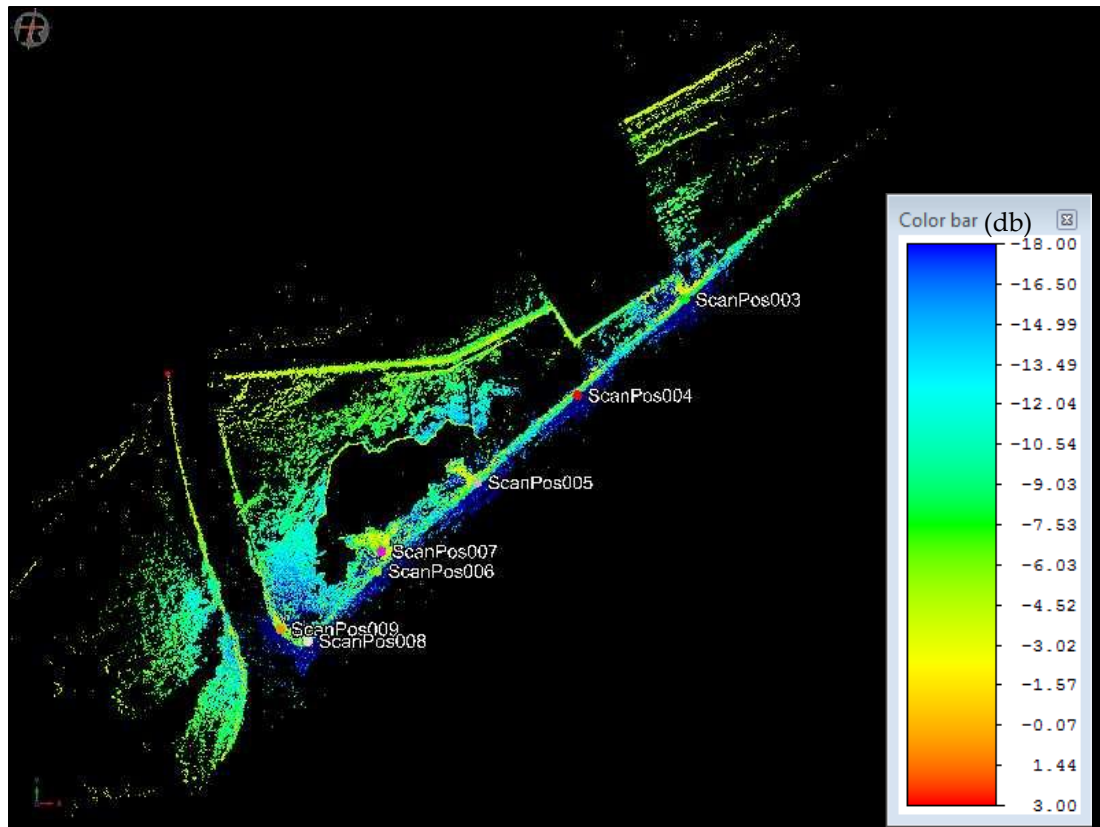


Fig. 4.13: Point cloud from the Winter 2015 collection cycle. The point cloud was retrieved after data collection on December 09, 2015, and it shows reflectance intensity values in dB.

4.3.3 TLS Data Processing

After data collection, raw LiDAR data must be processed in order to generate DEMs. There are two key elements in data processing which involve the scan registration and georeferencing, and the conversion to a final product used for the analysis of the dataset (Telling et al., 2017). Since producing DEMs involves the

interpolation of data points into a continuous dataset, raster cells or grids with a defined size must be created. This study provides a workflow for data processing, which includes the application of three software tools. RiSCAN Pro, the software package that accompanies the VZ-2000 instrument was used for data acquisition, pre-processing, and registration. Moreover, the Generic Mapping Tools (GMT) was used for TLS data processing and DEM generation. Final DEMs of the study area were visualized and analyzed using ArcGIS' tools, where extraction of the coastal features was performed. A workflow of the processing steps is provided in this study.

- Registration

The generation of DEMs for multi-temporal comparison as a goal for this study motivates the horizontal precision and accurate registration of overlapping point clouds (Shan and Toth, 2009). Since it is required to cover the entire study area, multiple scans were carried out over several days and each of them was referenced to the instrument's coordinate system. Therefore, it is essential to convert the scans to a common coordinate system to produce a composite point cloud of the study area (Fig. 4.14). This process is called registration, and it produces a single dataset with combined scans. Furthermore, the registered datasets can be further

integrated into an external or geodetic coordinate system in a process called georeferencing.

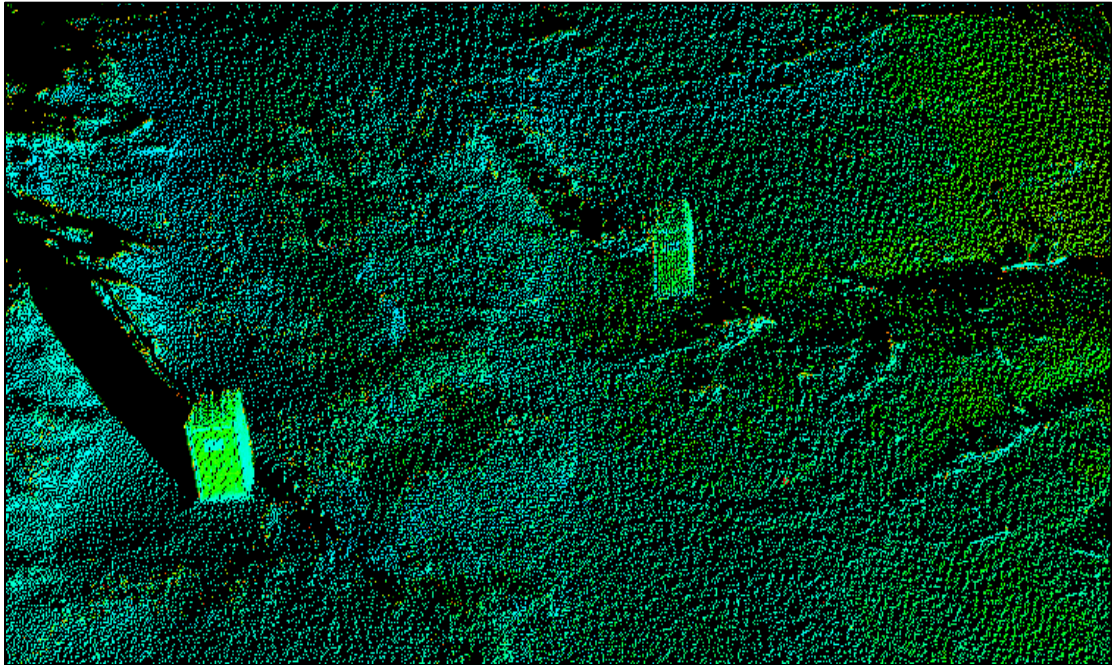


Fig. 4.14: Example of an “unregistered” point cloud. The figure shows an “unregistered” point cloud from two separate scans. The square object in the figure is a single portable restroom seen twice in the point cloud before the registration pre-processing step.

The registration includes the transformation from the Scanner’s Own Coordinate System (SOCS) to a Project Coordinate System (PRCS) which is accomplished by performing a rigid transformation through a rotation matrix. In turn, the rotation matrix can be described by three angles: the roll angle (rotation about the scanner’s x-axis), the pitch angle (rotation about the scanner’s y-axis), and the yaw angle (rotation about the scanner’s z-axis). The rotation matrix is then calculated from the angles such as:

$$R_x(R) = \begin{pmatrix} 1 & 0 & 0 \\ 0 & \cos R & -\sin R \\ 0 & \sin R & \cos R \end{pmatrix} \rightarrow \text{Roll matrix with roll angle } R$$

$$R_y(P) = \begin{pmatrix} \cos P & 0 & \sin P \\ 0 & 1 & 0 \\ -\sin P & 0 & \cos P \end{pmatrix} \rightarrow \text{Pitch matrix with pitch angle } P$$

$$R_z(Y) = \begin{pmatrix} \cos Y & -\sin Y & 0 \\ \sin Y & \cos Y & 0 \\ 0 & 0 & 1 \end{pmatrix} \rightarrow \text{Yaw matrix with way angle } Y$$

Therefore, the rotation of a point with SOCS coordinates (P_{socs}) is:

$$R = R_z(Y)R_y(P)R_x(R) P_{socs}$$

Although there are many methods to register point clouds, a technique called “backsight registration” was employed in this study. This registration technique uses the known position of a remote object and the TLS known location. GPS data is used for registration. The technique was selected due to the nature of the study. Since the study area represents a linear beach strip with high dunes and a rough trough terrain behind the dunes, the most affordable and manageable way to register the datasets was to use a single reference point. The technique allows the instrument to set the horizontal plane by using its inclination sensors, while the usage of a reference point defines its direction.

A cylinder reflector with a diameter of 20 cm and a height of 25 cm was used to correct the orientation of the scanner. A Trimble R10 GPS unit was installed on the reflector to position the reflector. The GPS unit was used so that a common

reference point can be established to define the survey's direction, and used to tie together separate scans. Once every scan is registered to its corresponding reflector, multiple scans can be tied together. For this study, at least two scan positions were registered to each reference point.

In this case, because we are using reference points and TLS' positions in a global coordinate system, the registration is directly done by transforming from SOCS to GLCS (Global Coordinate System). The common coordinate system was defined by the UTM Zone 15 in the horizontal plane, and the North American Vertical Datum of 1988 (NAVD 88) from the GEOID12B geoid model in the vertical plane.

- Terrain Filtering and Point Selection

Three other tools and filters were used in RiSCAN Pro to eliminate unwanted and unrealistic points of the dataset and to decimate the dataset. These tools included the point selection tool, the octree filter, and the terrain filter.

The point selection tool is an optional tool for different TLS surveys, and it is used to eliminate unrealistic points that are not representative of the true data or that are simply unwanted points. The software allows the user to set a window based on a variety of factors such as range or reflection to eliminate cloud points

within that window. The point selection tool was used in this study to eliminate distinctive and unrealistic data points surrounding the scanner.

A second tool was applied in RiSCAN Pro, the terrain filter. This filter eliminates off-terrain objects (e.g., cars, trees, or debris) based on an estimated ground surface and the distance between different data points. The filter analyzes the distances from points to the estimated ground surface and it classifies them as “terrain” or “off-terrain.” This is done in a hierarchic manner in which several levels of grid representation are used to estimate a representative cell point which at the same time is be used to estimate a local surface for each cell. A tolerance value is also established for each cell, and this value is used in order to determine off-terrain or terrain points.

Finally, the octree filter was used to diminish the size of the dataset. Since this study encompasses multiple scans, extremely large and dense point clouds can cause longer and even excessive processing time. The octree filter applies an iterative cube algorithm filter in which a cube is divided into eight cubes which at the same time is divided into eight cubes and so on. When the cube reaches a minimum size or when there are no more points within the cube, the division and thus the filtering stops, resulting in each cube containing only one data point in the center of gravity of the cube. For this study, there are more redundant points

in the horizontal direction than the vertical direction, thus a cuboid octree is used with the size of 10 cm in the X-direction (east-west), 10 cm in the Y-direction (north-south), and 3 cm in the Z-direction (vertical).

The two filters applied to the dataset are considered to be pre-processing steps that need to be performed in order to produce DEMs of the study area. Moreover, the filters used can significantly reduce the size of the data and ultimately they can minimize its processing time. For our datasets, the filters were capable of removing approximately 85% of the raw laser points.

- Decimation and DEM Generation

In order to produce DEMs of the study area, further manipulation of the data must be conducted. After data pre-processing, the Generic Mapping Tool software package was used in order to downsample and regrid the dataset and to produce the DEMs that were analyzed. GMT is an open-source collection of software command-line tools for the processing and manipulation of coordinate data (Wessel and Smith, 2016). A script provided by Xing et al., 2016, was used in order to remove anomalous points from the dataset, perform interpolation and anti-aliasing filtering, and to downsample the dataset to ultimately produce the DEMs.

After pre-processing the data using RiSCAN Pro, the data was exported in ASCII format with XYZ triplets. GMT allows users to manipulate these file formats and produce maps, graphs, or DEMs. The following functions by GMT were used to process the dataset.

➤ Rigid coordinate transformation

In order to maximize the use of the figure and save gridding time with plane boundaries that focus only on the desired study area, a coordinate transformation was performed. The UTM coordinates of the exported ASCII files were rotated 40 degrees anticlockwise while defining a new origin which was defined for convenience near the mouth of the Brazos River. This caused the X-axis to be positioned nearly parallel to the shoreline of the study area (Fig 4.15).

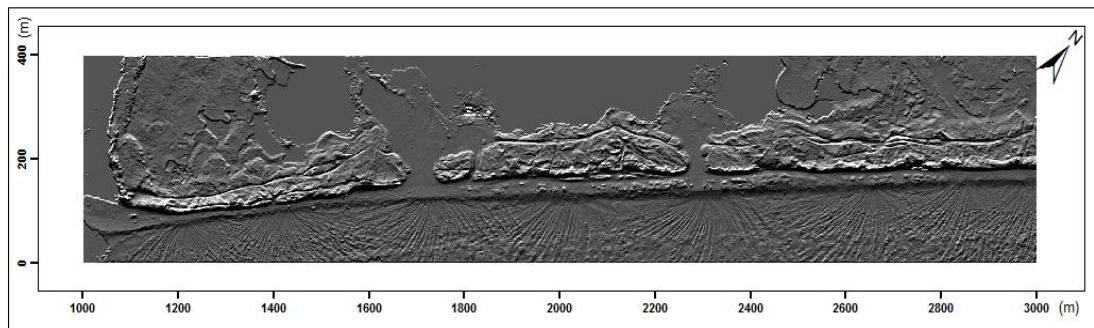


Fig. 4.15: Hill-shaded image of the study area. After a coordinate transformation, the study area possesses a new origin near the mouth of the delta and extends to 3000 m in the X direction, and 400 m in the Y direction.

The coordinate rotation was performed by using the following rotational matrix:

$$\begin{Bmatrix} x \\ y \\ z \end{Bmatrix} = \begin{bmatrix} \cos \theta & \sin \theta & 0 \\ -\sin \theta & \cos \theta & 0 \\ 0 & 0 & 1 \end{bmatrix} \begin{Bmatrix} e \\ n \\ z \end{Bmatrix}$$

where the point $P(x, y, z)$ in the new coordinate system is calculated from its location in the original system $P(e, n, z)$ according to the rotation degree θ . The rotation degree θ is counted from the original east axis. The anticlockwise direction is positive; the clockwise direction is negative (Fig. 4.16).

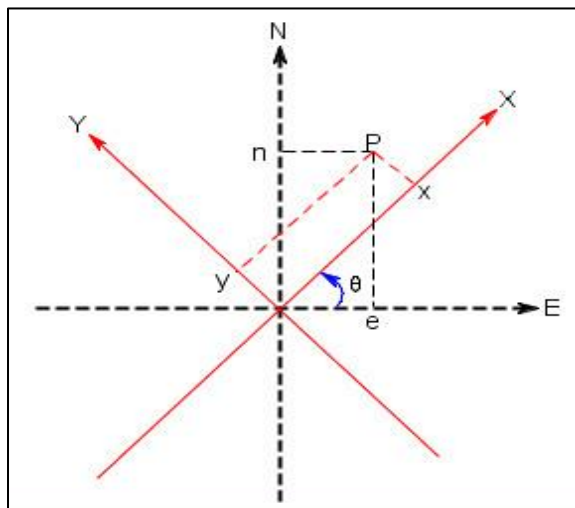


Fig. 4.16: Coordinate rotation. The diagram shows the rotation of the coordinate system from ENZ to XYZ.

➤ Data Cleaning

While collecting TLS data, points that are not representative of the true surface such as scattered points from the wind, dust, or birds can be recorded in the dataset. Some anomalous outlying points can be manually and carefully removed

from the dataset while processing the data using RiSCAN Pro. However, other more difficult-to-remove and isolated points have to be removed using additional tools. These outliers can sometimes be buried in the point cloud and were therefore missed by the automated terrain filtering process. Thus, their manual removal must be avoided, and other data cleaning processes must be performed.

For this purpose, the GMT command *grdfilter* was used. The *grdfilter* filter is performed in the space domain using either a convolution or a non-convolution filter. In this study, a non-convolution median filter was applied to the pre-processed TLS dataset. The filter uses “averaging” in order to remove anomalous and unwanted signals, and it sets a window which resulting value will be represented as the median of the neighboring points. The “window” for this study was set to be a square of 0.5 m by 0.5 m dimensions.

➤ Interpolating to DEM

Due to the uneven distribution in space of points, a regriding process of interpolation is necessary to generate a model where elevation is continuously available, and gaps are smoothed and filled. The *nearneighbor* interpolation GMT tool was used in order to smooth the dataset and to fill gaps. This tool uses the nearest-neighbor algorithm in order to calculate a value for a node. The algorithm considers points within a radius with its center at the defined node, and it

calculates an average value for the node based on the weighted mean of the points within the search radius. In our study area, the search radius was set to be 16 m.

➤ Anti-Aliasing Filtering

Following the necessity to regrid the dataset, the generation of DEMs also involves a downsampling process where spatial decimation is performed. However, the downsampling process leads to aliasing issues as it biases high-frequency signals; therefore, further filters must be applied on the dataset in order to remove spatial distortions. As recommended by Xiong et al., 2016, a Butterworth low-pass spatial filter was applied using the *grdfft* GMT command before performing downsampling. This filter was set with a cutoff wavelength three times the desired DEM's grid size. Therefore, to produce a 1 m by 1 m DEM of our study area, the cutoff wavelength was set to be 3 m in the X-direction and 3 m in the Y-direction. The GMT tool *grdfft* uses a 2D-forward Fast Fourier Transform, and it is used in order to perform filtering in the frequency domain, allowing users to apply anti-aliasing filtering.

➤ Downsampling

The further decimation of the data was done in order to reduce the size of the dataset and to manipulate the data in a timely manner without compromising the

quality of the results. The GMT *blockmedian* tool was used to assign a value to non-empty blocks in a grid file with arbitrarily located XYZ points. In this study, the downsampling took the DEM from an original 0.5 m by 0.5 m grid size to a 1 m by 1 m grid size.

The proposed workflow to process TLS data and generate DEM is shown in Fig. 4.17. It includes steps from the initial collection of the TLS and GPS datasets to the generation and visualization of the resulting DEMs. It includes the application of three software and short scripts. A total of four DEMs representing each collection cycle were generated in this study and analyzed using different ArcGIS tools explained later.

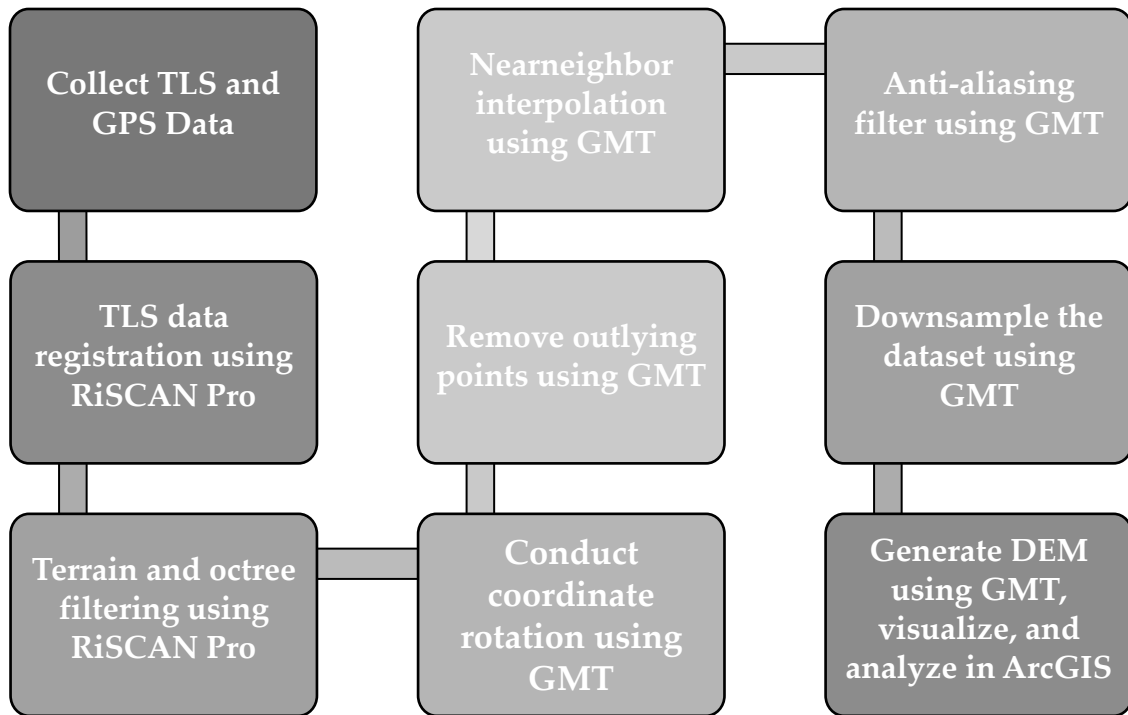


Fig. 4.17: Methodology to derive DEMs from TLS and GPS datasets. Each step of the methodology, from data collection and DEM generation, is included in the methodology.

After the collection of TLS and GPS data from May and December of 2015, and May and December of 2016, the processing of the corresponding datasets following the workflow was conducted. Four DEMs were obtained for the four TLS collection cycles, and they are seen in Figs. 4.18 through 4.21.

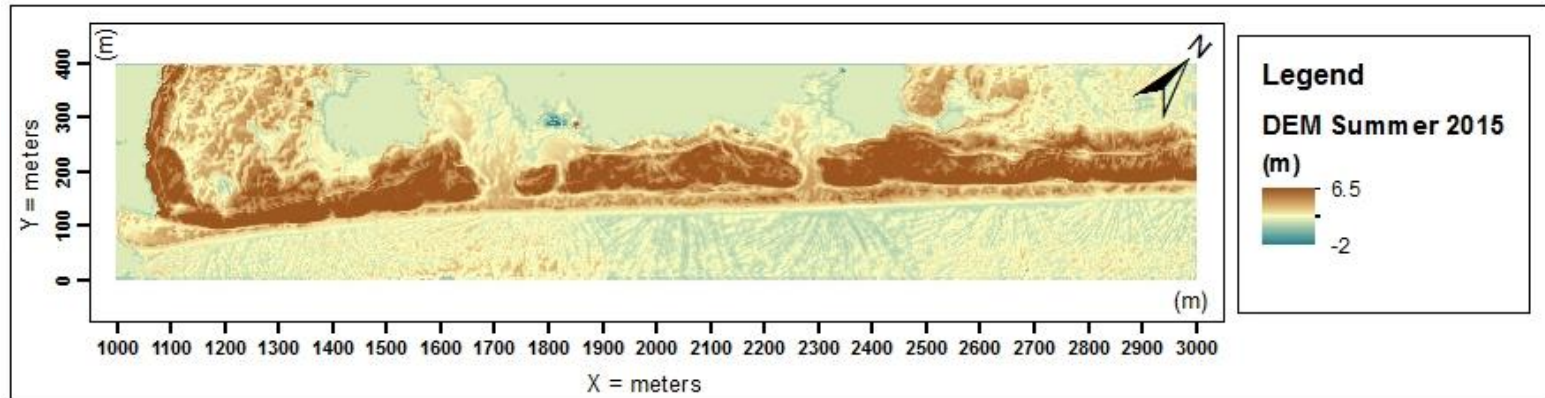


Fig. 4.18: DEM derived from 2015 Summer TLS Survey. The figure shows the Summer 2015 digital elevation model generated after performing the processing steps established in this study.

72

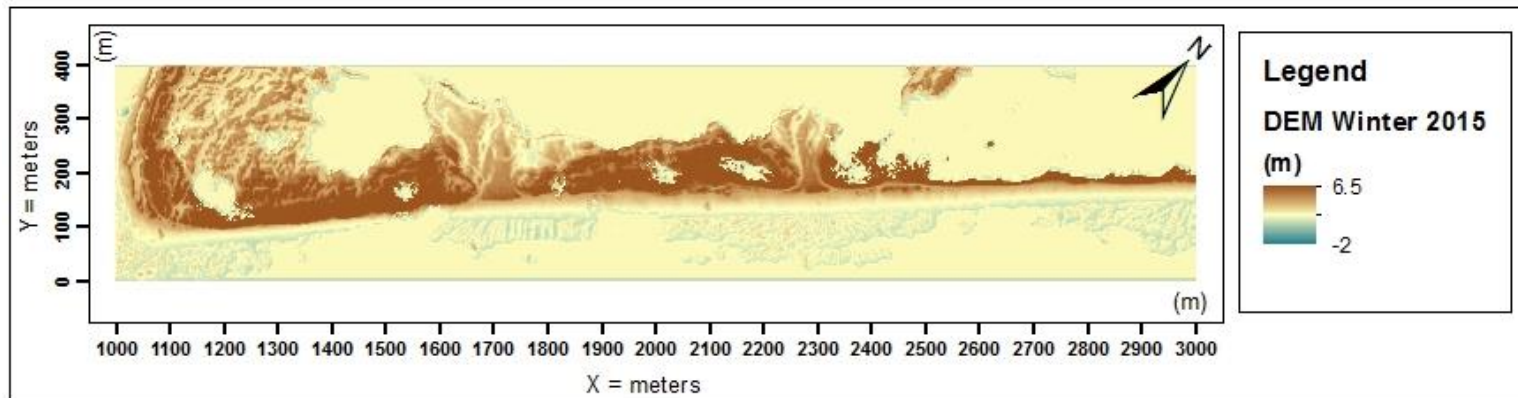


Fig. 4.19: DEM derived from 2015 Winter TLS Survey. The figure shows the Winter 2015 digital elevation model generated after performing the processing steps established in this study.

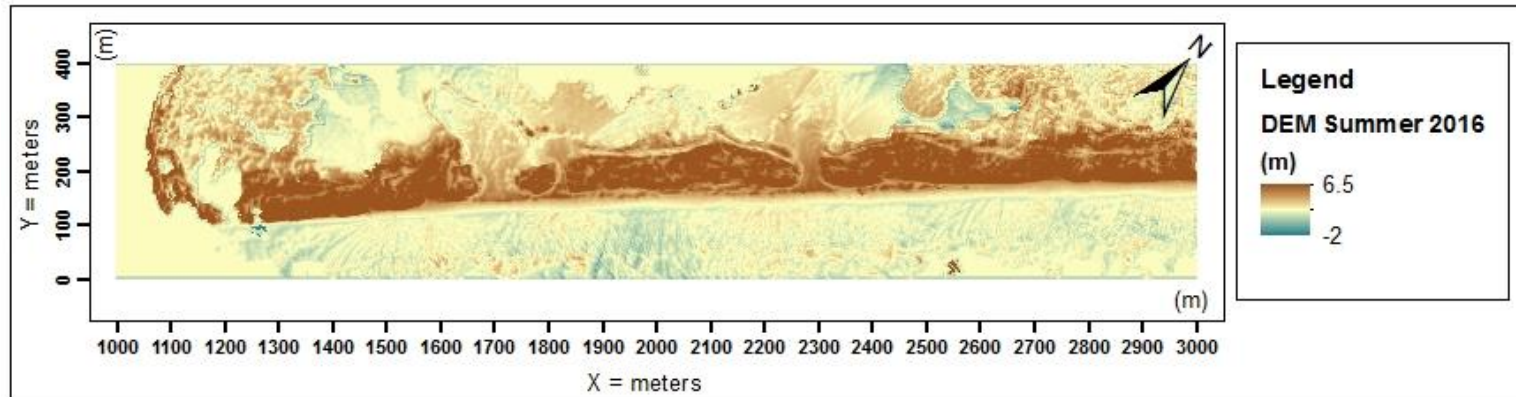


Fig. 4.20: DEM derived from 2016 Summer TLS Survey. The figure shows the Summer 2016 digital elevation model generated after performing the processing steps established in this study.

73

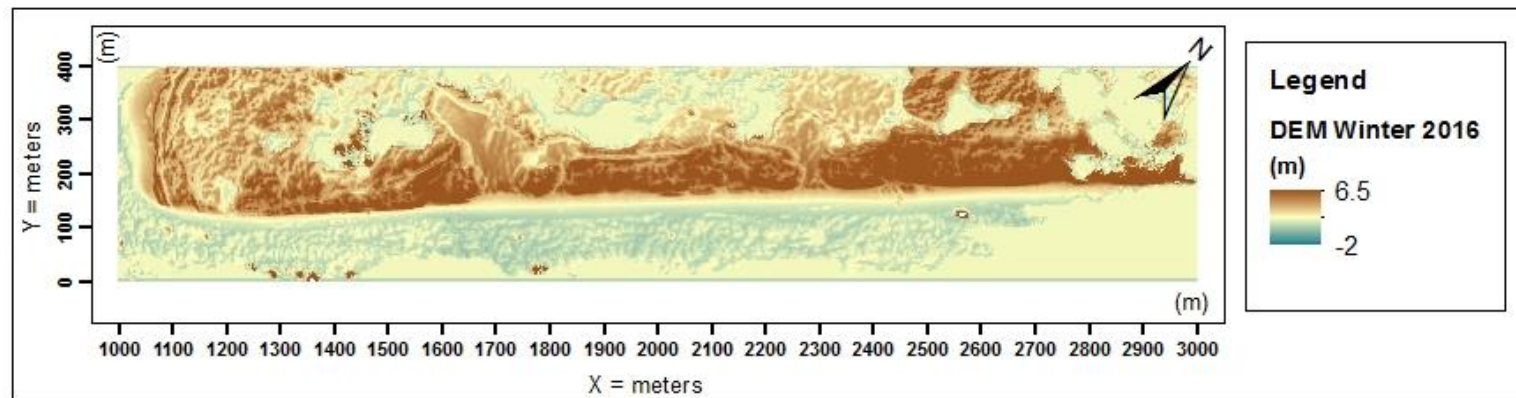


Fig. 4.21: DEM derived from 2016 Winter TLS Survey. The figure shows the Winter 2016 digital elevation model generated after performing the processing steps established in this study.

4.3.4 Point Cloud and DEM Accuracy Assessment

The accuracy and precision of the results and the quantification of morphological changes depend on the overall accuracy of the TLS surveys and the obtained DEMs. Accuracy is defined as the degree to which the measured value is close to its real value, and precision specifies the repeatability of the measurements. Accuracy describes systematic errors in the measurements, while precision describes random errors. The root-mean-squared error of the repeated measurements in a study is used to quantify its accuracy. In TLS studies, the accuracy of the GPS measurements from which positioning is derived defines the accuracy of the survey.

According to the scanner manufacturer, the accuracy of the instrument at 150 m range and under ideal conditions is 8 mm, while the accuracy of the GPS units used for the kinematic survey lies within centimeter level. However, accuracy in the field can be lower due to unfavorable conditions such as rain, wind, or poorly reflective surfaces. Moreover, the positional accuracy of TLS points with respect to the GLCS could be affected by the precision or accuracy of GPS measurements. While both the R10 GPS and the NetR9 unit quote a vertical precision in positioning performance of 15 mm, the true accuracy might be affected by other factors such as obstructions, satellite geometry, or atmospheric conditions among

other. Also, the accuracy of the RTK survey itself, which corresponds to a couple centimeters level, can be affected by external factors such as the nature of the survey, the terrain, and the instruments used to collect the GPS data.

Point cloud and DEM accuracy assessments were performed during the Winter 2016 collection cycle. The objective of the evaluation was to determine the accuracy of the raw LiDAR point clouds (after terrain filter) and the derived DEMs by comparing kinematic GPS elevation values to the point cloud and DEM elevation points. Descriptive statistical terms are used to assess the accuracy of LiDAR data. Measures of statistical variability are used to quantify the accuracy of repeated measurements. The standard deviation of a set of a set of points, in this case the set of values representing the difference between the LiDAR and the GPS points, is generally used to assess the accuracy of the TLS survey. The value usually ranges from 5 to 30 cm in LiDAR studies (NOAA Coastal Services Center, 2012).

The kinematic GPS surveys were performed on December 5th and 6th of 2016. Two sets of surveys were collected to also compare the assessment between a mostly flat beach surface and the dune surface. The cross-dune survey was performed on December 5th, and the flat-beach survey was performed on December 6th. Fig. 4.22 shows the GPS points selected for the assessment. The December 5th survey was in turn subdivided into four profiles A through D. The

elevation points from the kinematic surveys were compared to the DEM and the raw point cloud.

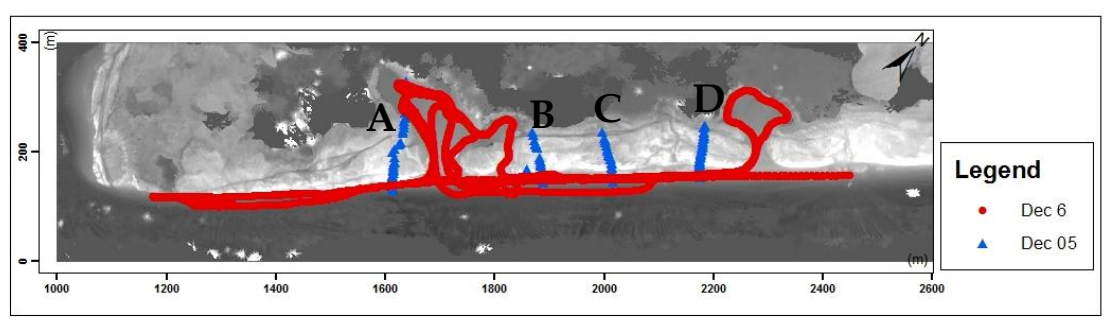


Fig. 4.22: GPS survey points. Scaled image of the GPS points labeled A through B collected in the study area on December 5th, and the selected GPS points for the December 6th survey. These surveys were used to perform the point cloud and DEM accuracy assessment of the study.

A total of 114 data points were collected in the December. 5th RTK survey, and over 2100 kinematic GPS points were collected in the December. 6th survey. The same amount of data points closest to the GPS points were extracted from the 1 m x 1 m DEMs and the LiDAR point cloud for comparison. The GPS elevation values for the four profiles of the December. 5th survey were plotted in Figs. 4.23 and 4.24, and in Fig. 4.25 for the December. 6th survey. The differences show a trend between the elevation points.

A summary of the statistical results obtained from the cross-dune GPS survey is shown in Table 4. Out of 114 points compared, there was one DEM point with a difference value higher than 1 m, and no raw data points with a difference value

higher than 1 m. The survey points with the highest elevation differences were mostly located where there is a sudden change in elevation or at the back dune area where the density of the TLS points diminishes and there are small areas with no laser coverage. Therefore, the points selected from the DEM were based on the interpolation rather than the original point cloud, while some of the extracted points from the point cloud dataset were located too far away from the GPS points.

Table 4. Accuracy assessment statistical results for the cross-dune GPS survey. The table shows the standard deviation and the mean of the elevation differences of the point cloud versus the DEM.

	Standard Deviation	Mean
Point Cloud	0.24 m	-0.20 m
Dem	0.25 m	0.37 m

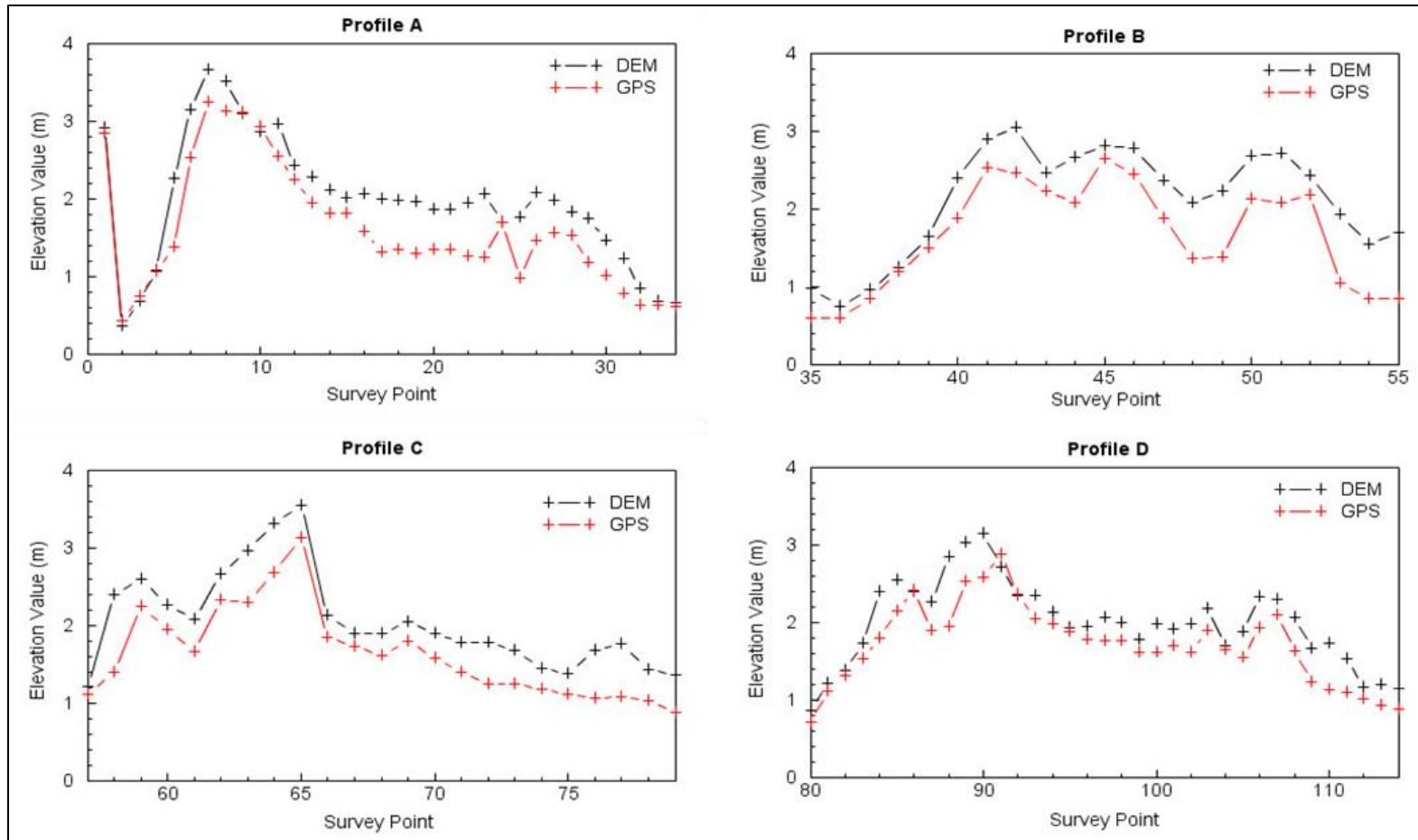


Fig. 4.23: DEM accuracy assessment results for the cross-dune area. The plots show the elevation value comparisons of the four profiles extracted from the RTK survey and the Winter 2016 DEM.

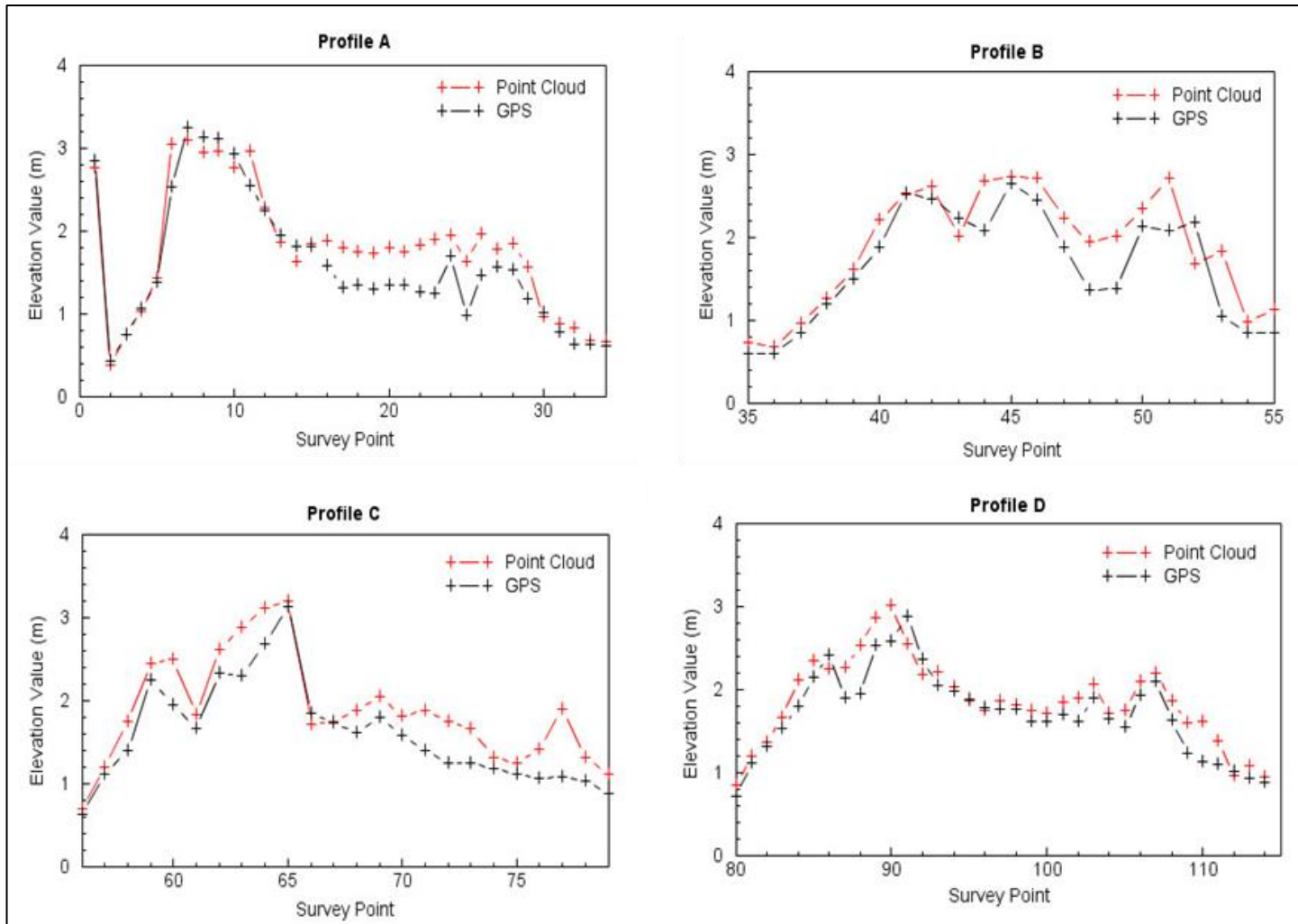


Fig. 4.24: Point cloud accuracy assessment results for the cross-dune area. Profiles A through D depict the accuracy assessment of the raw data points.

A summary of the statistical results of the flat-beach survey is seen in Table 5. Out of the 2100 points compared, there were no DEM-GPS or raw-GPS compared points with an elevation difference higher than 1 m.

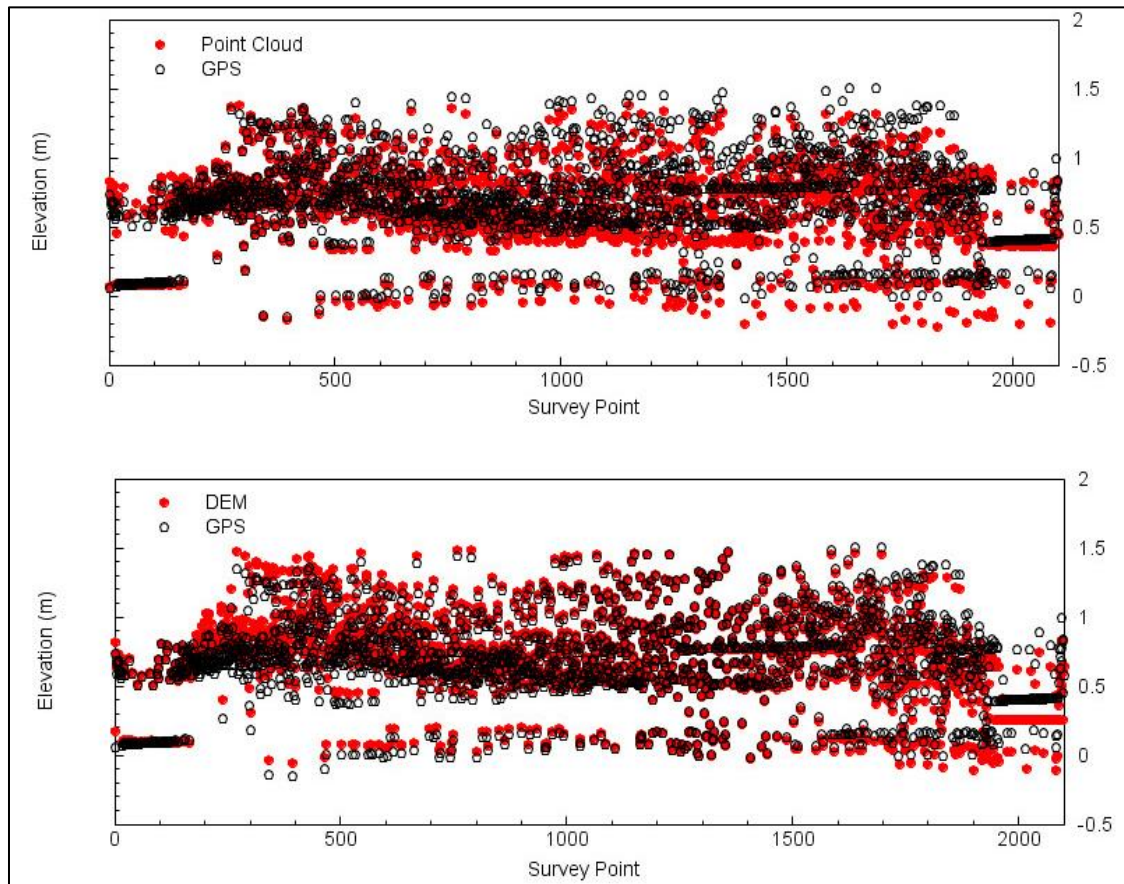


Fig. 4.25: Point cloud and DEM accuracy assessment results for the flat-beach area. The plots show the comparison of elevation values between the GPS survey and both the raw LiDAR datasets and the final DEM from December of 2016.

Table 5. Accuracy assessment statistical results for the flat-beach GPS survey. The table shows the standard deviation and the mean of the elevation differences of the point cloud versus the DEM

	Standard Deviation	Mean
Point Cloud	0.074 m	-0.058 m
Dem	0.076 m	0.005 m

Conclusions from the accuracy assessment include:

(1) In both cases (flat-beach versus cross-dune GPS surveys), the accuracy proves to be better in the raw datasets. This occurs because generating DEMs implies interpolation of the datasets into continuously available elevation values. When doing so, the points that were extracted to be considered in the assessment might have not coincided with the GPS points.

(2) The flat-beach assessment also showed improved results compared to the cross-dune accuracy evaluation mainly due to the nature of the rough terrain in the dune area and the laser scanner coverage. While performing the RTK GPS survey across the dunes, the pole used to transport the GPS unit was sometimes tilted and sunk in the dry sand. Moreover, the cross-dune area exhibit some poor-coverage regions where there are no cloud point. In those areas, the assessment relied on cloud points that did not coincide or that were too far away from the RTK survey points. Therefore, higher difference values were expected for these areas.

Chapter 5 Morphological Changes Derived from DEMs

Coastal monitoring studies and change analysis rely on the extraction of coastal features, the quantification of their movement in time, and the quantification of volumetric change throughout time. In this study, the features that were extracted are the shoreline, the vegetation line, and the dune ridge (Fig. 5.1). These features are important to quantify net accretion or erosion, to measure dune migration, and to predict coastal vulnerability (Hardin et al., 2014). The features extracted have differing definitions depending on the nature and location of the study, and therefore require further explication.

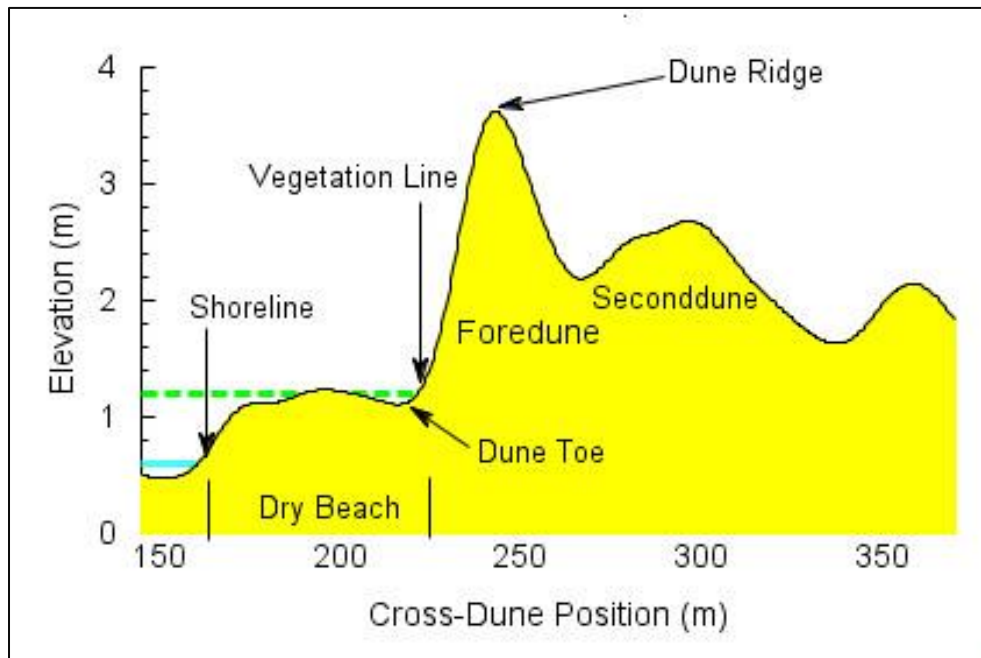


Fig. 5.1: Coastal features extracted from the study area. A diagram that shows a cross-beach profile example of the features extracted in this study including the shoreline, vegetation line, and dune ridge.

The extracted flat- beach features in the study area (shorelines and vegetation lines) were assumed to possess an uncertainty related to the accuracy of the DEMs obtained in this study. The uncertainty of the DEMs on the flat-beach area was of 7 cm, and it was considered in the shoreline and vegetation line extraction procedures. The average change in the positioning of the shorelines and the vegetation lines when taken into consideration the DEM uncertainty was ± 3 m. Therefore, the net movement and rates-of-change values calculated had an uncertainty of ± 3 m.

5.1 Shoreline Analysis

Shorelines are directly affected hierarchically by natural factors that include (from the one with more effect on the shorelines to the one with less effect) tides, storms, sediment supply, and relative sea level (Morton and Pieper, 1975). The importance of shoreline analysis lies on the fact that shoreline erosion, which is the overall trend of the Texas coast, means the loss of land and damage to coastal structures.

The shoreline is defined as the line between wetland and dry land. The shoreline can be approximated by a constant elevation contour in a tidal datum (Hardin et al., 2014). Previous studies have indicated that the wet and dry

boundary in the Texas coast typically occurs 0.6 m above local mean sea level (Gibeaut et al., 2009; Paine et al., 2013); therefore, contour maps of the datasets were generated with a 0.6 m contour interval with the seaward-most contour interval representing the defined approximated shoreline.

After the TLS datasets were processed, ArcGIS was used to visualize and analyze the results in the form of DEMs. ArcGIS is the geographic information system's set of software products by the Environmental Systems Research Institute (ESRI) which focuses on the analysis, editing, design, and management of geographic information. Several tools can be added to ArcGIS to extend the capabilities and usefulness of the product. The Digital Shoreline Analysis System (DSAS) is an open-source ArcGIS extension tool by the USGS that computes rate-of-change statistics from shorelines' time series. The shoreline net movement and change statistics of this study were analyzed using DSAS. The tool has been used extensively in multiple coastal morphology studies (Mahapatra et al., 2014; Mujabar and Chandrasekar 2011; Kuleli, 2009; Paine et al., 2013), and the advantages of the software includes the ease to perform statistical computation and its minimal requirements.

DSAS uses the user's shorelines input, and a user-delineated baseline in order to construct transects perpendicular to the baseline, and to calculate net movement

and rate-of-change statistics. These calculations are made after the tool computes the intersect points between the transects and each shoreline it traces, and they are based on the dates corresponding to each shoreline and the distances between them. In this study, the baseline was constructed offshore parallel to the trend of the four shorelines considered. After digitizing every shoreline for each collection cycle of the study (Fig. 5.2), the transects were cast perpendicular to the baseline with a 50 m spacing, and 300 m of length (Fig. 5.3 and Fig. 5.4).

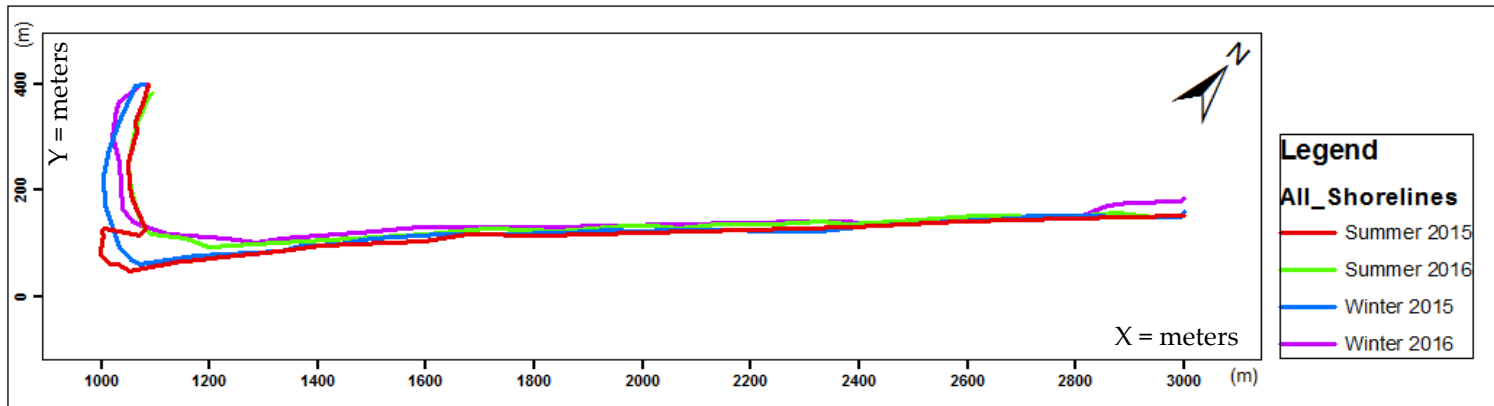


Fig. 5.2: Extracted shorelines of the study area. After extracting the contours for each dataset, the shorelines were approximated and extracted.

98

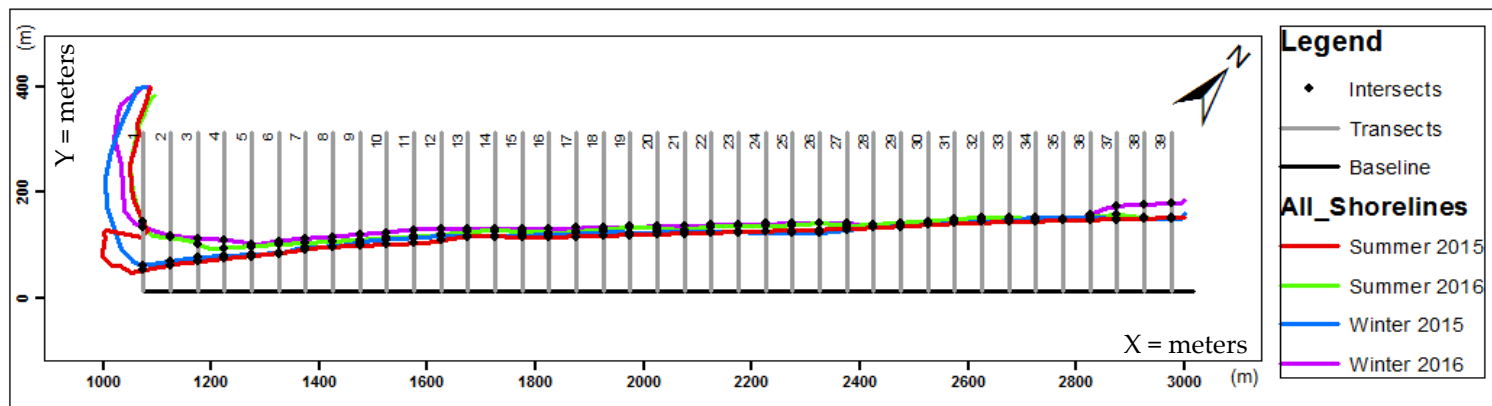


Fig. 5.3: Shorelines, baseline, transects, and intersects. The figure shows the extracted shorelines, the constructed baseline, the transects built perpendicular to the baseline, and the intersects of the transects with the shorelines.

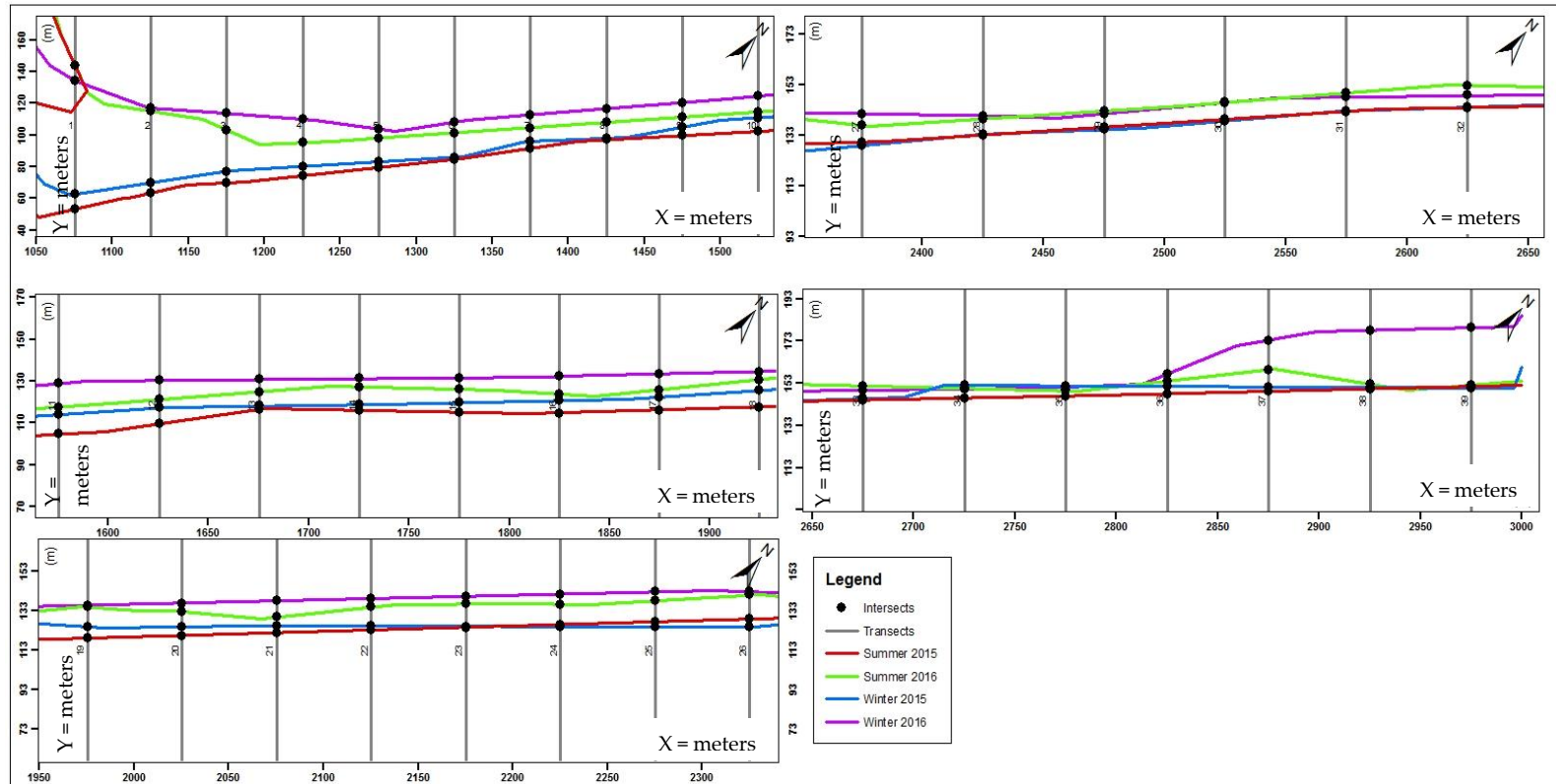


Fig. 5.4: Shoreline, transects, and intersects. The zoomed-in figure shows the approximated shorelines for all the four collection cycles, the transects, and the intersect points.

In order to report linear changes, DSAS offers the user calculations that provide net movement and rate-of-change statistics of the input shorelines. They include shoreline change envelope (SCE), the net shoreline movement (NSM), and the end point rate (EPR), all of which were calculated in this study.

The shoreline change envelope represents a distance measurement between the farthest and closest shorelines to the baseline at each transect (Fig. 5.5). This calculation takes into consideration all available shoreline positions, and it does not regard the shorelines temporal identification.

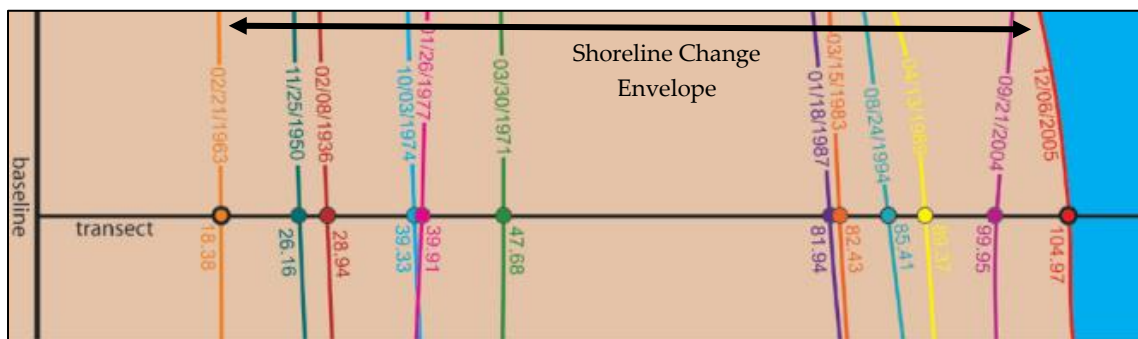


Fig. 5.5: Shoreline change envelope. The diagram shows the distance measured from the closest to the farthest shoreline to the baseline representing the shoreline change envelope (modified from Himmelstoss, 2009).

Another movement report is the net shoreline movement which represents the distance between the oldest and the youngest shoreline at each transect (Fig. 5.6). When this distance is divided by the number of years passed between the two shoreline positions, the result is the end point rate (Fig 5.7). The sign of the shoreline movement depends on the location of each shoreline with respect to the

baseline, and the relative position of the shorelines with respect to one another.

Both the NSM and the EPR are associated with two shorelines and their dates.

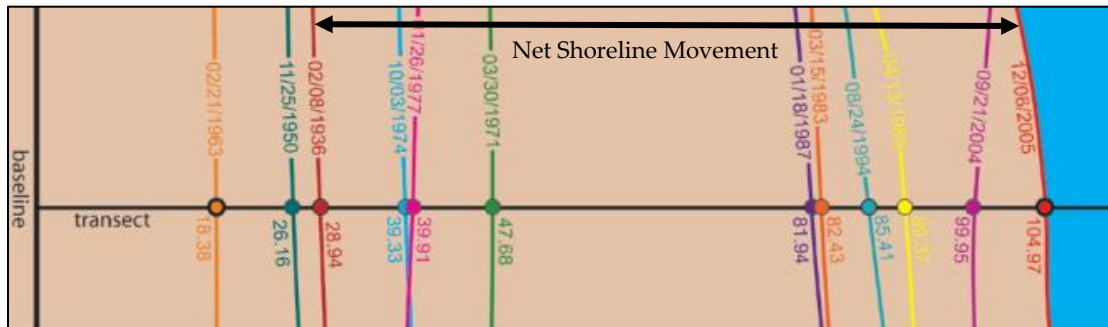


Fig. 5.6: Net shoreline movement. The net shoreline movement represents a distance between the oldest and the youngest shorelines (modified from Himmelstoss, 2009).

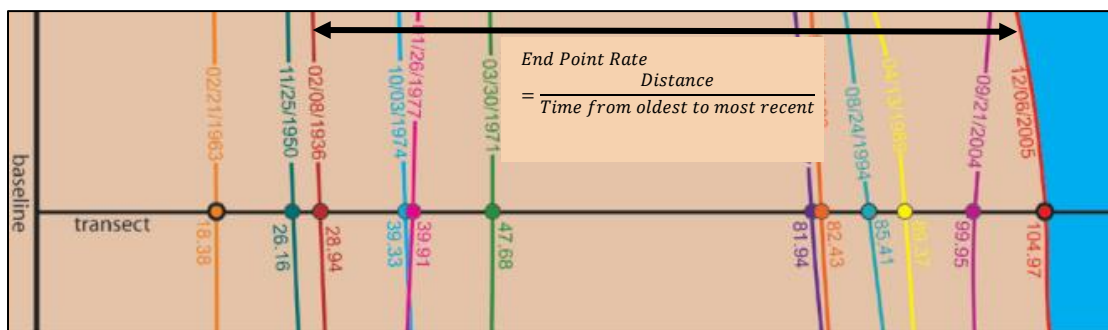


Fig. 5.7: Shoreline's end point rate. The end point rate represents the net shoreline movement (distance between the youngest and oldest shoreline) divided by the time elapsed between those two shorelines (modified from Himmelstoss, 2009).

The shorelines were approximated to be at the 0.6 m contour line, extracted, and digitized in ArcGIS. The DSAS ArcGIS extension tool was applied in order to digitize the shorelines and to produce transects in order to derive shoreline displacement calculations for the study's time period. After the extraction of the approximated shorelines for the four collection cycles, DSAS provided the

following movement and rate-of-change calculations at each transect. It is worth noting that the transects are identified and numbered from transect #1 near the mouth of the delta to transect #39 at the northeastern end of the study area.

The shoreline change envelope (Fig. 5.8), which is a distance and not a rate, showed higher values at both ends of the shorelines. The highest values are seen specifically in the delta area where a distance of 91 m was calculated between the closest and the farthest shorelines to the baseline. The lowest distance calculated was for transect #35 with 5 m of shoreline distance. The average shoreline distance between the closest and farthest shorelines to the baseline was 20 m. However, since the first four transects (#1 to #4) cover the highly dynamic delta environment with extreme shoreline movement values, they were ignored in the final average calculations. When omitting those transects, the average shoreline change envelope is 16 m.

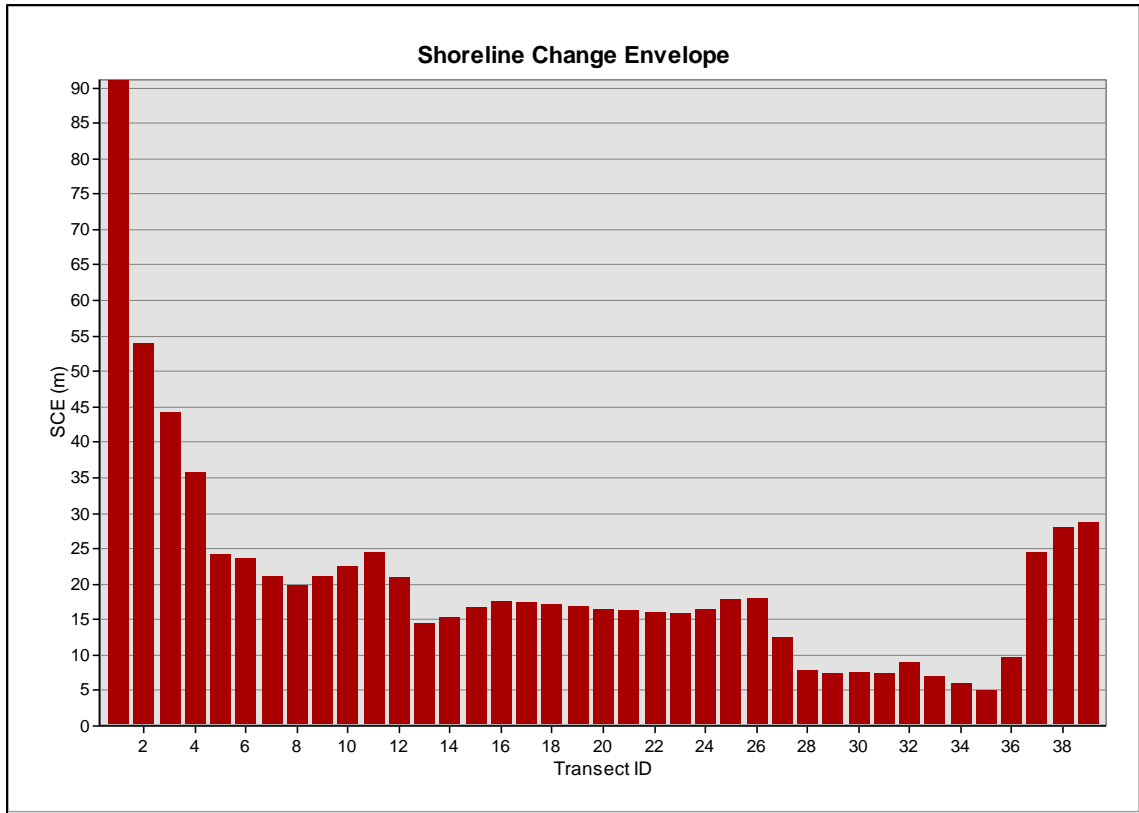


Fig. 5.8: Shoreline change envelope. Change envelope representing the distance between the closest and the farthest shorelines to the baseline.

The net shoreline movement was then calculated, and it reported a distance between the oldest and youngest shorelines; therefore, it is not considered a rate either (Fig. 5.9). Similar to the shoreline change envelope trend, the most extreme values are seen at both ends of the shorelines. Since both shorelines considered for this calculation lie on one side of the baseline, and since the oldest shoreline is the closest to the baseline at each transect, the net shoreline movement is negative at each transect. Therefore, negative values correspond to shoreline retreat and erosion. The lowest value was -81 m at transect #1, while the largest value was -4

m at transect #34. The average net shoreline movement was -20 m. As mentioned before, since the first four transects were considered highly dynamic and not truly representative of the rest of the study area, the average net shoreline movement after ignoring them is -16 m.

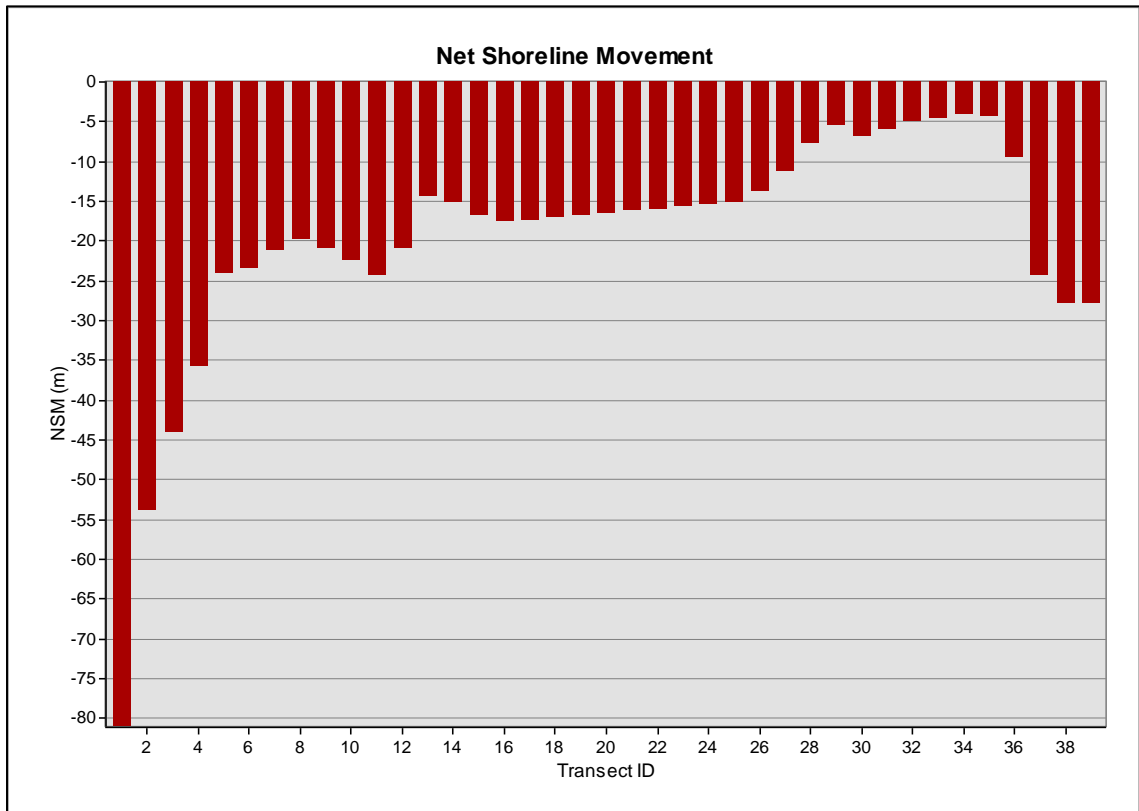


Fig. 5.9: Net shoreline movement. The figure shows the net shoreline movement, or the distance from the oldest to the youngest shoreline in the study area.

The end point rate (EPR) calculation followed after dividing the net shoreline movement at each transect by the time elapsed between them (Fig. 5.10). Since the net shoreline movement values were all negative, the EPR is also negative at each transect. Following the coastal trend, the rates-of-change are extreme at both ends

of the shorelines studied. The largest rate calculated was at transect #1 with a rate of 51 m of beach loss per year, while the lowest rate of change was calculated at transect #34 with a rate of 3 m of beach loss per year. The average rate-of-change was 12 m of beach loss. It is worth noting that there was no transect with positive values, so no portion of the shorelines considered in the study accreted in the study period. Again, when ignoring the first four transects located at the delta, the average shoreline rate of erosion is 10 m per year.

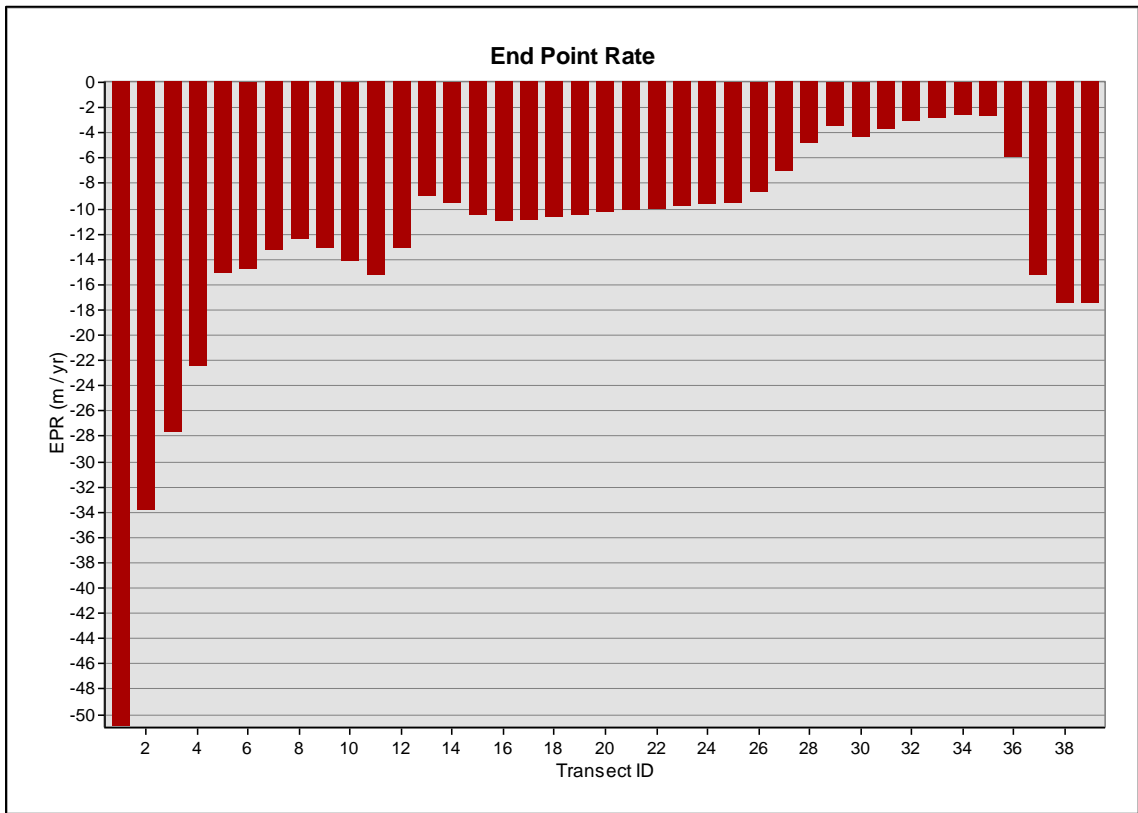


Fig. 5.10: Shoreline end point rate. The figure shows the yearly rate of shoreline change at each transect in the study area.

Since the shoreline corresponds to one of the most representative feature in coastal morphological studies, further calculations were performed. The movement calculations were completed for the periods from Summer 2015 to Summer 2016 (Fig 5.11) and from Winter 2015 to Winter 2016 (Fig 5.12). The net shoreline movement from Summer 2015 to Summer 2016 was calculated to be -8 m of shoreline retreat, while the net shoreline movement from Winter 2015 to Winter 2016 was -12 m. From these values, the yearly average rate of net shoreline movement is -12 m. Similar to previous calculations, the Summer 2015-Summer 2016 graph shows that the shorelines exhibited retreat at each transect. In contrast, from the Winter 2015 to the Winter 2016 graph we can see that there are several transects in which shoreline accreted.

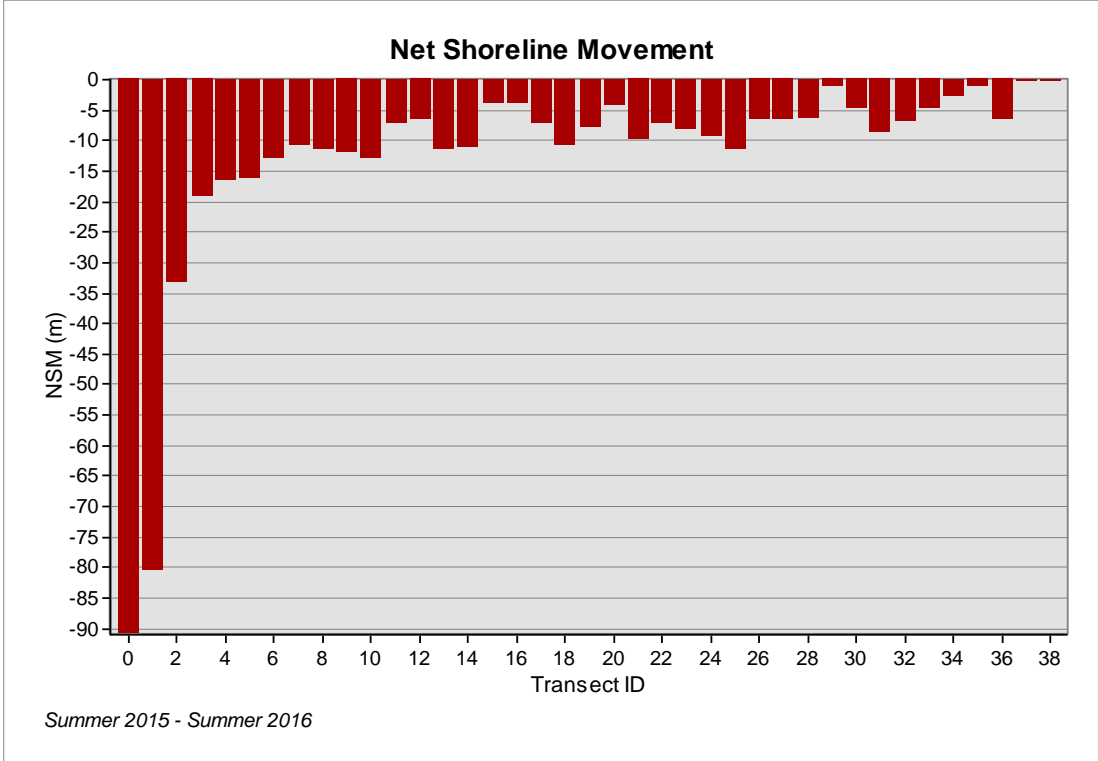


Fig. 5.11: Net shoreline movement from summer 2015 to summer 2016. The figure shows the net movement between the summer 2015 shoreline and the summer 2016 shoreline.

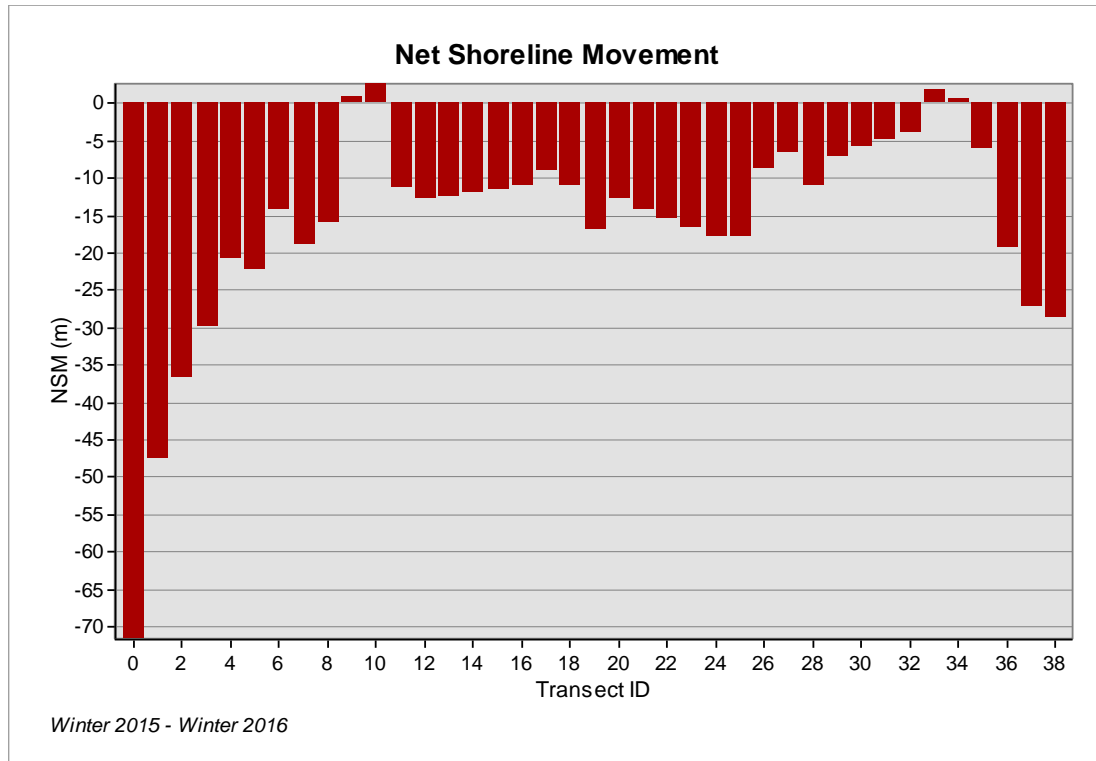


Fig. 5.12: Net shoreline movement from winter 2015 to winter 2016. The figure shows the net shoreline movement between the winter 2015 and the winter 2016 shorelines.

The net shoreline movement was also calculated from Summer 2015 to Winter 2015 (Fig. 5.13), and from Summer 2016 to Winter 2016 (Fig. 5.14). The average net shoreline movement for the Summer 2015 to the Winter 2015 period was calculated to be -2 m, while the net movement for the Summer 2016 to the Winter 2016 was calculated to be -5 m. The calculations for both time periods exhibit areas of significant shoreline advance, although the overall average corresponded to shoreline retreat.

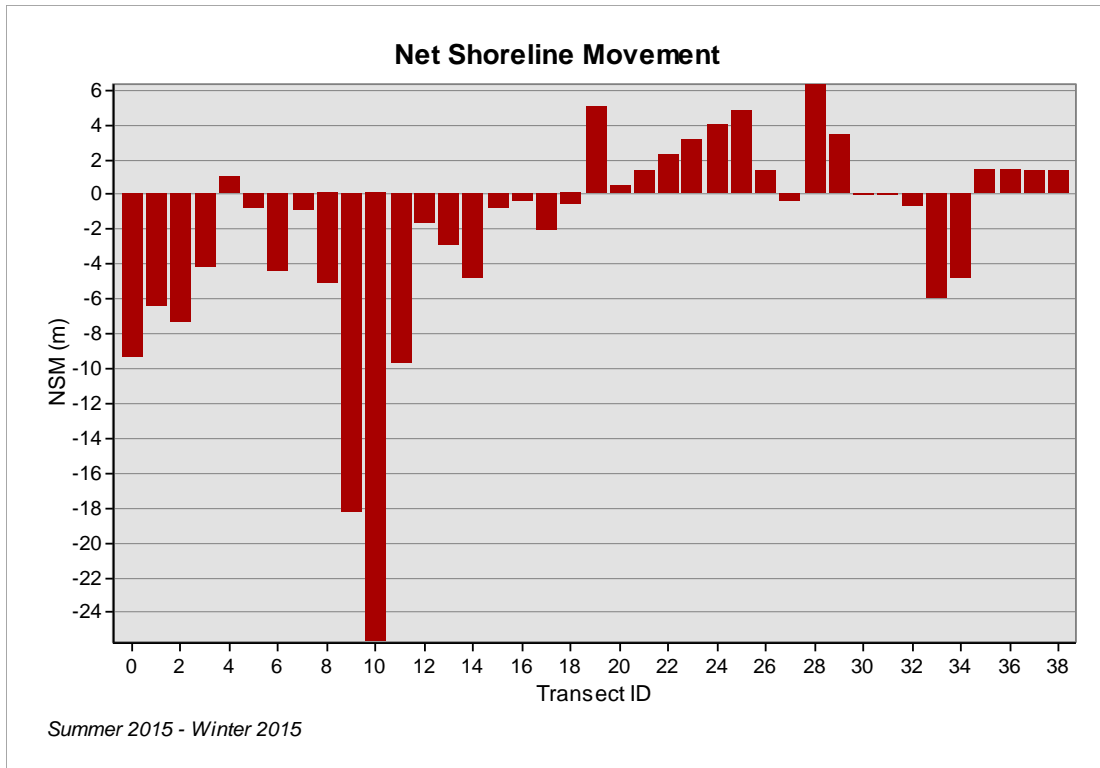


Fig. 5.13: Net shoreline movement from summer 2015 to winter 2015. The figure shows the distance between the summer 2015 and the winter 2015 shorelines.

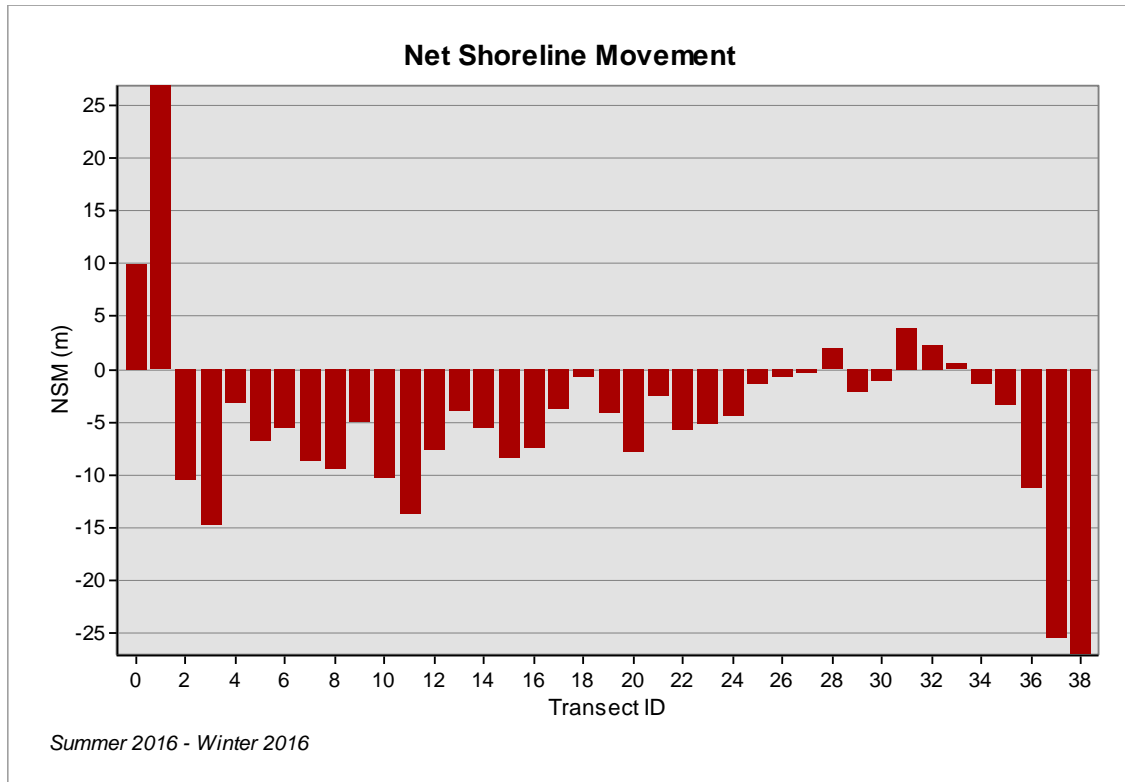


Fig. 5.14: Net shoreline movement from the summer of 2016 to the winter of 2016. The figure shows the distance between the summer of 2016 and the winter of 2016 shorelines.

A summary of the average net shoreline movement results at each transect is seen in Table 6. As mentioned before, the average movement values have an uncertainty of ± 3 m. The total net shoreline movement for this study from the Summer 2015 to the Winter 2016 study period was -16 m. Moreover, the yearly movement was compared to the seasonal movement of the shorelines. The shoreline experienced average yearly movement values that almost tripled the average of the seasonal changes. At the same time, the 2016 average seasonal movement doubled when compared to the average seasonal movement in 2015.

The total and yearly movements yielded higher results than those presented in previous studies. However, when considering the DEMs accuracy and the shorelines' uncertainty, the yearly summer-to-summer net shoreline movement is fairly comparable to the shoreline rate-of-change calculated in previous studies.

Table 6. Summary of the net shoreline movement results. The table shows the net shoreline movement values for each time period analyzed. Negative values correspond to shoreline retreat.

Period	Net Shoreline Movement
Total Movement	
Summer 2015 – Winter 2016	-16 m ± 3 m
Yearly Movement	
Summer 2015 – Summer 2016	-8 m ± 3 m
Winter 2015 – Winter 2016	-12 m ± 3 m
Seasonal Movement	
Summer 2015 – Winter 2015	-2 m ± 3 m
Summer 2016 – Winter 2016	-5 m ± 3 m

5.2 Vegetation Line Analysis

The vegetation line is generally defined as the seaward boundary of permanent vegetation, and the state of Texas defines it as the boundary between public beach and private property. Net changes in vegetation line have been related mainly to

storms on the Texas coast, and they reflect short-term conditions rather than long-term factors that affect the coast (Morton and Pieper, 1975). The study of vegetation line and shorelines might be perceived as overlapping, however, in some cases, their recovery period after storms might differ. As mentioned earlier in this study, while the shoreline recovers to its pre-storm location, the vegetation line might be buried under the recovered sand before it grows back through the sands.

Previous studies have indicated that the lowest elevation that the vegetated foredune can occur on the Texas coast is at 1.2 m above mean sea level (Gibeaut and Caudle, 2009; Paine et al., 2013); therefore, contour maps of the datasets were generated with a 1.2 m contour intervals in which the seaward-most line represents an approximation of the vegetation line.

Since the DSAS ArcGIS software tool is designed for studies that include rates-of-change for any boundary-type subject that incorporates a defined feature position, it can be used for vegetation line statistics as well. The same procedure used in DSAS to generate a baseline, transects and intersects for the shoreline analysis was followed for the vegetation line change analysis. However, the approximated vegetation line was extracted and approximated to be at the 1.2 m contour line. Figs. 5.15, 5.16, and 5.17 show the approximated vegetation lines for

each collection cycle, the digitized baseline and transects, and a zoomed-in view for better appreciation, respectively. Furthermore, the same movement calculations computed for the shorelines were calculated for the vegetation lines.

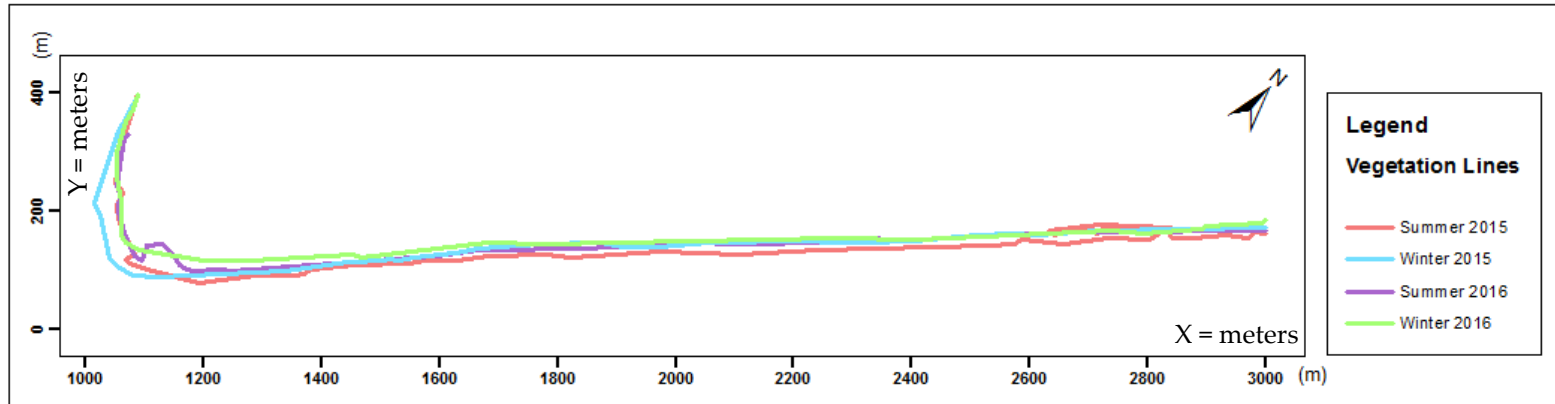


Fig. 5.15: Approximated vegetation lines of all collection cycles. The figure shows the vegetation lines from Summer 2015, and 2016, and Winter 2015 and 2016 of the study area.

102

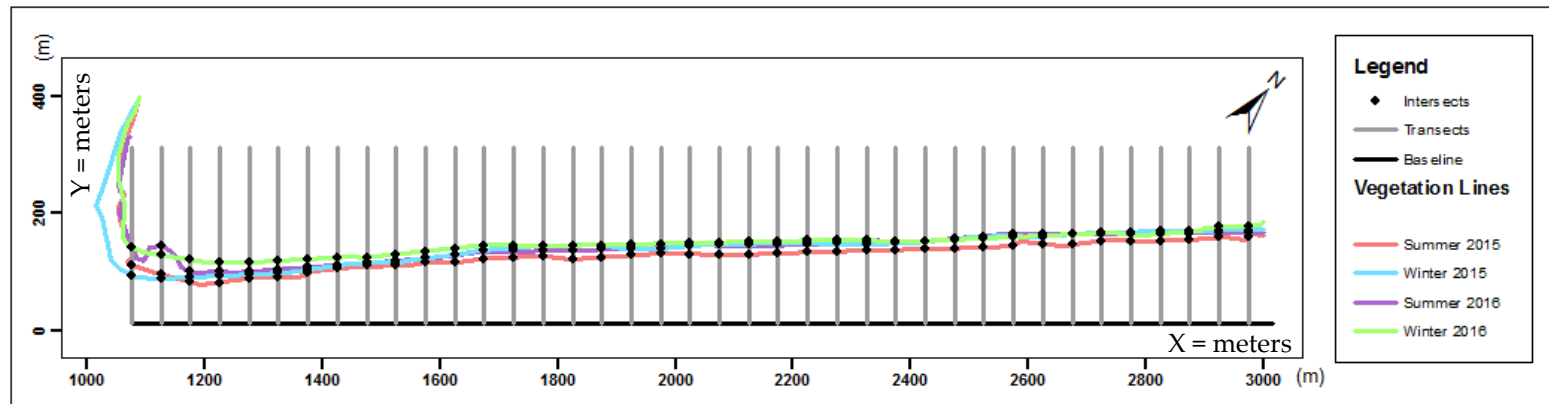


Fig. 5.16: Vegetation line, baseline, transects, and intercepts. The figure shows the approximated vegetation lines, the baseline constructed in ArcGIS, and the transects, and intercepts derived from DSAS.

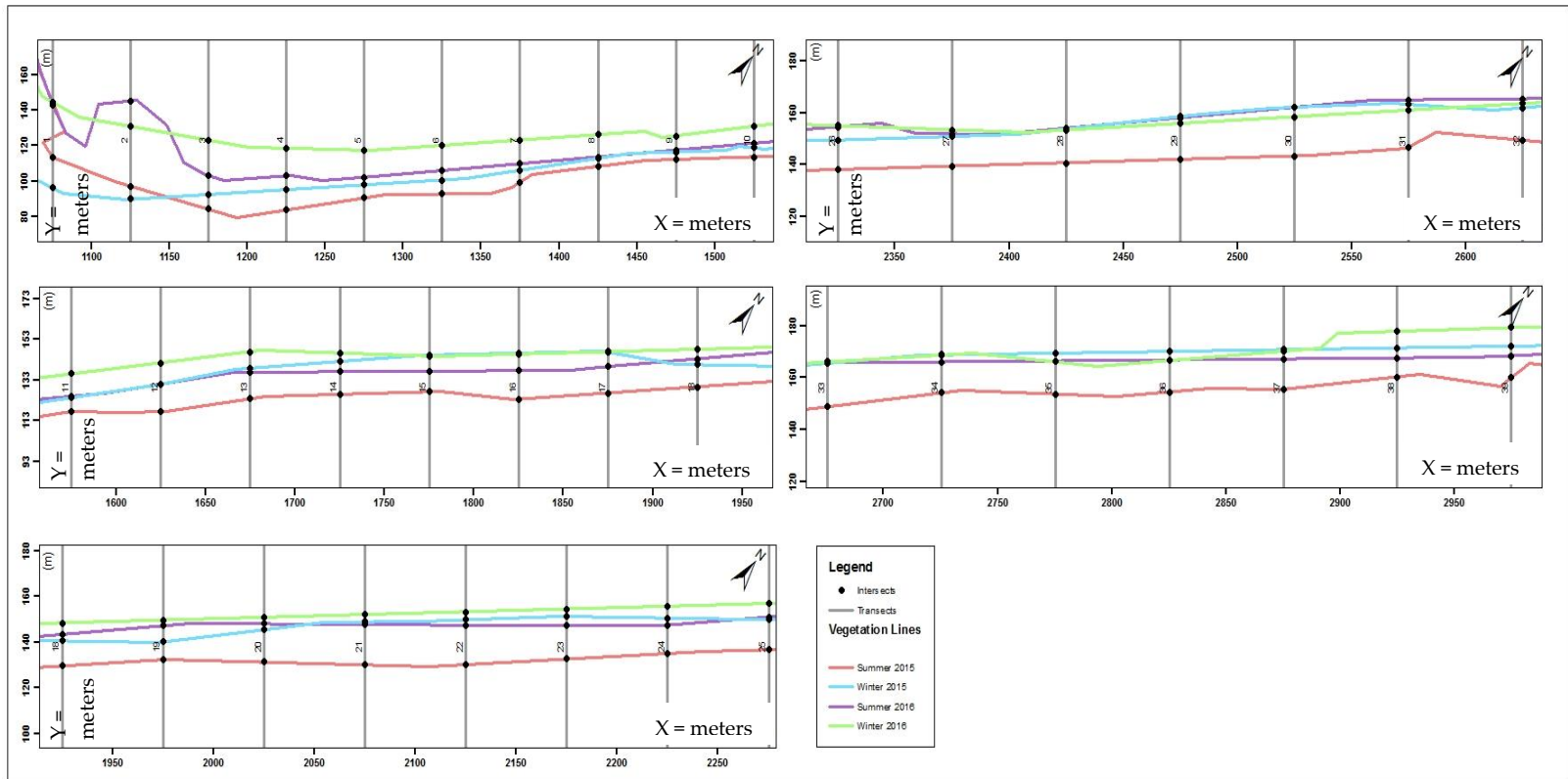


Fig. 5.17: Approximated vegetation lines, transects, and intersects. The zoomed-in figure shows the approximated vegetation lines for all the four collection cycles, the transects, and the intersect points between the transects and the vegetation lines. The approximated vegetation lines were split into four plots of approximately 600 m long.

Following the same workflow as for the shoreline extraction, the vegetation lines for each collection cycle was extracted at the 1.2 m contour interval where the seaward-most interval was considered to be the approximated vegetation line. The same calculations were also performed, and they are shown in Figs. 5.18 through 5.20.

Similar to the shorelines trend, the change envelope for the vegetation line shows maximum change near the delta area (Fig. 5.18). The highest distance between the farthest and the closest vegetation lines to the baseline in the study area was calculated at transect #2 with 55.5 m of vegetation line movement. The lowest value of vegetation line change envelope was calculated at transect #28 with 13.4 m of displacement. A fluctuating trend of vegetation line change is seen at the rest of the transects. The average of the change envelope values is 21.64 m. Following the shoreline trend, the first four transects were chosen to be ignored for averaging calculations. When doing so, the average approximated vegetation line change envelope is 19.5 m.

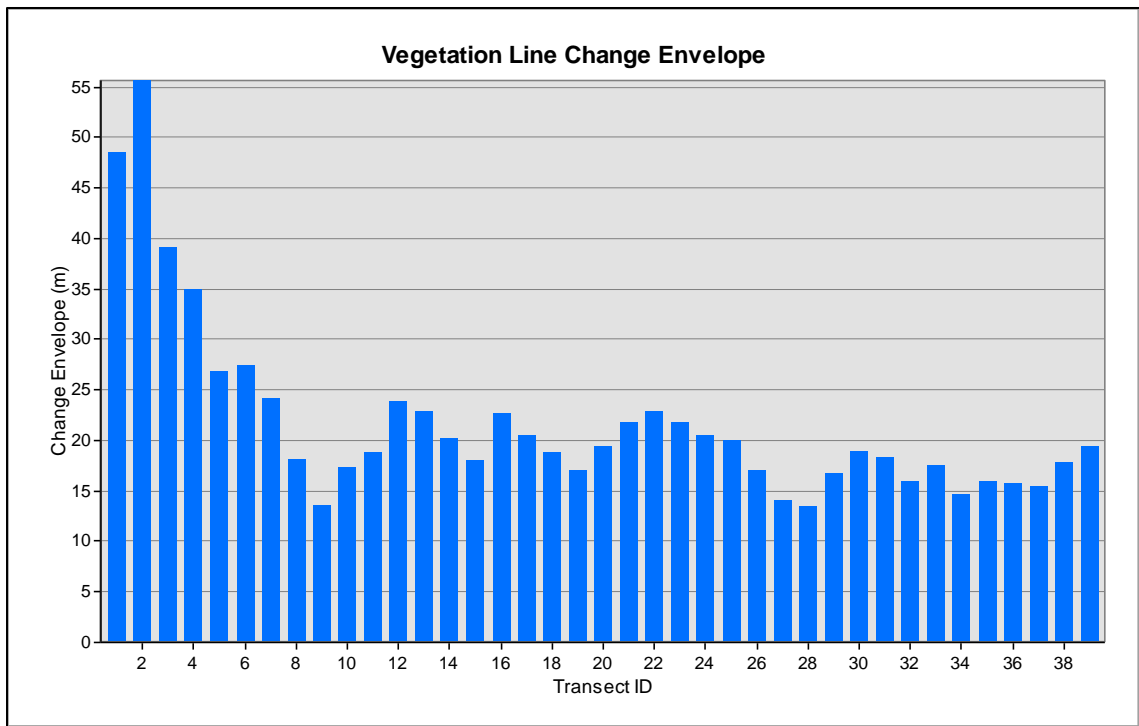


Fig. 5.18: Approximated vegetation line change envelope. The distance at each transect between the closest and the farthest vegetation line to the baseline is depicted in the figure.

The vegetation line net movement calculations brought up negative values due to the positioning of the vegetation lines with respect to the baseline, and their relative position (Fig. 5.19). The lowest values were calculated at both ends of the vegetation lines. The lowest value was -39 m at transect #3, while the highest value was calculated at transect #36 with -12 m of vegetation line movement. As well as for shoreline net movement, all of the transects were calculated to have negative vegetation line movement, which implies the retreat of the vegetation line in the study period. When ignoring the first four transects, the average net vegetation line movement is -19 m.

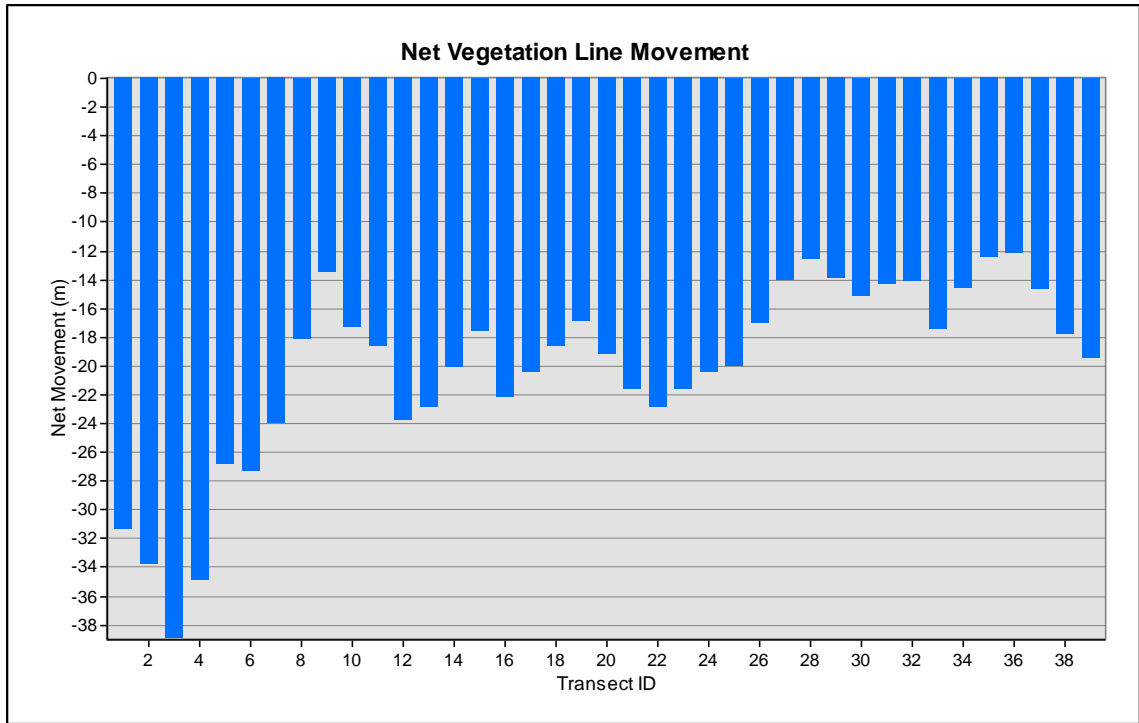


Fig. 5.19: Net vegetation line movement. The figure shows the distance between the youngest and the oldest vegetation lines at each transect in the study area.

The end point rate for all of the vegetation lines was also calculated (Fig. 5.20). The highest rate value was calculated at transect #3 with an EPR of 25 m of beach loss per year, which implies the fastest rate in the area. The lowest rate was calculated at transect #36 with an EPR of 8 m of beach loss per year. The average EPR was calculated to be 13 m for the study area. After ignoring the first four transects, the average end point rate of change for the vegetation line is 12 m of erosion per year.

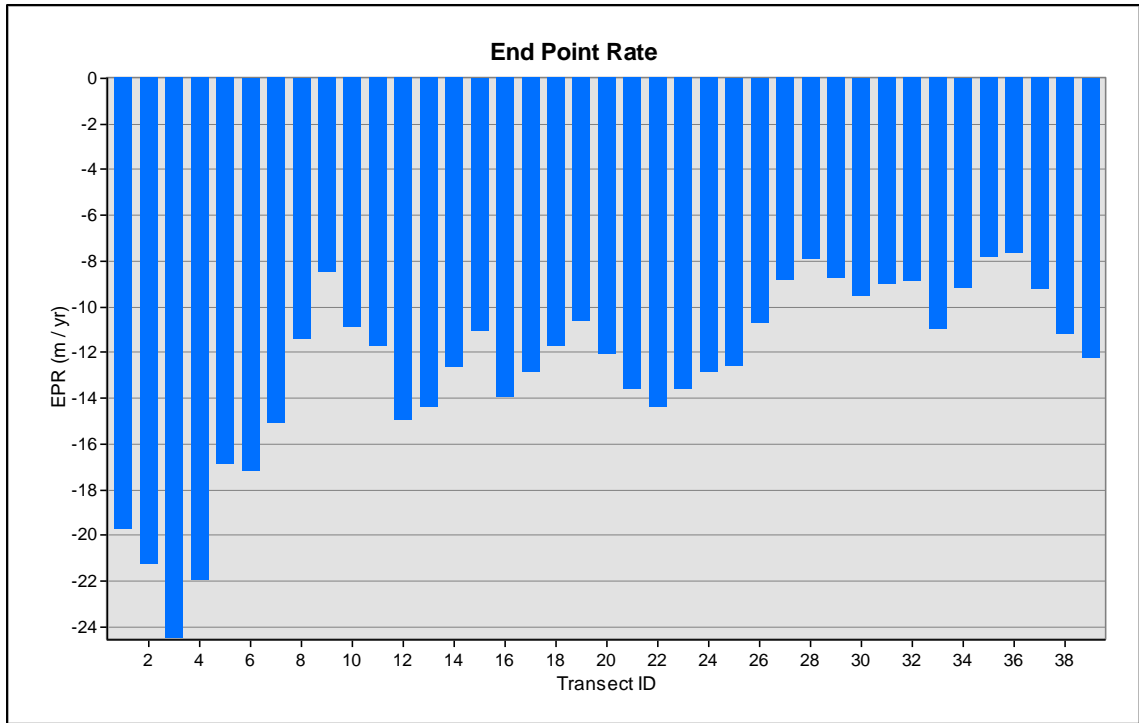


Fig. 5.20: Approximated vegetation line's end point rate. The figure shows the yearly rate of vegetation line movement at each transect in the study area.

5.3 Dune Ridge Analysis

As an acting protection structure to the back beach during storms, the dune ridge is an important dune and beach parameter to consider when studying beach morphology and coastal vulnerability. As storms hit the coastal area, the dunes protect the beach system from the storm surge and waves. Moreover, dunes act as sand reservoirs in the beach sediment's budget whenever the wind direction is sea-ward (Stanica and Ungureanu, 2010). The dune height (dune ridge) can be extracted from topographic data, and has been previously obtained from cross-

shore transects perpendicular to a baseline. However, an automated extraction method proposed by Hardin et al., 2014, and modified for ArcGIS was used in this study to extract dune ridges of the four collected datasets.

The method is based on the least-cost path tracing which can be easily applied in ArcGIS, and which aims to find the least-cost path between two geographic points. It only requires two inputs from the user: the DEM from which the parameter is going to be extracted, and two random points on each side of the dune ridge. Moreover, it is based on the quantitative definition of the dune ridge in the form of a cost function. Since the dune ridge corresponds to the maximum elevation in the dune area, the cost function is an inverse function of the DEM's elevation values. The premise to define cost through each grid cell is that the cost of a shorter, lower elevation path is greater than the longer, higher elevation path; therefore, the path below the dune ridge have a higher cost.

The cost function proposed by Hardin et al., 2014, and used in this study is as follow:

$$J_{ij} = e^{-\alpha z_{ij}}$$

where J_{ij} is the cost of each cell (i, j) , α is a tunable parameter, and z_{ij} is the elevation from the DEM. The complexity of the dune ridge is defined by the tunable

parameter, and the larger the value the more complex and detail is the dune ridge extracted. The function can be easily applied in ArcGIS using the *Raster Calculator* (a *Spatial Analyst* tool). After defining the cost function for each DEM, the dune ridge was extracted by calculating the cumulative cost surface and the path with the least cumulative cost. These computations can also be done in ArcGIS by using the *Spatial Analyst* tools' *Cost Distance* and *Cost Path*. The dune ridge was approximated for each collection cycle in order to derive seasonal changes in dune morphology of the study area.

The dune ridges were extracted using the least-cost path extraction method. Figure 5.21 shows the dune ridges for all of the collection cycles. All of the dune ridges were positioned very close to each other, and no significant change was detectable. Moreover, the dune ridges exhibited high variability within the small area they cover.

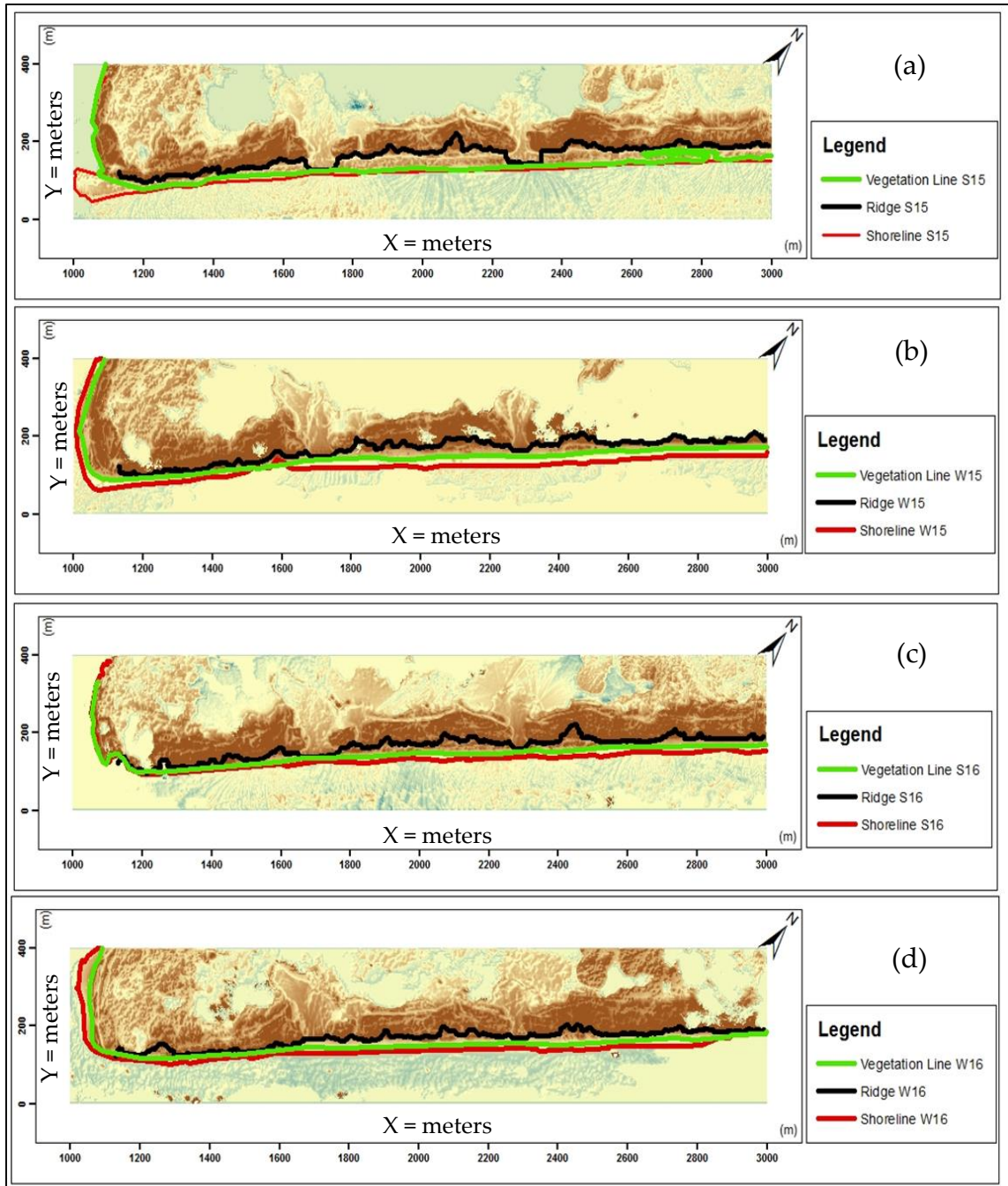


Fig. 5.21: Dune ridges, shorelines, and vegetation lines. The figure shows the dune ridges and their position relative to the shorelines and vegetation lines for (a) Summer 2015, (b) Winter 2015, (c) Summer 2016, and (d) Winter 2016.

5.4 Volumetric Change

Volumetric change analysis is relevant in morphological change detection studies in order to quantify the net gain and loss of sediments in the area, and to identify specific areas prone to sediment loss or gain. Moreover, volumetric change can also be tied together with the analysis of beach profiles to derive seasonal changes related to storms in coastal areas, specifically, the dunes.

As in many morphological changes studies, in order to derive volumetric change, the *Cut Fill* analysis tool was used in ArcGIS (Lee et al., 2011; Pepe and Coutu, 2008). The tool uses a cut-and-fill operation in order to calculate and identify areas of sediment erosion or deposition. It considers two datasets; the surface in its “original” state, and the one after erosion or deposition has affected the study area.

The *Cut Fill* tool identifies edge-connected areas which are given sequential values that represent areas of loss, gain, or no change. The volume is calculated using the following formulas:

$$Volume = cell\ area \times \Delta z$$

$$\Delta z = Z_{before} - Z_{after}$$

In areas where material has been lost (more volume – less volume), the resulting volume is positive. Where material is gained (less volume – more volume), the resulting volume value is negative. The output results include the area of each cell with an assigned object ID and the volume after the calculations.

The volumetric change analysis was performed to derive morphological changes in the dune and coastal areas, but most specifically to extract seasonal sediment loss and gain patterns and compare them with the expected change from summer to winter beaches. The *Cut Fill 3D Analyst* tool was used in ArcGIS in order to quantify net gain or loss in volume at the study area. Net gain or net loss were calculated in a biannual manner, therefore, three maps were extracted as results: the Summer 2015-Winter 2015 volumetric change, the Winter 2015-Summer 2016 volumetric change, and the Summer 2016-Winter 2016 volumetric change. The net gain and net loss were also calculated from Summer 2015 to Winter 2016. Furthermore, the volumetric analysis was limited to examine only the dune area covering approximately 200 m in the cross-beach direction, and approximately 1300 m along the X-direction. The results are seen in Figs. 5.22 through 5.25.

From summer 2015 to winter 2015, there was more volume loss in the area. The sediment loss was mostly experienced by the dunes and the coastal region, while

the backdune area experienced sediment gain. From the Winter 2015 to the Summer 2016 data cycle, there was more sediment loss than gain throughout the whole study area. The sediment loss was experienced in the delta and the coastal areas. Nonetheless, some intermittent areas of sediment gain and loss are seen in some parts of the shoreline and beach areas within the study extent. From Summer 2016 to Winter 2016, more sediment was gained than lost in the area, however, the sediment gain was accumulated in the backdune while the beach berm, the foredune, and part of the delta experienced more sediment loss.

Throughout the total time period that encompasses this study, sediment loss was mostly experienced by the delta banks, and the dune and shoreline regions, while the sediment gain was concentrated mostly in the backdune area.

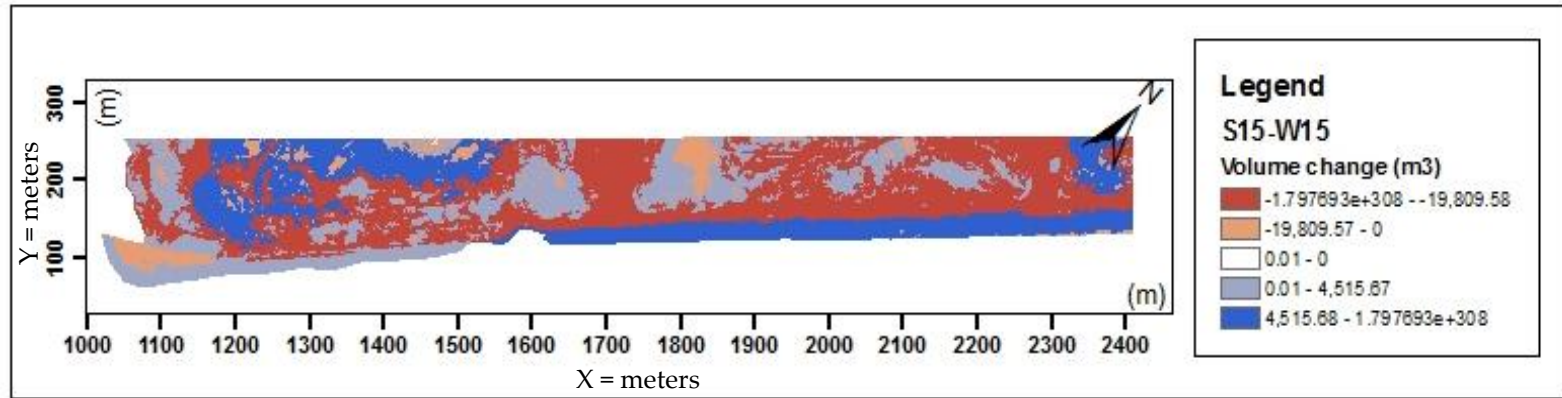


Fig. 5.22: Summer 2015 to Winter 2015 volumetric change. The figure shows the volumetric change after the *Cut Fill* tool was applied in ArcGIS.

114

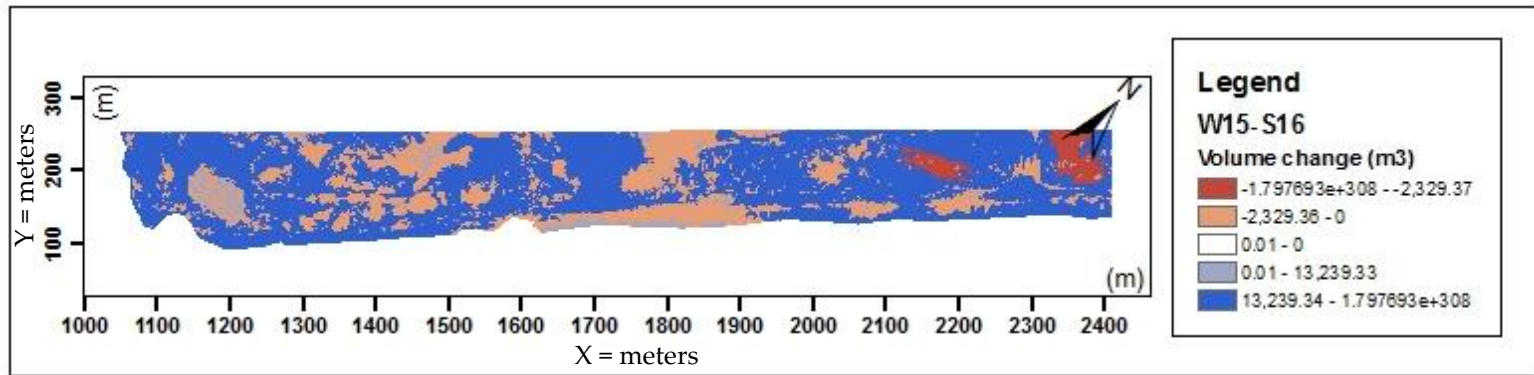


Fig. 5.23 Winter 2015 to Summer 2016 volumetric change. The figure shows the volumetric change after the *Cut Fill* tool was applied in ArcGIS. The.

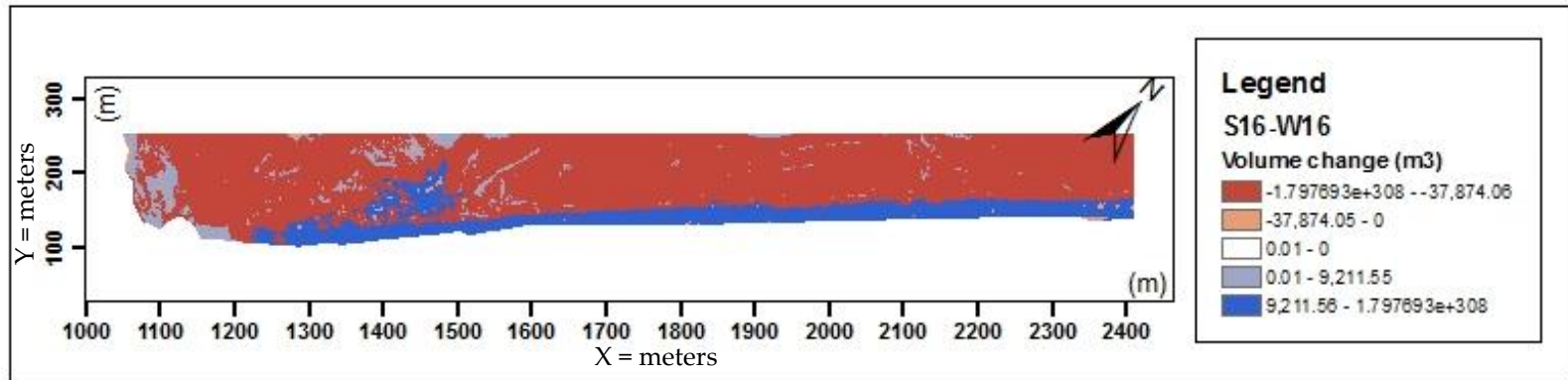


Fig. 5.24: Summer 2016 to Winter 2016 volumetric change. The figure shows the volumetric change after the Cut Fill tool was applied in ArcGIS.

115

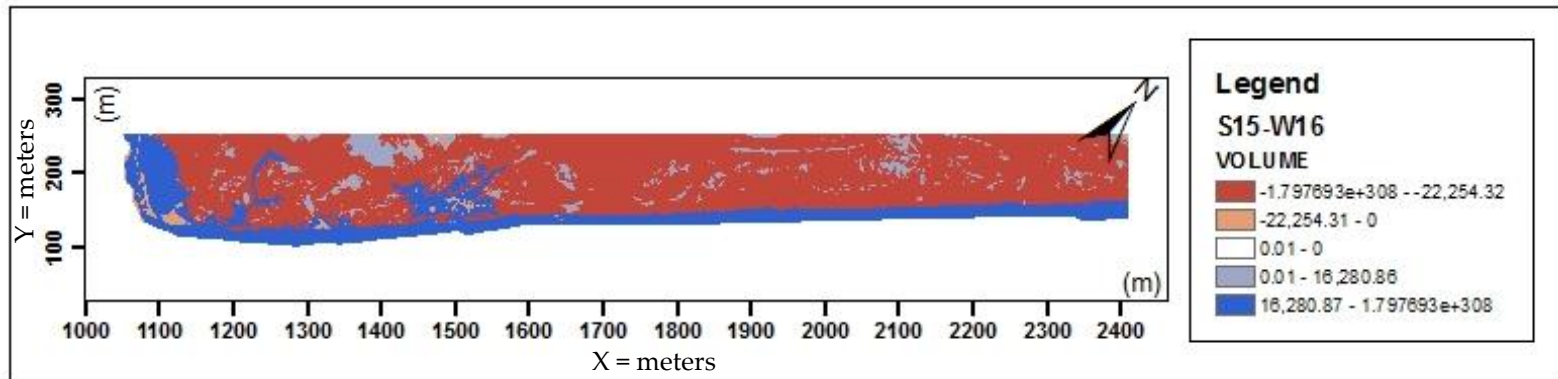


Fig. 5.25: Summer 2015 to Winter 2016 volumetric change. The figure shows the volumetric change after the Cut Fill tool was applied in ArcGIS.

5.4 Beach Profile Analysis

Besides aiding the quantification of morphological changes in coastal areas, beach profiles can be used in order to quantify seasonal changes and the effect of storms in coastal areas. As mentioned before, the “winter” beach is very different from the “summer” beach. During the winter, as the storm frequency increases the wave energy intensifies coastal erosion and offshore sand transportation. These factors can also lead to the formation of an offshore sand bar. During the winter months, the beach profile looks steeper, with a narrow berm. On the other hand, during the summer months, waves tend to be gentler and calmer, allowing for a recovery period where the sand returns to the beach after the winter erosion-prone period. During this time, the beach profile looks gradual and gentler in contrast with the “summer” beach. During this period accretion usually happens, and beaches grow as sand accumulated offshore returns to the coastal area.

For this study, beach profiles of the study area were extracted to study seasonal changes from one season to the other. ArcGIS' *3D Analyst Tools* were used in order to generate two beach profiles per collection cycle, at the $X = 2000$ m and $X = 2600$ m coordinate marks, and from the 150 m cross-dune position to the 200 m cross-dune position for each collection cycle. Figs. 5.26 and 5.27 correspond to the

Summer 2015 collection cycle, and Figs. 5.28 and 5.29 correspond to the Summer 2016 cycle at the two positions in the study area.

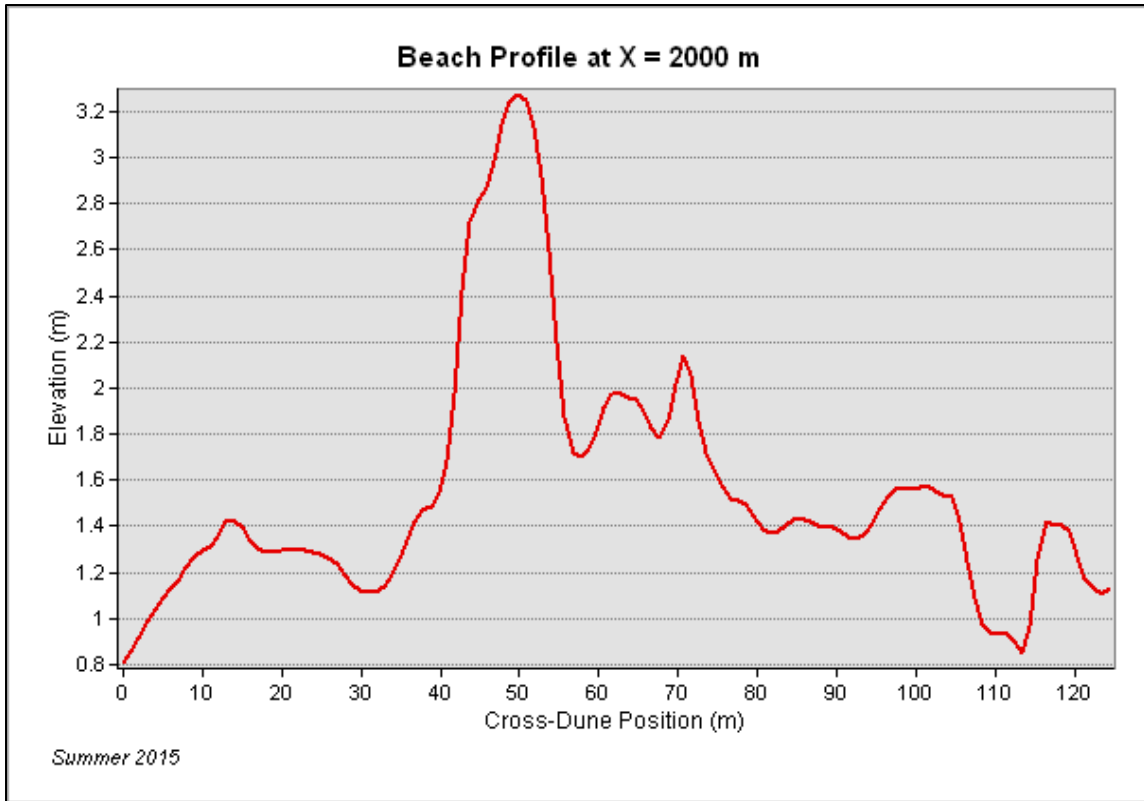


Fig. 5.26: Beach profile for Summer 2015 at X = 2000 m. The beach profile extracted at the X = 2000 m mark from the 150 m to 200 m cross-dune positions.

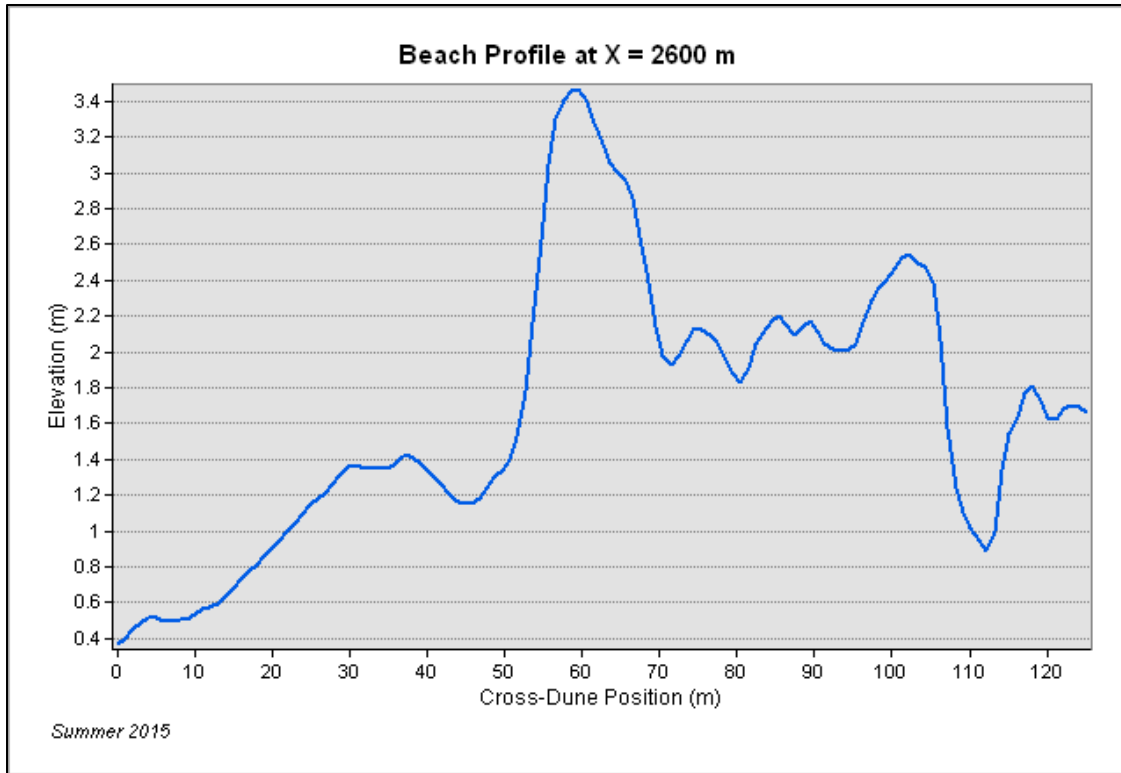


Fig. 5.27: Beach profile for Summer 2015 at X = 2600 m. The beach profile extracted at the X = 2600 m mark from the 150 m to 200 m cross-dune positions.

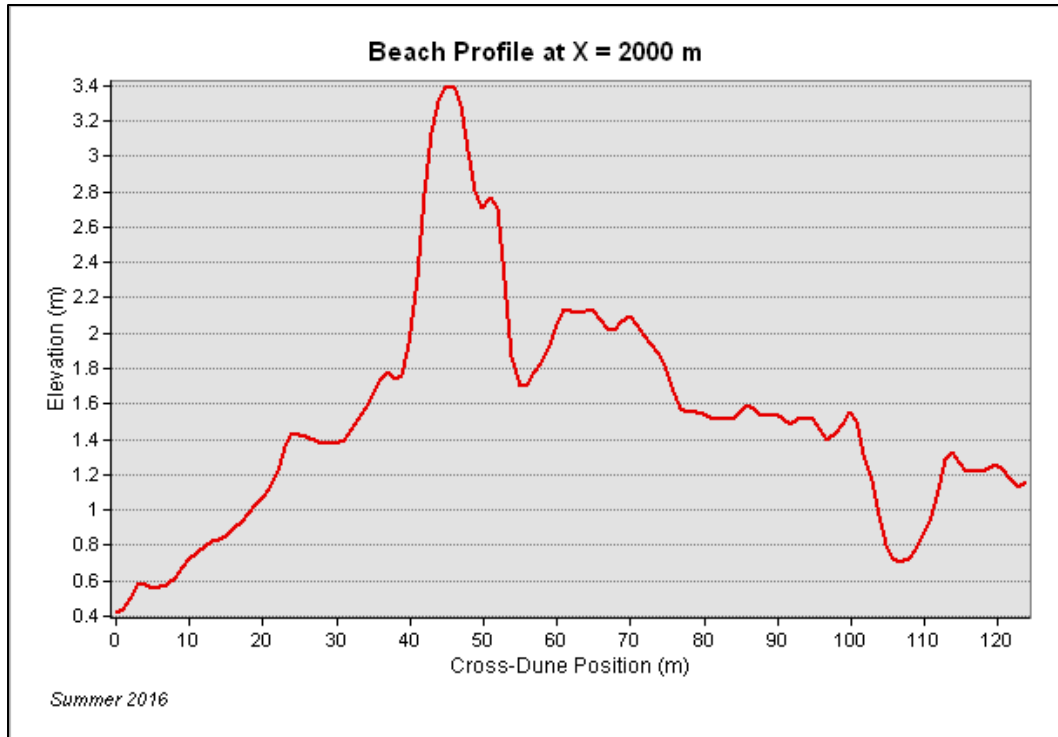


Fig. 5.28: Beach profile for Summer 2016 at X = 2000 m. The beach profile extracted at X = 2000 m mark from the 150 m to 200 m cross-dune positions.

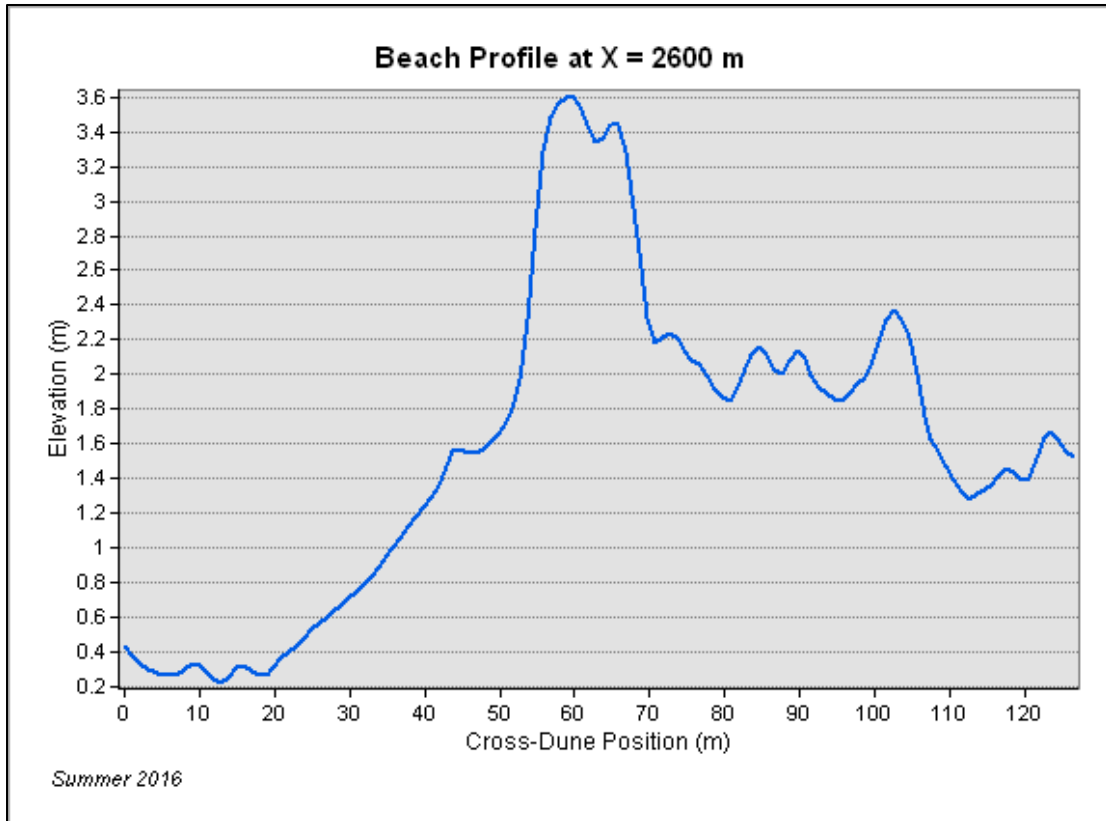


Fig. 5.29: Beach profile for Summer 2016 at X = 2600 m. The beach profile extracted at the X = 2000 m mark from the 150 m to 200 m cross-dune positions.

To better appreciate seasonal changes, the beach profiles were plotted together based on the coordinate mark they were extracted from (Fig. 5.30).

The Summer 2015 beach profile shows abrupt elevation changes when compared to the other datasets as it has a significant lower backshore next to the dune and a higher foreshore possibly due to the effect of the floods and storm episodes that affected the east Texas coast before the dataset was collected. The Winter 2015 dataset had a more gradual profile, but from the volumetric change results, it was still evident that the coastal and beach areas exhibited sediment loss.

Therefore, although the Memorial Day Weekend flood had a great effect on the Summer 2015 beach, the usual seasonal pattern of winter erosion was present. With more sediment loss in the beach area, the Summer 2015 – Winter 2015 period is considered as a period of beach retreat with sediment gain in the backdune area.

The Summer 2016 profile did not change considerably from Winter 2015, although in some instances it had a lower profile. Nevertheless, the volumetric change showed great loss in the backshore and beach areas, while showing some areas of sediment gain in the backdune. The Winter 2015 – Summer 2016 is considered to be a period of shoreline and beach retreat with some sediment deposition in the beach area. Although this does not coincide with expected seasonal changes, the erosional trend can be attributed to the period of storms and floods that affected Texas in April 2016. It can be concluded that not enough sediments returned to the coastal area before the Summer 2016 time period of data collection.

Lastly, the Winter 2016 profiles displayed a lower beach when compared to the Summer 2016 period which was consistent with expected winter beach seasonal changes. Even though this period experienced more sediment gain than loss, the sediment gain was mostly concentrated in the backdune and through regions, while the shoreline, beach and part of the dune areas still experienced sediment

loss. Therefore, the Summer 2016 – Winter 2016 period was considered to be a period of shoreline and beach retreat as well. Moreover, it is also evident that the area behind the dunes is significantly higher in the Winter 2016 profile than the rest of the beach profiles. Therefore it is inferred that the backdune and through regions gained significant sediments during the entire study period.

From the beach profiles, we can also confirm that the dune ridges did not migrate significantly throughout our study period. They are only a few meters from each other in both profiles. However, their height did change and the highest dune ridge corresponded to the Winter 2016 beach profile, and the lowest corresponded to the Summer 2015 profile.

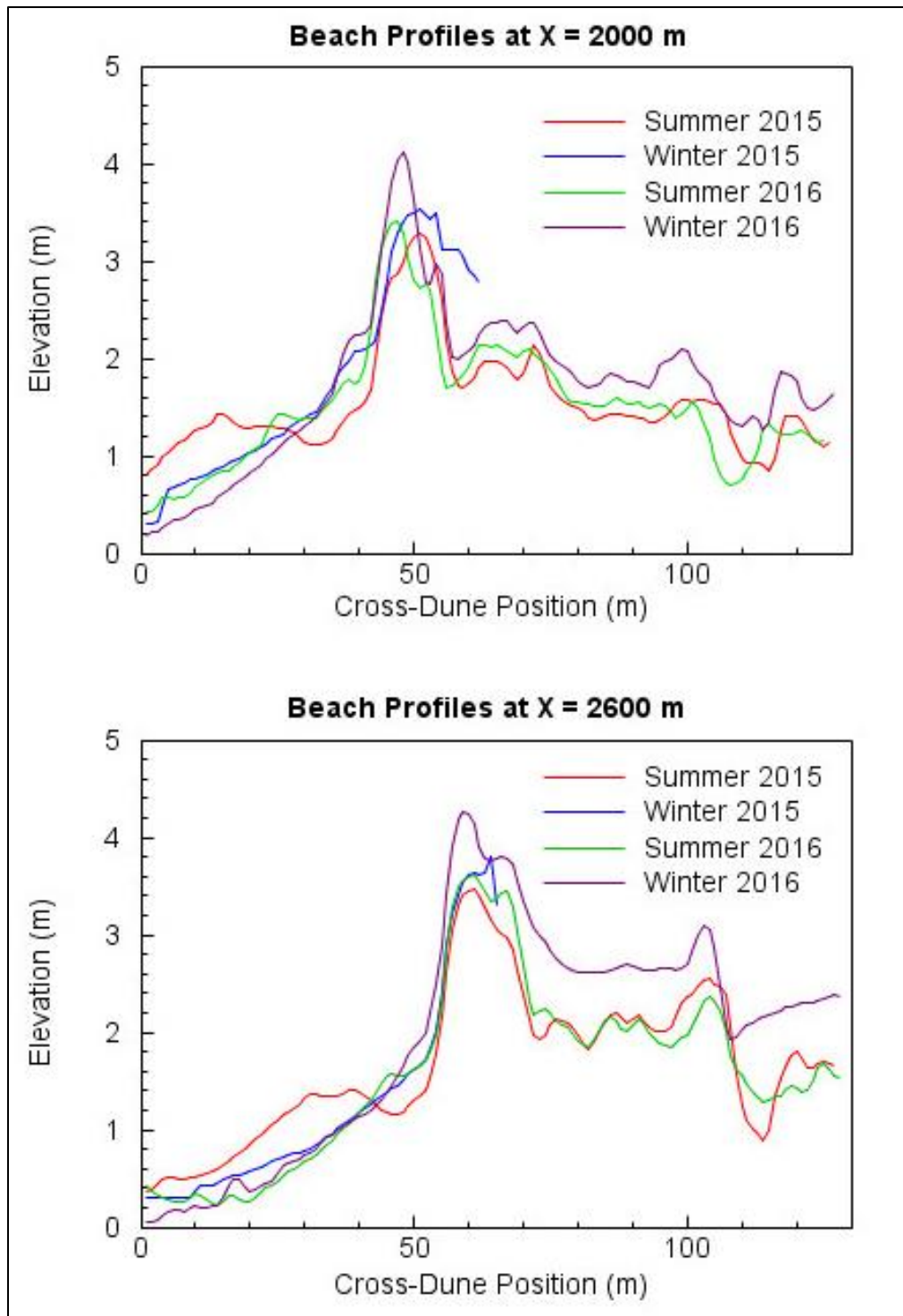


Fig. 5.30: Beach profiles for all datasets. The figure shows the beach profiles at the X = 2000 m and X = 2600 m coordinate marks.

Chapter 6 Discussion and Conclusions

The Texas coast is a highly dynamic environment with many factors in charge of shaping its beach and dune morphology. Previous studies reviewing the morphological changes in Texas coast have been carried out mainly using aerial photography and airborne LiDAR techniques. These studies have documented a 4.5 m shoreline retreat per year since the 1930s. Short-term studies from the 2000s through 2012 also give similar rates-of-change per year. While being one of the few zones with the largest rates-of-change in the Texas coast, the Bryan Beach is documented as one of the most active coastal environments in Texas.

Four biannual TLS LiDAR surveys were carried out at a 2000 m land strip at Bryan Beach, Freeport, Texas. A methodology for the acquisition and processing of the TLS and GPS datasets was established. To analyze the datasets and draw conclusions regarding the morphological change in the area, the DEMs were used for the extraction and examination of coastal features. These features include the approximated shorelines and vegetation lines, and the dune ridge. The features' changes along with the volumetric and beach profile change analysis were considered as proxies for morphological variations in the area throughout the study's time period.

This study concludes that (1) the Texas coast at Bryan Beach retreated significantly during the study period. The shoreline and vegetation line changes are consistent with the general trend for long-term and short-term rates-of-change of the Texas coast. Considering the accuracy assessment of the DEMs and the derived uncertainties for the coastal features extracted, the yearly rate of shoreline movement showed fairly similar values when compared to previous studies.

(2) All of the transition periods from one season to the next one presented beach and shoreline sediment loss, while they also experienced significant sediment gain in the backdune and troughs of the study area. The beach profiles at two different locations in the study area were extracted and analyzed. In general, the beach profiles exhibited expected seasonal changes. After analyzing the beach profiles it was concluded that the transition periods between one season to the next on exhibited the expected seasonal change except for the Winter 2015 – Summer 2016 which experienced erosion probably due to the effect of the Tax Day flood.

(3) The dune ridges in the study area did not migrate significantly. The beach profiles and the dune ridge analysis showed that the dune ridges did not exhibited significant horizontal change in the region. However, the dune heights did change with the highest ridge corresponding to the winter of 2016 dataset.

(4) The accuracy assessment of the point cloud and the DEMs showed expected values when considering the nature of the study area and the survey. Although the accuracy of the region across the dunes in the study area was lower, the flat-beach zones exhibited centimeter level accuracy values consistent with our expectations.

(5) Due to the short term duration of the study, the causes of coastal change could not be precisely specified to a single factor. Although sea-level rise is augmented in Freeport due to subsidence, coastal changes brought up by sea-level rise affect mostly long-term studies. At the same time, there has not been any recent human activity that affected our study area. On the other hand, flood events that affected the study area in May and April of 2015 and 2016 might have affected the Summer 2015 and 2016 collection cycles, and this was observed in the amplified shoreline retreat observed throughout our study period.

References

- Asner, G., Mascaro, J., Muller-Landau, H., Vieilledent, G., Vaudry, R., Rasamoelina, M., Hall, J., and Breugel, M. (2012). "A Universal Airborne LiDAR Approach for Tropical Forest Carbon Mapping." *Oecologia*, vol. 168, issue 4, 1147-1160.
- Buckley, S. J., Howel, J. A., Enge, H.D., and Kurz, T. H. (2008). "Terrestrial Laser Scanning in Geology: Data Acquisition, Processing and Accuracy Considerations." *Journal of the Geological Society*, vol. 165, 625–638.
- Bureau of Economic Geology. (2016). "The Texas Shoreline Project." <<http://www.beg.utexas.edu/coastal/tscp.php>> (September, 2016).
- Conrad Blucher Institute for Surveying and Science (CBI). (2017). "CEPRA Beach Monitoring Program and Coastal Habitat Restoration GIS (CHRGIS)." <<http://www.cbi.tamucc.edu/CHRGIS/>> (February, 2017).
- Dunn, D. D., and Raines, T. H. (2001). "Indications and Potential Sources of Change in Sand Transport in the Brazos River, Texas." Report to the U.S. Geological Survey No. 01-4057. Bureau of Economic Geology, University of Texas at Austin.
- Fairley, I., Thomas, M., Phillips, M., and Reeve, D. (2016) "Terrestrial Laser Scanner Techniques for Enhancement in Understanding Coastal Environments." *Seafloor Mapping along Continental Shelves*, vol. 13, 273-289.
- Gibeaut J. C., White, W. A., Hepner, T., Gutierrez, R., Tremblay, T. A., Smyth, R., and Andrews, J. (2000). "Texas Shoreline Change Project: Gulf of Mexico Shoreline Change from the Brazos River to Pass Cavallo." Report to the Texas Coastal Coordination Council pursuant to National Oceanic and Atmospheric Administration Award No. NA870Z0251. Bureau of Economic Geology, University of Texas at Austin.
- Gibeaut J. C., and Caudle, T. L. (2009). "Defining and Mapping Foredunes, the Line of Vegetation, and Shorelines along the Texas Gulf Coast." Final Report to the Texas General Land Office, Contract No. 07-005-22. Bureau of Economic Geology, University of Texas at Austin.

- Hardin, E., Mitasova, H., Tateosian, L., and Overton, M. (2014). "GIS-based Analysis of Coastal Lidar Time-Series." New York: Springer-Verlag New York.
- Himmelstoss, E.A. (2009). "DSAS 4.0 Installation Instructions and User Guide" in: Thieler, E.R., Himmelstoss, E.A., Zichichi, J.L., and Ergul, Ayhan. 2009 Digital Shoreline Analysis System (DSAS) version 4.0 – An ArcGIS extension for calculating shoreline change: U.S. Geological Survey Open-File Report 2008-1278.
- Jaboyedoff, M., Oppikofer, T., Abellán, A., Derron, M., Loye, A., Metzger, R., and Pedrazzini, A., (2012). "Use of LIDAR in Landslide Investigations: A Review. Natural Hazards, vol. 61, issue 1, 5–28.
- Johnson, K. M., and Ouimet, W. B. (2014). "Rediscovering the Lost Archaeological Landscape of Southern New England Using Airborne Light Detection and Ranging." *Journal of Archaeological Science*, vol. 43, 9-20.
- Kandrot, S. M. (2013). "Coastal Monitoring: A New Approach." *Geographical Journal*, vol. 26, 75-89.
- Killinger, D.K. (2014). "Lidar (light detection and ranging)." *Laser Spectroscopy for Sensing*. Cambridge: Woodhead Publishing. 292-312. Print.
- Kuleli, T. (2009). "Quantitative Analysis of Shoreline Changes at the Mediterranean Coast in Turkey." *Environmental Monitoring and Assessment*, vol. 167, issue 1, 387-397.
- Lee, H.S., Lim, S.S., and Park, D.W. (2011). "Application of Terrestrial Laser Scanner and Raster Operations to Change Detection of Beach." *Journal of Coastal Research*, vol. 2, issue 64, 1692-1696.
- Mahapatra, M., Ratheesh, R., and Rajawat, A.S. (2014). "Shoreline Change Analysis along the Coast of South Gujarat, India, using Digital Shoreline Analysis System." *Journal of the Indian Society of Remote Sensing*, vol. 42, issue 4, 869-976.
- Mitasova, H., Overton, M. F., Recalde, J. J., Bernstein, D. J., and Freeman, C. W. (2009). "Raster-Based Analysis of Coastal Terrain Dynamics from Multitemporal Lidar Data." *Journal of Coastal Research*, vol. 25, issue 2, 507-514.

- Morton, R. A., and Pieper, M. J. (1975). "Shoreline Changes in the Vicinity of the Brazos River Delta (San Luis Pass to Brown Cedar Cut): an Analysis of Historical Changes of the Texas Gulf Shoreline." Bureau of Economic Geology, University of Texas at Austin. Geological Circular, vol. 75, issue 4, 2-47.
- Morton, R. A. (1977). "Historical Shoreline Changes and their Causes, Texas Gulf Coast." Bureau of Economic Geology, University of Texas at Austin. Geological Circular, vol. 7, issue 6, 351-364.
- Muhadi, N. A., Abdullah, A.F., and Kassim, M. S. M. (2016) "Quantification of Terrestrial Laser Scanner (TLS) Elevation Accuracy in Oil Palm Plantation for IFSAR Improvement." IOP Conference Series: Earth and Environmental Science, vol. 37, no. 012042, 1-8.
- Mujabar, S., and Chandrasekar. (2011). "A Shoreline Change Analysis along the Coast Between Kanyakumari and Tuticorin, India, Using Digital Shoreline Analysis System." Geo-Spatial Information Science, vol. 14, issue 4, 282-293.
- NOAA Coastal Services Center. (2012). "Lidar 101: An Introduction to Lidar Technology, Data, and Applications." Revised. Charleston, SC: NOAA Coastal Services Center.
- Paine, J. G., Caudle, T., and Andrews, J. (2013). "Shoreline, Beach, and Dune Morphodynamics, Texas Gulf Coast." Final Report to the Texas General Land Office, Contract No. 09-242-000-3789. Bureau of Economic Geology, University of Texas at Austin.
- Paine, J. G., Caudle, T., and Andrews, J. (2014). "Shoreline Movement along the Texas Gulf Coast, 1930's to 2012." Final Report to the Texas General Land Office, Contract No. 09-074-000. Bureau of Economic Geology, University of Texas at Austin.
- Pepe, G., and Coutu, G. (2008). "Beach Morphology Change Study Using Arcgis Spatial Analyst." Middle States Geographer, vol. 41, 91-97.
- Reshetyuk, Y. (2009). "Self-Calibration and Direct Georeferencing in Terrestrial Laser Scanning." PhD dissertation. Royal Institute of Technology, Department of Transport and Economics, Division of Geodesy. Retrieved from ResearchGate.

- Riegl. (2014). "Riegl VZ-2000: Technical instrumentation and users instructions." (February, 2017).
- Riegl. (2016a). "Data Sheet VZ-2000." <http://www.riegl.com/uploads/tx_pxpriegldownloads/DataSheet_VZ-2000_2016-09-08.pdf> (September, 2016).
- Riegl. (2016b). "RiSCAN PRO 2.0." <<http://www.riegl.com/products/software-packages/riscan-pro/>> (September, 2016).
- Rodriguez, A. B., Hamilton M. D., and Anderson, J. B. (2000). "Facies and Evolution of the Modern Brazos Delta, Texas: Wave versus Flood Influence." *Journal of Sedimentary Research*, vol. 70, issue 2, 283-295.
- Roth, D. (2010). "Texas Hurricane History." United States National Oceanic and Atmospheric Administration's National Weather Service.
- Shan, J., and Toth, C. K. (2009). "Topographic Laser Ranging and Scanning: Principles and Processing." Boca Raton: CRC Press/Taylor & Francis Group.
- Sidwell, R. (1940). "Sediments Transported by the Texas River from High Plains, Texas." *Journal of Sedimentary Petrology*, vol. 10, no. 3, 138-141.
- Santos, A. L. S., Amaro, V., and Teles Santos, M. S. (2014). "Terrestrial Laser Scanner Applied to Monitoring Beach Morphological Changes in a High Energy Coastal Zone in Northeast Brazil." Presented at the 7th International Terrestrial Laser Scanner User Meeting, Rome, Italy. June, 2014
- Stanica, A., and Ungureanu, G. V. (2010). "Understanding Coastal Morphology and Sedimentology." *NEAR Curriculum in Natural Environmental Science*, vol. 88, 105-111.
- Swanson, R.L., and Thurlow, C. I. (1973). "Recent Subsidence Rates along the Texas and Louisiana Coast as Determined from Tide Measurements." *Journal of Geophysical Research*, vol. 78, issue 15, 2665-2671.
- Syvitski, J.P.M. (2003). "Supply and Flux of Sediment along Hydrological Pathways: Research for the 21st Century." *Global and Planetary Change*, vol. 39, 1-11.

- Telling, J., Lyda, A., Hartzell, P., and Glennie, C. (2017) "Review of Earth Science Research Using Terrestrial Laser Scanning." *Earth Science Reviews*, vol. 169, 35-68.
- Wehr, A., and Lohr, U. (1999). "Airborne Laser Scanning – An Introduction and Overview." *ISPRS Journal of Photogrammetry and Remote Sensing*, vol. 54, 68–82.
- Wessel, P., and Smith, W. H. F. (2016). "The Generic Mapping Tools Technical Reference and Cookbook." Version 4.5.14, pp. <https://www.soest.hawaii.edu/gmt/gmt/pdf/GMT_Docs.pdf> (September, 2016).
- Xiong, L., Wang, G., and Wessel, P. (2016). "Anti-Aliasing Filters for Deriving High Accuracy Dems from TLS Data: A Case Study from Freeport, Texas." Submitted for publication.